# CMFT+DMRG method to characterize gapless phases of ultracold bosons in optical lattices

A Thesis submitted in partial fulfillment for the Degree of

DOCTOR OF PHILOSOPHY
in
School of Physical and Applied Sciences
Goa University


by

**PALLAVI P. GAUDE**

School of Physical and Applied Sciences
Goa University
Goa, India

**December 2023**

## DECLARATION

I, Pallavi P. Gaude hereby declare that this thesis represents work which has been carried out by me and that it has not been submitted, either in part or full, to any other University or Institution for the award of any research degree.

Place: Taleigoa Plateau
Date: 23-12-2023 Signature of the Candidate

## CERTIFICATE

I hereby certify that the work was carried out under my supervision and may be placed for evaluation.

Prof. Ramesh V. Pai
School of Physical and Applied Sciences
Goa University

. . . . . .

*Dedicated,*
*to my*
*Parents and*
*late Grandfather.*

. . . . . .

# *Acknowledgements*

First and foremost, I express my sincere gratitude to my research guide, Prof. Ramesh V. Pai, for all his teaching, unwavering support, and upliftment during my Ph.D. work. His valuable intellect and passion for the subject have inspired me time and time again to stay calm and dedicated to the topic. Despite his academic responsibilities, he gave me enough time for the discussion and encouragement I needed throughout these years.

I sincerely thank the members of DRC and VC's nominees, Prof K. R. Priolkar and Dr. Bholanath Pahari, for monitoring my research progress throughout these years.

For the Computing facilities, I express my gratitude to Goa University for providing access to the HPC PARAM SHAVAK and Parvatibai Chowgule College of Arts and Science for computational resources.

I would also like to thank the faculty members of the School of Physical and Applied Sciences, Goa University, for their support and the non-teaching staff for their constant cooperation during this work.

I sincerely acknowledge Dr. Ananya Das for the warm support and encouragement she has showered on me throughout this year.

I am also thankful to my fellow research scholars and friends for fruitful discussions, suggestions, and motivation.

Finally, I would like to thank my parents for their unconditional love and support.

**Pallavi P. Gaude**
PhD Fellow, Goa University

# *Abstract*

In recent years, ultra-cold atoms trapped in optical lattices have gained massive interest. The complex interactions, impurities, and disorders make understanding the solid-state system difficult. However, the ability to control these various aspects in optical lattices makes them ideal testing grounds for simulating the solid-state system and exploring the plethora of exotic phases arising due to rich inter-particle interactions. In this thesis, we have developed a theoretical method, the cluster mean-field theory plus the density matrix renormalization group (CMFT+DMRG) approach, to study the phases in the Bose-Hubbard models. In Chapter 1, we have briefly introduced the Bose-Einstein condensation, optical lattice systems, and the Bose-Hubbard model. The cluster mean-field theory and density matrix renormalization group theory (CMFT+DMRG), as well as its successes and limitations, are discussed in Chapter 2, followed by the methodology of the CMFT+DMRG method. Chapter 3 demonstrates the CMFT+DMRG method using the Bose-Hubbard model and compares the results with the DMRG result. The CMFT+DMRG method captures the superfluid and Mott Insulator phases expected in the Bose-Hubbard model, and the phase diagram agrees with the earlier studies. Chapter 4 is devoted to exploring the phases in the extended Bose-Hubbard model.

The finite long-range interaction in the extended Bose-Hubbard model predicts a variety of phases such as superfluid, density wave, Mott insulator, supersolid, solitonic, and phase-separated phases. The CMFT+DMRG method captures the Berezinskii–Kosterlitz–Thouless phase transition between superfluid and density wave in the hard-core limit of the extended Bose-Hubbard model at half-integer density.

We have investigated the phases in the EBH model and obtained the phase diagram. We finally explore the effect of the attractive three-body on-site interaction in the phases of the extended Bose-Hubbard model. Lastly, Chapter 5 summarizes the CMFT+DMRG method's results and limitations and indicates the future scope.

# Contents

**Abstract** i

**Table of Contents** ii

**List of Figures** iv

**List of Tables** ix

**1 Introduction** 1
- 1.1 Introduction . . . 1
- 1.2 Motivation . . . 11
- 1.3 Objectives . . . 12
- 1.4 Overview . . . 13

**2 Methods** 15
- 2.1 Introduction . . . 15
  - 2.1.1 Single Site Mean-Field Theory . . . 16
  - 2.1.2 Cluster Mean-Field Theory . . . 19
  - 2.1.3 Density-Matrix Remormalization Group Theory . . . 24
  - 2.1.4 Cluster mean-field Plus Density matrix Renormalization Group Method . . . 30
    - 2.1.4.1 Translational Symmetry Case . . . 31
    - 2.1.4.2 Bipartite lattice . . . 33
  - 2.1.5 Conclusions . . . 39

**3 Bose Hubbard Model** 41
- 3.1 Introduction . . . 41
- 3.2 Convergence of superfluid order parameter . . . 42
- 3.3 Comparison of CMFT+DMRG with DMRG . . . 44
- 3.4 Staggered Superfluid Phase in Bose-Hubbard model . . . 51
- 3.5 Conclusions . . . 55

**4 Extended Bose-Hubbard Model** 57
- 4.1 Introduction . . . 57
- 4.2 Extended Bose-Hubbard Model . . . 59
  - 4.2.1 Hard-core case . . . 62
  - 4.2.2 Soft-core case . . . 67
- 4.3 Extended Bose-Hubbard Model with three body interactions . . . 78

4.4 Conclusion . . . . . 81

**5 Summary** **85**
5.1 Summary . . . . . 85
5.2 Outlook . . . . . 89

**6 Publications and Conferences** **91**
6.1 List of Publications . . . . . 91
6.2 List of Conferences attended . . . . . 91

**Bibliography** **93**

# List of Figures


1.1 Velocity distribution of $^{87}$Rb atoms near at temperature $T > T_c$ (leftmost), $T \approx T_c$ (middle) and $T < T_c$ (rightmost). The colors represent red for the fastest moving atoms to white for the slowest moving atoms. Figure courtesy: Cornell E. (1996) [16]. . . . . 4

1.2 Optical lattices are formed by superimposing two and three pairs of lasers in a) 2D and b)3D. In a 2D optical lattice, the atoms are confined in array potentials represented by grey tubes and spheres in a 3D case. Figure courtesy: I.Bloch (2008) [21]. . . . . 7

1.3 Time of flight images of matter-wave interference patterns for different optical lattice potentials a) 0, b)3 $E_r$, c)7Er, d)10$E_r$, e)13$E_r$, f) 14$E_r$, g) 16$E_r$, and h)20$E_r$ depicts phase transition from superfluid to Mott insulator phase. The potentials are measured using the recoil energy $E_r = \frac{\hbar^2 k^2}{2m}$. In the superfluid phase, the central peak is observed, and in the Mott insulator phase, the central peak is destroyed, and phase coherence is lost. Figure courtesy: M. Greiner(2002) [24]. . . . . 10

2.1 Site configuration of (a) one-dimensional and (b) two-dimensional system. The dotted line represents the hopping term approximated using the mean-field decoupling $\langle \hat{a}_j \rangle + \delta \hat{a}_j$. . . . . 17

2.2 Site configuration of the one-dimensional system for cluster size with (a) one site and (b) two sites. The solid line represents the exact hopping within the cluster, and the dotted lines represent the hopping term approximated using the mean-field decoupling $\langle \hat{a}_j \rangle + \delta \hat{a}_j$. . . . . 20

2.3 Site configuration of the one-dimensional system for cluster size L. Here, the cluster $p$ is decoupled from the neighbouring clusters, $p-1$ and $p+1$, using the mean-field decoupling. The dotted line represents the approximated hopping between the clusters. . . . . 21

2.4 Schematic representation of RSRG for 1D system. . . . . 25

2.5 Schematic representation of DMRG iteration for the 1D system. (a) A superblock consists of the system block $S$ and the environment block $E$, and the two sites $(s, e)$, (b) Single site $s$ is added to the system block $S$ to form new system block $S'$ and (c) the new superblock is formed replacing $S$ with $S'$ and $E$ with $E'$, and two new sites $s$ and $e$. . . . . 27

2.6 Schematic representation of CMFT+DMRG iteration for the 1D system. (a) A superblock consists of the system block $S$ and the environment $E$ and the two sites $(s, e)$, (b) The single site $s$ is added to the system block $S$ to form new system block $S'$ and (c) new superblock is formed replacing $S$ with $S'$ and $E$ with $E'$ and two new sites $s$ and $e$. . . . . 30
2.7 Schematic representation of the CMFT+DMRG method for a bipartite lattice. The dotted lines represent the mean-field decoupling, and the solid lines represent the exact hopping in the superblock. (a) represents the superblock constructed from symmetric blocks $S$ and $E$ with the site $s$ in between, (b) the formation of new block $S'$, and (c) a new superblock formed using $S'$ and $E'$. . . 34

3.1 Superfluid order parameter $\psi_j$ and boson density $\rho_j$ are plotted as a function of position $j$. Here we have considered a lattice with length $L = 50$ and model parameters $U = 5$ and $\mu = 0.6$. . . . . 43
3.2 The superfluid order parameter $\psi_j$ are plotted as a function of position $j$ for different lengths $L$. Here $U = 5$ and $\mu = 0.6$. . . . . 45
3.3 The boson density $\rho_j$ are plotted as a function of position $j$ for different lengths $L$. Here parameters $U = 5$ and $\mu = 0.6$ are same as that in Fig 3.2. . . . . 46
3.4 The superfluid order parameters $\psi(1)$, $\psi(L/2)$ and the boson densities $\rho(1)$ and $\rho(L/2)$ are plotted as a function length $L$ for $U = 5$ and $\mu = 0.6$. . . . . 46
3.5 The superfluid order parameters $\psi(1)$, $\psi(L/2)$ and the boson densities $\rho(1)$ and $\rho(L/2)$ are plotted as a function length $L$ for $U = 5$ and $\mu = 1.4$. . . . . 47
3.6 Density $\rho$ from DMRG (blue line) and CMFT+DMRG (black line with bullet) methods and $\psi$ from the CMFT+DMRG method for two different lengths. . . . . 47
3.7 (a) $\rho$ and (b) $\psi$ for different lengths for on-site interaction $U = 5$. . 48
3.8 (a) $\rho$ and (b) $\psi$ for different lengths $L = 100,\ 200,\ \cdots,\ 3700$ for on-site interaction $U = 4$. . . . . 49
3.9 (a) Decay of phase coherence correlation function $\Gamma(r)$ with respect to $r$. $\Gamma(r) \to \psi^2$ as $r \to \infty$. (b) Variation of the condensate fraction $n(0)$ and the superfluid density $\rho_S$ across SF-MI transition. . . . . 51
3.10 $\mu - U$ phase diagram of Bose Hubbard model close to density $\rho = 1$ using the DMRG (black line)) and CMFT+DMRG (red dot) method. 51
3.11 The superfluid order parameter $\psi_j$ (top panel) and density $\rho_j$ (bottom panel) are plotted as a function of position $470 < j < 530$ for length $L = 1001$. Here $t = -1$, $U = 5$, and $\mu = 0.5$. . . . . 53
3.12 Superfluid order parameters $\psi_A = \psi_{\frac{L-1}{2}}$ and $\psi_B = \psi_{\frac{L+1}{2}}$ versus $\mu$ for $t = -1$ and $U = 5.0$. . . . . 54
3.13 The boson densities for $t = 1$ and $t = -1$ are plotted as function of $\mu$ for $U = 5.0$. . . . . 55
3.14 The superfluid density $\rho_S$ for $t = \pm 1$ and $\Delta_{\pi-\mathrm{SF}}$ is plotted as function of $\mu$ for $U = 5.0$. The finite $\Delta_{\pi-\mathrm{SF}}$ marks the $\pi$-SF phase. . . . . 55

4.1 (a) superfluid order parameter, (b) density wave order parameter, (c) condensate fraction, and (d) $S(\pi)$ across SF to DW phases. . . . 64
4.2 $\psi$, $\delta\psi$, $\rho$ and $\Delta$ plotted as a function of $\mu$ for $V = 1.0$ (left panel) and $V = 3.0$ (right panel) . . . . . 65
4.3 Plots of $\psi_i = \langle a_i \rangle$ and $\rho_j = \langle n_i \rangle$ as a function of lattice position $i$ for $\mu = 1.0,\ 2.0,\ 3.0$, $U = \infty$ and $V = 1.0$(top panel) and $V = 3.0$(bottom panel). . . . . 65
4.4 $\rho_A = \rho_{\frac{L+1}{2}}$ and $\rho_B = \rho_{\frac{L-1}{2}}$ plotted as function of lattice position $\mu$ for $V = 3.0$. . . . . 66
4.5 (a) $\psi$, (b) $\delta\psi$, (c) $\Delta$, and (d) $\rho$ plotted as a function of $\mu$ for a fixed $V = 4.0$ and $U = 0.5$. . . . . 67
4.6 Variation of $\psi_j$ and $\rho_j$ with lattice position $j$ for (a) $\mu = 1.10$ and (b) $\mu = 1.12$ for $V = 4.0$ and $U = 0.5$. . . . . 69
4.7 Variation of $\rho_j$ with lattice position $j$ from the DMRG calculation fixing density $\rho = 1$ for $V = 4.0$, $U = 0.5$. The lower panel is the expanded supersolid region. . . . . 70
4.8 Variation of $\rho_j$ versus $j$ for five different densities from DMRG calculation with $L = 301$. Number of bosons $N = 185,\ 270,\ 301,\ 330,$ and 399, corresponding to the densities $\rho = N/L = 0.615,\ 0.897,\ 1.0,\ 1.096,$ and 1.326. . . . . 70
4.9 Length of the superfluid region as a function of $\rho$ for (a) $U = 0.5$ and (b) $U = 1.2$ keeping $V = 4.0$. . . . . 71
4.10 (a) $\psi$, (b) $\delta\psi$, (c) $\Delta$, and (d) $\rho$ plotted as a function of $\mu$ for a fixed $V = 4.0$ and $U = 1.3$. . . . . 71
4.11 (a) $\psi$, (b) $\delta\psi$, (c) $\Delta$, and (d) $\rho$ plotted as a function of $\mu$ for a fixed $V = 4.0$ and $U = 3.0$. . . . . 72
4.12 Phase diagram in $\rho - U$ for $V = 4.0$ . . . . . 72
4.13 (a) $\psi$, (b) $\delta\psi$, (c) $\Delta$, and (d) $\rho$ plotted as a function of $\mu$ for a fixed $V = 2.0$ and $U = 0.1$. . . . . 73
4.14 (a) $\psi$, (b) $\delta\psi$, (c) $\Delta$, and (d) $\rho$ plotted as a function of $\mu$ for a fixed $V = 2.0$ and $U = 0.5$. . . . . 73
4.15 (a) $\psi$, (b) $\delta\psi$, (c) $\Delta$, and (d) $\rho$ plotted as a function of $\mu$ for a fixed $V = 2.0$ and $U = 1.0$. . . . . 74
4.16 Phase diagram in $\rho - U$ for $V = 2.0$ . . . . . 74
4.17 Phase diagram in $\rho - U$ for $V = 6$. . . . . 76
4.18 Plot of $\rho_j$ versus $j$ for a set of $\mu$ values for $V = 6.0$ and $U = 8.0$. . 77
4.19 The structure factor $S(k)$ is plotted as a function of $k/\pi$ for $V = 6.0$ and $U = 8.0$ for different $\mu$. The shifted peak from $\pi$ shows the presence of SL phase. . . . . 77
4.20 The Modulation vector $k_m$ and $2\pi\rho$ plotted as function of $\mu$. . . . . 78
4.21 Comparison of (a) the superfluid order parameter $\psi$, (b) the density $\rho$ and (c) $\Delta$ for $U = 0.8, V = 2.0$ varying $W = 0, -0.1, -0.5, -0.7, -1.0$. 82
4.22 Comparison of (a) the superfluid order parameter $\psi$, (b) the density $\rho$ and (c) $\Delta$ for $U = 0.5, V = 4.0$ varying $W = 0, -0.1, -0.5, -1.0, -1.5, -2.5$. 83

# List of Tables

4.1 Order parameter values and density for SF, MI, DW, and SS phase 61

CHAPTER 1

# Introduction

## 1.1 Introduction

Ultra-cold atoms trapped in optical lattices are ideal laboratories for simulating many-body interacting systems in condensed matter physics. Although all the constituents of the solid-state systems, such as atoms and electrons, are known, complexities like electron-electron and electron-atom interaction, impurities, and disorders pose a problem in anticipating the behavior of the solid-state system. We need to obtain a reliable theoretical solution. The optical lattice provides us with simplified models to study these systems. The ability to control and manipulate various parameters in optical lattices, such as the hopping amplitude, dimensions, interaction energy, and disorder strength, allows us to engineer a variety of effective Hamiltonians to explore. Different numerical and analytical methods are available to solve these systems. In this thesis, we aim to develop one such approach: a cluster mean-field plus density matrix renormalization (CMFT+DMRG) method for solving such Hamilonians known as Bose-Hubbard models. In this chapter, we will first introduce the Bose-Einstein condensation and its experimental realization, followed by the optical lattices and the model mapping ultra-cold bosons in the optical lattices.

In 1924, Satyendra Nath Bose introduced statistics for indistinguishable photons [1], later generalized by Albert Einstein for all integer spin particles with

symmetric total wavefunction called bosons and termed Bose-Einstein statistics. According to it, the number of indistinguishable bosons in the energy level $\epsilon_i$ for $\epsilon > \mu$ is given by

$$n(\epsilon_i) = \frac{g_i}{e^{\frac{(\epsilon_i - \mu)}{k_B T}} - 1} \tag{1.1}$$

where $k_B$ is Boltzmann constant, $T$ is temperature, $\mu$ is the chemical potential-energy required to add a particle, and $g_i$ is the degeneracy of $\epsilon_i$. The upper bound of $\mu$ is the ground state energy $\epsilon_0$, and the condensation occurs in the ground state. For $k_B T >> (\epsilon_i - \mu)$, more than half of the particles occupy the ground state, and this number increases as $k_B T$ approaches $\epsilon_i - \mu$. Based on these statistics, the quantum phenomena of Bose-Einstein condensation (BEC) was predicted in 1925 for ideal non-interacting Bose gas [2]. The fundamental concept behind the BEC being below the critical temperature $T_c$, given by

$$T_c = \left(\frac{n}{\zeta(3/2)}\right)^{2/3} \frac{h^2}{2\pi m k_B} \tag{1.2}$$

the macroscopic number of bosons occupy the lowest energy state. Here, $n$ is the boson density, $h$ is the Plank's constant, $m$ is the boson's mass, and $\zeta(3/2)$ is the Riemann zeta function. The de Broglie wavelength $\lambda$ of particles given by

$$\lambda = \frac{h}{\sqrt{2\pi m k_B T}} \tag{1.3}$$

As the Bose gas temperature decreases, $\lambda$ increases as $T^{-1/2}$. When $T \approx T_c$, $\lambda$ is comparable to the mean inter-particle separation $n^{-\frac{1}{3}}$ of bosons forming condensate. At this point, particles are so close that there is an overlap between the wavefunctions of the bosons, and the entire Bose gas is represented by a giant macroscopic wavefunction- a coherent wave.

The possibility of observing quantum phenomena at the macroscopic level fueled the experimental efforts to realize BEC. However, the low-temperature requirement became a significant hurdle in realizing the BEC. The $T_c$, being directly proportional to the density of the bosons $n$ and inversely to its mass $m$, favored

using lighter bosons with high densities to increase the $T_c$ in the experiments. However, with very high $n$, the transition from gas to liquid to solid was detected with decreasing temperature even before the condensation occurred. This lead to the desired densities of the order $10^{13} - 10^{14}\text{cm}^{-3}$ resulting in the $T_c$ in the nano Kelvin region. The initial experimentation concentrated on the light bosons such as Hydrogen, Helium, etc. The BEC in spin-polarized hydrogen failed because of insufficient experimental devices to produce it at sufficient densities. In $^4$He, the BEC was predicted at $T_c = 3.14K$, but the strong interaction drives the transition to the superfluid phase at a temperature equal to $2.47K$ [3]. In this phase, the fluid flows with zero viscosity below the transition temperature. Although the BEC was predicted for non-interacting bosons, London suggested BEC as the underlying mechanism behind the superfluidity in the strongly interacting $^4$He. Neutron scattering experiments later proved this prediction.

It was not until the advances in experimental techniques such as laser cooling [4] and evaporative cooling [5] that the BEC was first realized in dilute alkali gases at JILA using $^{87}$Rb atoms [6] and at MIT using $^{27}$Na atoms [7] in 1995 which garnered the Nobel prize in Physics in 2001. In these experiments, atoms are typically gathered in a magneto-optical trap and cooled to micro-Kelvin temperatures using laser cooling techniques. They are then transferred to a magnetic trap where evaporative cooling allows the system to be cooled to nano-Kelvin temperature, forming the condensate as seen in the velocity distribution of $^{87}$Rb atoms in figure 1.1. In the $T > T_c$ regime, the bosons occupy all possible states, and a significant number of bosons occupy the ground state seen from the broad peak in Fig. 1.1 (left). As temperature decreases, more bosons start settling in the lowest energy state Fig. 1.1 (center), and at $T_c \approx 170$ nK, atoms mostly occupy the lowest energy state, forming the BEC. The narrow peak in the velocity distribution in Fig. 1.1 (right) is the signature of BEC. After this initial success, BEC was experimentally realized in dilute bosonic gases such as $^7$Li [8], $^{40}$Ca [9], $^{41}$K [10], $^{39}$K [11], $^{170}$Yb [12], $^{23}$Na [13] and many more weakly interacting bosons.

BEC is also achieved by mixing two different bosons and purely optical traps, where the spin degrees of freedom play important role [14], [15].

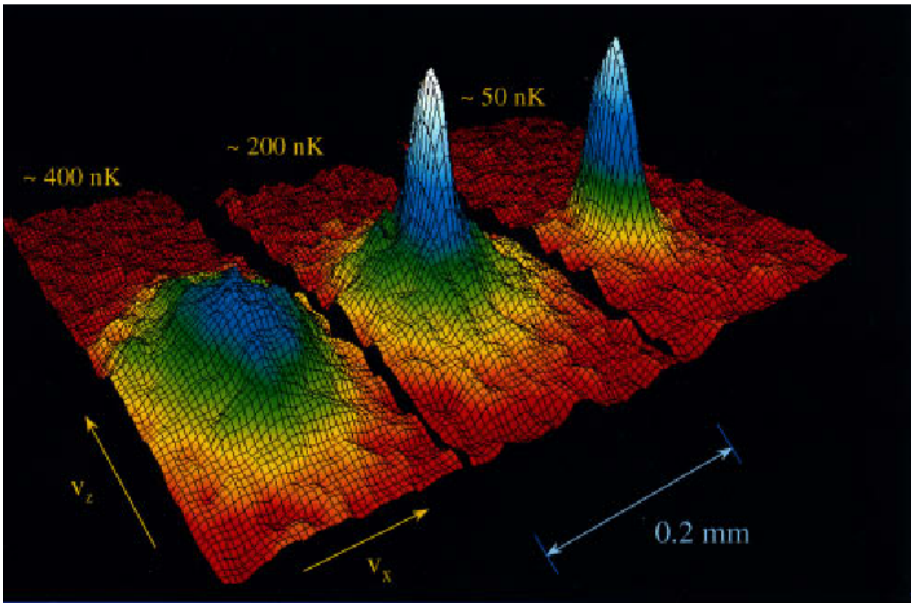


Figure 1.1: Velocity distribution of $^{87}$Rb atoms near at temperature $T > T_c$ (leftmost), $T \approx T_c$ (middle) and $T < T_c$ (rightmost). The colors represent red for the fastest moving atoms to white for the slowest moving atoms. Figure courtesy: Cornell E. (1996) [16].

The experimental realization of BEC in weakly interacting alkali gases opened unique opportunities for exploring the quantum phenomena on a macroscopic scale and studying the coherent matter wave properties, pioneering many experiments such as coherent lasers. This topic gained more impetus with a proposal of D. Jaksch and his team to use trapped ultra-cold bosonic atoms in an array of optical potential to create avenues for research into the strongly correlated system [17]. Over the last few decades, the strongly correlated systems have become one of the active research fields in the condensed matter physics. Theoretical predictions and experimental observations in recent years have revealed a variety of complicated phases, including superconductivity, magnetic semiconductors, and gigantic magneto-resistance. They arise due to the subtle interplay between Coulomb interaction, spin fluctuations, charge fluctuations, lattice, and band structure. In theory, all these interactions must be included in the Hamiltonian to study these systems. However, the scale and various interactions make the theoretical stud-

ies a difficult task to undertake. The uncontrollable complexities like disorders and impurities further add to these difficulties. The possibility of converting the weakly interacting BEC in alkali atoms into strongly interacting systems opened new avenues to comprehend and predict the solid state systems' phases using pristine and controllable systems.

The array of potentials created by the interference of laser beams forms the optical lattices. The standing wave resulting from the interference of the counter-propagating laser beam is the simplest 1D lattice with the trapping potential

$$V_0(x) = V_0 \sin^2(kx) \tag{1.4}$$

where $k = 2\pi/\lambda$ and $\lambda$ are the laser beam's wave vector and wavelength, and $V_0$ is the lattice potential depth. The dimensionality and the lattice geometry are controlled in optical lattices using laser beams. Higher dimensions and complex optical lattices, such as a kagome or triangular lattice, can be created by superimposing more laser beams. The simplest 3D optical lattice is created by overlapping three standing waves with no cross-interference between the laser beams of different standing waves. Such 3D optical lattice is approximated by which can be approximated by a simple cubic array of harmonic potentials

$$V_0(x) = V_0(\sin^2(kx) + \sin^2(ky) + \sin^2(kz)) \tag{1.5}$$

AC Stark effect is used to trap the atoms in the optical lattices. The laser beam interacts with the atoms through its electric field inducing the dipole moment ($d$) in the atoms. The induced dipole moment interacts with the electric field, creating the potential

$$V_0(x) = -d.E(x) \propto \alpha(\omega)|E(x)|^2, \tag{1.6}$$

where $E(x)$ is the electric field of the laser is proportional to the intensity of the laser beam, and $\alpha(\omega)$ is the polarizability of the atom. The laser's electric field oscillates spatially, creating a periodic array of potentials simulating the solid-

state crystals. The frequency of the laser beam $\omega$ used to form the optical lattices is tuned away from the atom's resonance frequency $\omega_0$ to avoid the spontaneous emission. When $\omega < \omega_0$, the laser is red detuned, the dipole force is attractive, and atoms are attracted to the region of maximum intensity, i.e., a region with maximum intensity is potential minima for red detuned laser. Whereas for blue detuned laser- $\omega > \omega_0$, the dipole force is repulsive, and atoms occupy region with minimum intensity. The distance between two potential minima is $\lambda/2$, which is of the order micro-meter and can be manipulated by changing the wavelength of the laser beam [18]–[20]. Further, the Feshbach resonances can control the scattering length $a_s$ beyond the inter-particle distances along with its polarity in two-particle scattering. The Feshbach resonances occur in the two-particle scattering when the bound state in the closed channel couples resonantly with the continuum in the scattering channel [21]. The Feshbach resonances in the optical lattices can be controlled using the laser beam. The control on scattering length $a_s$ gives control over the interaction between the particles, which can be made attractive or repulsive. In optical lattices, atoms can tunnel through the potential barrier to the adjacent lattice site depending on the laser beam intensity. A laser beam can control and manipulate various parameters such as lattice geometry and dimension, lattice constant, and interactions. Impurities and disorders can also be included in the system. The control and ability to tweak various parameters, otherwise impossible in real crystal, makes optical lattices an ideal testing ground for simulating the solid state crystals. The basic second quantized Hamiltonian of the interacting many-body system in external trapping potential in the grand canonical ensemble is written as

$$\begin{aligned} H = & \int d^3r \psi^\dagger(\mathbf{r}) \left( \frac{-\hbar^2}{2m} \nabla^2 + V_0(\mathbf{r}) + V_T(\mathbf{r}) - \mu \right) \psi(\mathbf{r}) \\ & + \frac{1}{2} \int d^3r \psi^\dagger(\mathbf{r}) \psi^\dagger(\mathbf{r}') V_{at}(\mathbf{r} - \mathbf{r}') \psi(\mathbf{r}) \psi(\mathbf{r}') \end{aligned} \tag{1.7}$$

where $\psi(\mathbf{r})(\psi^\dagger(\mathbf{r}))$ is a boson field operator which annihilates (creates) boson at

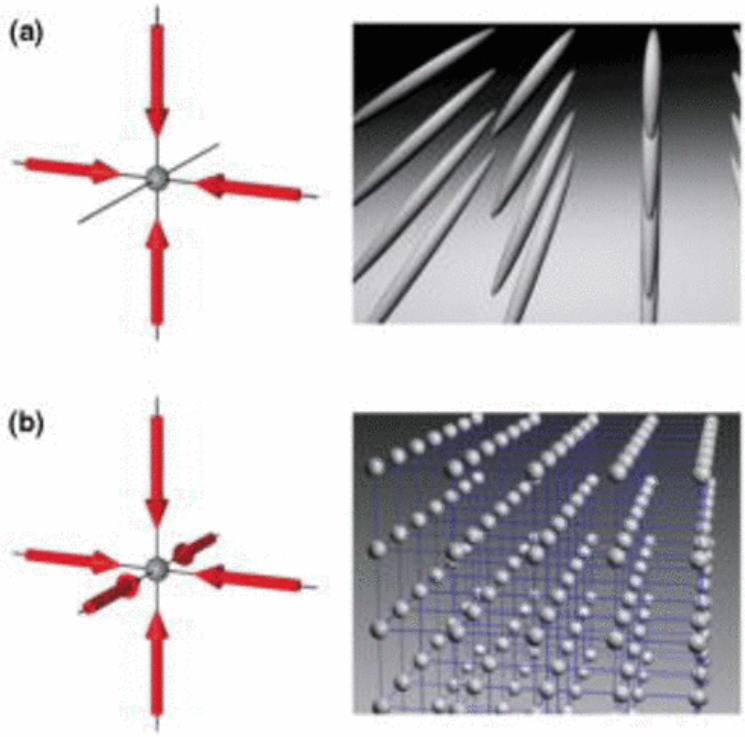


Figure 1.2: Optical lattices are formed by superimposing two and three pairs of lasers in a) 2D and b)3D. In a 2D optical lattice, the atoms are confined in array potentials represented by grey tubes and spheres in a 3D case. Figure courtesy: I.Bloch (2008) [21].

position $\mathbf{r}$, $V_0(\mathbf{r})$ is the periodic lattice potential, $V_T(\mathbf{r})$ denotes an additional slowly varying external trapping potential due to the magnetic trap, $\mu$ is the chemical potential which fixes the number of particles in the system and $V_{at}(\mathbf{r}-\mathbf{r}')$ is the interaction between the bosons at position $\mathbf{r}$ and $\mathbf{r}'$. In most of the cases, $V_{at}(\mathbf{r}-\mathbf{r}')$ decays as $|\mathbf{r}-\mathbf{r}'|$ value increases. For the dilute cold Bose gas, the only relevant scattering process is $s$ wave scattering, to a good approximation $V_{at}(\mathbf{r})$ is approximated isotropic short-ranged contact potential given by

$$V_{at}(\mathbf{r}-\mathbf{r}') = \frac{4\pi a_s \hbar^2}{m}\delta(\mathbf{r}-\mathbf{r}') \tag{1.8}$$

where $a_s$ is $s$ wave scattering length, and $m$ is the mass of atoms.

$$\begin{aligned} H = \quad & \int d^3r\psi^\dagger(\mathbf{r})\left(\frac{-\hbar^2}{2m}\nabla^2 + V_0(\mathbf{r}) + V_T(\mathbf{r}) - \mu\right)\psi(\mathbf{r}) \\ & + \frac{4\pi a_s\hbar^2}{2m}\int d^3r\psi^\dagger(\mathbf{r})\psi^\dagger(\mathbf{r})\psi(\mathbf{r})\psi(\mathbf{r}) \end{aligned} \tag{1.9}$$

Assuming the energies involved in the system dynamics are small in comparison to the excitation energies of the second band, the field operator, in terms of Wannier basis, keeping only the lowest vibrational states, can be written as

$$\psi(\mathbf{r}) = \sum_i \hat{a}_i w(\mathbf{r} - \mathbf{r}_i) \tag{1.10}$$

where $\hat{a}_i$ is the annihilation operator of the i$^{th}$ site and $w(\mathbf{r} - \mathbf{r}_i)$ is the Wannier function of the lowest vibrational band. Using this, we can approximate the Eq. 1.9 to a single band Bose-Hubbard model. For simplicity, approximating that particles only interact when they occupy the same site, the particle can only hop between the nearest neighbours, and hopping amplitude is negligible for higher-order hopping,

$$\hat{H} = -t \sum_{\langle ij \rangle} (\hat{a}_i \hat{a}_j^\dagger + h.c) + \frac{U}{2} \sum_i \hat{n}_i(\hat{n}_i - 1) - \mu \sum_i \hat{n}_i. \tag{1.11}$$

Here, we assumed a homogeneous lattice such that $t = t_{ij}$, $U = U_i$, and $\mu = \mu_i$ for all $i$ and nearest pair of sites $i, j$, and

$$t_{ij} = \int d^3 r w^*(\mathbf{r} - \mathbf{r}_i) \left( \frac{-\hbar^2}{2m} \nabla^2 + V_0(\mathbf{r}) \right) w(\mathbf{r} - \mathbf{r}_j) \tag{1.12}$$

$$U_i = \frac{4\pi a_s \hbar^2}{m} \int d^3 r |w(\mathbf{r} - \mathbf{r}_i)|^4 \tag{1.13}$$

$$\mu_i = \int d^3 r w^*(\mathbf{r} - \mathbf{r}_i) V_T(\mathbf{r}) w(\mathbf{r} - \mathbf{r}_i) \tag{1.14}$$

In equation 1.11, the $\hat{a}_i(\hat{a}_i^\dagger)$ is the annihilation (creation) operator, which annihilates (creates) particle at site $i$ and number operator $\hat{n}_i = \hat{a}_i^\dagger \hat{a}_i$ gives the number of particles at site $i$. The particle hop from the site $i$ to $j$ with the hopping amplitude and interacts on-site using on-site interaction strength $U$ (only comes into play when more than one particle occupies a site). The strength of $t$ and $U$ is less than the energy gap between the lowest vibrational bands. The chemical potential $\mu$ controls the number of particles in the system. Both $U$ and $t$ can be tuned using

the frequency and intensity of the laser beam used.

$$\frac{U}{t} = \frac{\sqrt{8}\pi a_s}{4a} \exp\left(\frac{2V_0}{E_r}\right) \tag{1.15}$$

where $a = \lambda/2$ is the lattice constant. The sign of the $U$ can be controlled using Feshbach resonances: for positive $U$, the model is repulsive and attractive for negative $U$.

The Bose-Hubbard model for $U > 0$ has two prominent phases at zero temperature, the superfluid phase for $U/t << 1$ and the Mott insulator for $U/t >> 1$, and the competition between $U$ and $t$ drives the transition from the superfluid to the Mott Insulator phase.

In the region, $t >> U$, the hopping term in the Eq. 1.11 dominates the on-site interaction. In the presence of weak $U$, bosons occupy the lowest energy state $k = 0$, forming a superfluid phase, described by a wavefunction

$$|\Psi_{\mathrm{SF}}\rangle \propto (a^\dagger_{k=0})^N |0\rangle \tag{1.16}$$

where $|0\rangle$ is the vacuum state. In the SF phase, all the bosons are delocalized on the entire lattice and are characterized by non-zero off-diagonal long-range ordering and phase coherence. Due to large fluctuations in the number of bosons per site, the SF phase has finite compressibility

$$\kappa = \frac{\partial \rho}{\partial \mu}. \tag{1.17}$$

In the strongly interacting regime, $U >> t$, the on-site interaction dominates the hopping amplitude. Bosons, for integer densities, are localized on the site forming the Mott insulator phase. The wavefunction in this phase is given by

$$|\Psi_{\mathrm{MI}}\rangle \propto (\Pi_i a^\dagger_i)^n |0\rangle \tag{1.18}$$

The MI phase is incompressible; the density remains the same with changes in

the chemical potential and is characterized by the absence of long-range ordering and loss of phase coherence. The excitation spectra of bosons in the MI phase are gapped. However, and the particle and hole excitations are gapless in the SF phase [22].

This quantum phase transition was predicted in the Bose-Hubbard Hamiltonian by Fisher *et.al.* [23] and later by Jaksch *et. al.* [17], and was later experimentally realized by M. Greiner *et. al.* [24] using BEC of $^{87}$Rb atoms and loading it in 3D optical lattices using the time of flight measurements. In these experiments, trapping potential is turned off, and the system's image is captured as the wavefunction of the bosons expands, as shown in Fig. 1.3. In the BEC phase, the bosons occupy the lowest momentum state $k = 0$, resulting in a sharp peak at $k = 0$. The central maxima here represent bosons having the lowest velocities and phase coherence. As the potential increases, in the weakly interacting regime, the bosons distribute themselves in the potential minima, and the Bragg peaks can be seen in the Fig. 1.3. The central peak vanishes in the strongly interacting regime, and the phase coherence is lost, representing the SF-MI transition. Subsequently, the SF-MI transition is also observed in 1D and 2D optical lattices [15], [25]–[27].

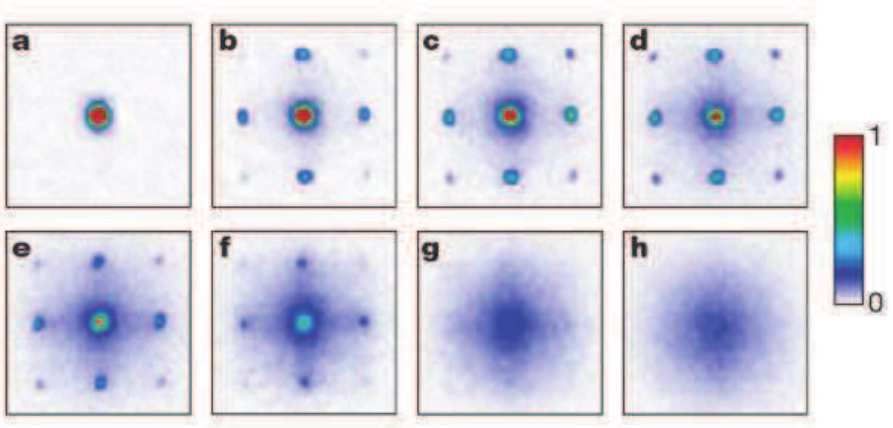


Figure 1.3: Time of flight images of matter-wave interference patterns for different optical lattice potentials a) 0, b)3 $E_r$, c)7Er, d)10$E_r$, e)13$E_r$, f) 14$E_r$, g) 16$E_r$, and h)20$E_r$ depicts phase transition from superfluid to Mott insulator phase. The potentials are measured using the recoil energy $E_r = \frac{\hbar^2 k^2}{2m}$. In the superfluid phase, the central peak is observed, and in the Mott insulator phase, the central peak is destroyed, and phase coherence is lost. Figure courtesy: M. Greiner(2002) [24].

The optical lattices thus provide us with ways to understand the complex

solid system with a simplified model. The control over system parameters like periodicity, dimensionality, and interactions make them ideal simulators of solids -this created the onset of various theoretical and experimental studies in this area.

The BH model is the simplest one describing the motion of ultra-cold bosons in optical lattices [17]. The exciting feature of this model is the SF to MI transition, which is similar to the metal to insulator transition in solid systems. BH models are not solvable even in one dimension, and various approximate and numerical methods are employed to solve these models. The mean-field theories [22], [23], [28] study large systems by converting them into single site/cluster problems by approximating the average field. In the random phase approximation [22], [29]–[32], the excitation spectra and the density of the state are calculated by approximating the phases. The quantum Monte Carlo [33], [34] and the Density Matrix Renormalization Group theory (DMRG) [35]–[37] are computational techniques applied to study the phases and phase transitions in the BH models for large system sizes under consideration. These methods have their advantages and limitations. The simplest method of all, the MFT correctly predicts the SF and MI phase, but it overestimates the SF phase boundaries [38]. The cluster mean-field theory (CMFT) improves the SF phase boundaries, but the Hilbert basis grows exponentially as the cluster size increases, increasing the computational resources required. The DMRG method, on the contrary, handles large system sizes and obtains the BH model's ground state properties with moderate computational resources. This method works well for the phases with a gap in the energy spectrum, such as the MI phase, but there is no direct way to observe the gapless superfluid phases using it.

## 1.2 Motivation

The optical lattice system predicts many exotic gapless phases by adding different interactions to the BH model. In experiments, the BEC is loaded in magneto-optical trapped, freezing the spin degrees of freedom. The spin degrees of freedom

are maintained by trapping the BEC in optical traps. The gapless phases, such as polar superfluid, are observed in this system defined by spin-1 Bose-Hubbard model [39]. The gapless phases, like supersolid and solitonic phases, are predicted in optical lattices with long-range interactions mapped by the extended Bose-Hubbard (EBH) model. Experimentally, this interaction is realized by trapping the magnetic and dipolar atoms in optical lattices [40]. The pair superfluid observed in the higher order on-site interactions resulting from the virtual transition to higher vibrational energy band [41] mapped by the BH model with three and higher body interactions.

Unlike MFT, the DMRG method cannot identify different gapless phases in these models, but MFT overestimates the phase boundaries. The CMFT improves the MFT results but at the cost of increased computational resources. This thesis aims to combine the simplicity of the CMFT method with the extensive system handling capabilities of the DMRG method to get the CMFT+DMRG method. Moreover, using the technique unravels phases and phase transitions in various extensions of BH models.

## 1.3 Objectives

Objectives proposed for this thesis are:

- Develop the CMFT+DMRG method in grand canonical ensemble
- Apply the CMFT+DMRG method to the Bose-Hubbard model to establish the method's working.
- Apply the method to the extended Bose-Hubbard model to predict the model's various phases and phase transitions.
- To understand the effect of three-body hardcore on-site interaction on the EBH model using the CMFT+DMRG method.

## 1.4 Overview

In Chapter 2, we first discuss the approximate methods used to study the Bose-Hubbard models, mainly focusing on the mean-field (MFT), cluster mean-field theory (CMFT), and DMRG methods. We discuss the Bose-Hubbard model in the MFT and CMFT framework, followed by a brief overview of the renormalization technique, and discuss the working of the DMRG method using the BH model. Next, combining these two methods, we put forward the framework of the CMFT+DMRG method for two cases-(i) translationally symmetric lattice and (ii) bipartite lattice. The CMFT-DMRG works in the grand-canonical ensemble. We first set up a cluster Hamiltonian of the desired size. We find the ground state of the cluster Hamiltonian using the DMRG iterative procedure self-consistently. In translationally invariant systems, we work with an even number of sites; however, for the bipartite system, an odd number of sites are preferred. The ground state properties used to characterize phases are calculated at the end of each iteration. We demonstrate that the CMFT+DMRG method predicts all the gapless phases with moderate computational resources. Furthermore, when the superfluid order parameter vanishes in the gapped phases, the CMFT Hamiltonian reproduces the earlier DMRG results.

In Chapter 3, we apply the CMFT+DMRG to the BH model and compare the results with the DMRG results. The superfluid order parameter $\psi_i$ and the boson density $\rho_i$ are calculated to predict the phases in the BH model. Both $\psi_i$ and $\rho_i$ converge with the length for all lattice sites. The effect of the fluctuations dampens as we move towards the center, causing the $\psi_i$ at the edges to converge to a higher value than at the center. The $\psi_i$ and $\rho_i$ at the center characterize the phases and phase transitions. In the SF (MI) phase, $\psi \neq 0 (\psi = 0)$ and the correlation function decays as a power law (exponentially). The structure factor and boson condensate fraction calculated using the correlations confirm the phase transitions. The CMFT+DMRG and DMRG results are found to agree with each

other. However, the convergence rate decreases towards the critical point due to the higher correlation length. A larger system size and density matrix basis are required to resolve the gap close to a critical point, which is difficult to determine with the CMFT+DMRG. The CMFT+DMRG and DMRG methods complement each other in studying the BH models; the former works well in the gapless phases, while the latter works in the gaped phase.

In Chapter 4, we apply CMFT+DMRG to the extended Bose-Hubbard model. In the EBH model, the nearest-neighbour interaction allows different boson densities at the neighbouring site. Due to this, we divide the entire lattice into $A-B$ sub-lattices and employ the CMFT+DMRG formalism. The superfluid order parameter and boson density for $A$ and $B$ sub-lattice at the center of the lattice are calculated along with the averages and correlations to predict the phases. We have calculated the EBH results in hard-core and soft-core regimes where new phases such as supersolid, density wave, solitons, and phase-separated phases are predicted. The EBH model maps into the spin 1/2 XXZ model in the hard-core limit, and we reproduce the BKT transition from superfluid to density wave phase. We obtain the phase-separated phase and compare the co-existence of superfluid and density ave/supersolid phases using the DMRG technique. We determine the phase diagram for different regions of the parameter space. Finally, we study the effect of attractive three-body hard-core on-site potential in the EBH model using the CMFT+DMRG method.

All the results are summarized and concluded in Chapter 5. The prospects of the future work are also discussed there.

CHAPTER 2

# Methods

## 2.1 Introduction

The Bose-Hubbard systems are excellent arenas to simulate the motion of ultracold bosons in optical lattices. However, it takes work to solve the Bose-Hubbard-like models. For example, the simplest Bose-Hubbard model, which contains only the hopping of bosons between nearest neighbour sites and on-site interaction, is not solvable even in one dimension. Our understanding of the possible phases and the underlying phase transitions in the Bose-Hubbard model is based on several approximate and numerical techniques. These studies include simple mean-field theories [22], [23], [28], strong-coupling-expansion (SCE) techniques [42], [43] and numerically accurate methods such as quantum Monte Carlo simulation [33], [34], density matrix renormalization group (DMRG) [35], [44], [45] and time-evolving block decimation (TEBD) method [46], [47].

We focus our study on one-dimensional systems. The approximate and numerical techniques mentioned above have advantages and limitations when applied to one-dimensional models. For example, though the mean-field theory predicts overall phases correctly, it is known to overestimate the phase boundaries, especially in one dimension. For instance, mean-field theory predicts critical on-site interaction $U_C/t = 11.6$ for Mott insulator to superfluid transition in one-dimensional Bose-Hubbard model with density $\rho = 1$ [22]. On the other hand, the numerical methods

are more accurate ($U_C/t \approx 3.3$ [35], [44], [45]). Numerical methods, however, come with high computational costs in predicting phases and their boundaries. This fact is especially true when studying and characterizing the gapless superfluid phases.

In this chapter, we discuss our formalism. For the sake of completeness, we discuss the single-site mean-field theory (MFT), its extension to cluster mean-field theory (CMFT), and the density matrix renormalization method (DMRG). These discussions lay the foundation for developing the cluster mean-field theory plus density matrix renormalization (CMFT+DMRG) method. In this approach, we combine the simplicity of the CMFT and the numerical accuracy of DMRG.

### 2.1.1 Single Site Mean-Field Theory

The mean-field theory described for the Bose-Hubbard model

$$\hat{H} = -t \sum_{\langle ij \rangle} (\hat{a}_i \hat{a}_j^\dagger + h.c) + \frac{U}{2} \sum_i \hat{n}_i(\hat{n}_i - 1) - \mu \sum_i \hat{n}_i. \tag{2.1}$$

follows the work of Sheshadri *et al.* [22]. In Eq. (2.1), $\hat{a}_i^\dagger$ ($\hat{a}_i$) are boson creation (annihilation) operators, and number operator $\hat{n}_i = \hat{a}_i^\dagger \hat{a}_i$. The first term represents the hopping of bosons between nearest neighbouring sites with amplitude $t > 0$. The second term is the on-site interaction between the bosons, which increases the system's energy by $U$ whenever there is more than one boson per site. The last term controls the boson number for a given chemical potential $\mu$.

The conventional mean-field approach applied to Fermionic or spin systems decouples the two-particle interaction term, i.e., the on-site interaction term in the Hamiltonian in Eq. (2.1), to map the problem into an effective one-particle Hamiltonian. This decoupling approach, however, fails to explain the Mott insulator phase. The ground state of the effective one-particle Hamiltonian is always in the superfluid phase. The unique feature of the mean-field theory described by Sheshadri *et al.* [22] is that it decouples the hopping term (first term in Eq. (2.1)), which connects two nearest neighbouring sites, thus mapping the Hamiltonian

into the one-site problem. We first discuss the single-site mean-field theory. The hopping term in Eq. (2.1) $\hat{a}_i^\dagger \hat{a}_j$ is decoupled using the mean-field decoupling approximation $\hat{a_j} = \langle \hat{a}_j \rangle + \delta \hat{a}_j$ as shown in Fig. 2.1. Here $\delta \hat{a}_j$ is the fluctuation over the mean value $\langle \hat{a}_j \rangle$. Applying this approximation to the Bose-Hubbard Hamiltonian in Eq. ( 2.1), the hopping term is decoupled into

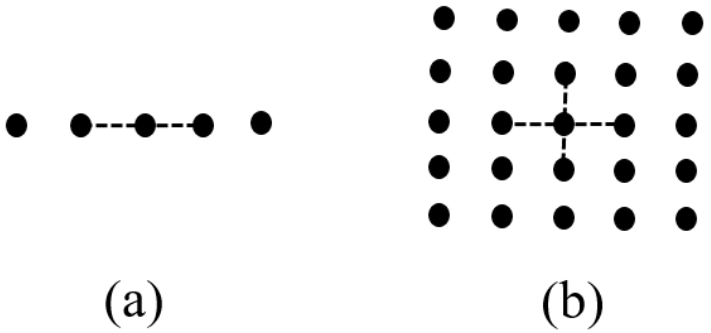


Figure 2.1: Site configuration of (a) one-dimensional and (b) two-dimensional system. The dotted line represents the hopping term approximated using the mean-field decoupling $\langle \hat{a}_j \rangle + \delta \hat{a}_j$.

$$\hat{a}_i^\dagger \hat{a}_j = \langle \hat{a}_i^\dagger \rangle \langle \hat{a}_j \rangle + \langle \hat{a}_i^\dagger \rangle \delta \hat{a}_j + \langle \hat{a}_j \rangle \delta \hat{a}_i^\dagger + \delta \hat{a}_i^\dagger \delta \hat{a}_j \tag{2.2}$$

Assuming $\delta \hat{a}_j$ to be very small, we neglect the quadratic term $\delta \hat{a}_i^\dagger \delta \hat{a}_j$ in the fluctuation, which leads to the approximation

$$\begin{aligned} \hat{a}_i^\dagger \hat{a}_j &\approx \langle \hat{a}_i^\dagger \rangle \langle \hat{a}_j \rangle + \langle \hat{a}_i^\dagger \rangle \delta \hat{a}_j + \langle \hat{a}_j \rangle \delta \hat{a}_i^\dagger \\ &= \langle \hat{a}_i^\dagger \rangle \hat{a}_j + \langle \hat{a}_j \rangle \hat{a}_i^\dagger - \langle \hat{a}_i^\dagger \rangle \langle \hat{a}_j \rangle = \psi_i \hat{a}_j + \psi_j \hat{a}_i^\dagger - \psi_i \psi_j \end{aligned} \tag{2.3}$$

where $\langle \hat{a}_i \rangle = \psi_i$ is the superfluid order parameter, and it is taken to be real $\psi_i = \psi_i^*$ [22]. Bose-Hubbard model ( 2.1) is translationally invariant, i.e., $\psi_i = \psi$ for all $i$. We rewrite the hopping term in the Eq. (2.1) as

$$-t \sum_{\langle i,j \rangle} \left( \hat{a}_i^\dagger \hat{a}_j + \hat{a}_j^\dagger \hat{a}_i \right) = -t \sum_{\langle i,j \rangle} \Big( (\psi \hat{a}_i + \psi \hat{a}_i^\dagger - \psi^2) + (\psi \hat{a}_j + \psi \hat{a}_j^\dagger - \psi^2) \Big) \tag{2.4}$$

Changing the index form $j$ to $i$ in the second term in the bracket and dividing by

two to avoid double counting, we get

$$-t\sum_{\langle i,j\rangle}\left(\hat{a}_i^\dagger\hat{a}_j+\hat{a}_j^\dagger\hat{a}_i\right)=-zt\sum_i\left((\hat{a}_i+\hat{a}_i^\dagger)\psi-\psi^2\right) \tag{2.5}$$

where $z = 2d$ is the coordination number and $d$ is the dimension. As a result of this approximation, the Hamiltonian (2.1) is approximated to

$$\hat{H}=\sum_i\hat{H}_i^{\mathrm{MF}} \tag{2.6}$$

where the mean-field Hamiltonian

$$\hat{H}_i^{\mathrm{MF}}=-zt\left(\hat{a}_i+\hat{a}_i^\dagger\right)\psi+zt\psi^2+\frac{U}{2}\hat{n}_i(\hat{n}_i-1)-\mu\hat{n}_i. \tag{2.7}$$

The single site Hamiltonian (2.7) is easily solved by an iteration procedure described below

- For initial value of $\psi$, we construct $\hat{H}_i^{\mathrm{MF}}$ in the Fock state basis $\{|n\rangle\}$ where $n = 0, 1, 2, ...., n_{\max}$. Here $n_{\max}$ is the maximum number of bosons that occupy per site. It may be noted that for bosons, $n_{\max} = \infty$. However, for the numerical calculation, we keep a finite value for $n_{\max}$ and examine the convergence of the ground state energy by varying the $n_{\max}$. We find $n_{\max}$ depends on the density of the bosons $\rho$ and the ratio of $U/t$. The larger the density, the larger should be the value of $n_{\max}$. However, for a larger value of $U/t$, we can keep smaller $n_{\max}$. For example, in the hard-core limit ($U \to \infty$), $n_{\max} = 1$ and analytical solution exist for the mean-field Hamiltonian (2.7) [22].

- The Hamiltonian matrix is diagonalized to obtain the ground state energy $E_{GS}$ and the wavefunction $|\Psi_{GS}\rangle = \sum_{n=0}^{\mathrm{n_{max}}} C_n|n\rangle$.

- Using the ground state $|\Psi_{GS}\rangle$, we re-calculate the superfluid order parameter $\psi' = \langle\hat{a}\rangle = \langle\Psi_{GS}|\hat{a}|\Psi_{GS}\rangle$.

- If $\psi \neq \psi'$, $\psi$ is replaced by $\psi'$ in $\hat{H}_i^{\mathrm{MF}}$ to re-calculate $E_{GS}$ and $|\Psi_{GS}\rangle = \sum_{n=0}^{\mathrm{n_{max}}} C_n|n\rangle$.

- The iteration process is repeated for self consistently till the $\psi$ is converged to the desired accuracy.

- The superfluid density $\rho_{SF} = |\psi|^2$ and boson density $\rho = \langle\Psi_{GS}|\hat{n}|\Psi_{GS}\rangle$ are then calculated from the converged ground state $|\Psi_{GS}\rangle$ to characterize different phases of the model.

The BH model has global $U(1)$ symmetry, i.e., it is invariant under the transformation

$$\hat{a}_i \rightarrow \hat{a}_i e^{i\phi} \tag{2.8}$$

In the superfluid (SF) phase, the finite value of $\psi$ spontaneously breaks the global $U(1)$ symmetry and does not conserve the total number of bosons. However, in the Mott insulator phase, $\psi = 0$ and its phase preserves the $U(1)$ symmetry. The ground state of the Mott insulator is a product of the Fock states. Hence, the value of $\psi$ characterizes the SF to MI phases transition in the BH model. The simple MFT, thus, correctly predicts the phase transition from SF to MI phase [22], [23].

The primary inadequacy of the MFT is that it neglects the fluctuations in the critical region of the phase transition. The fluctuations destroy the condensate, and ignoring the fluctuations leads to overestimating the phase boundary [48]. One way to improve the estimation of the phase boundary is to construct a larger cluster of sites while constructing the mean-field theory instead of a single site. We discuss the cluster mean-field view in the following sub-section.

### 2.1.2 Cluster Mean-Field Theory

The cluster mean-field theory (CMFT) is an extension of the single-site MFT, where we consider a cluster of sites in the build-up of mean-field Hamiltonian [48], [49]. The cluster is decoupled from the rest of the lattice using the mean-field approximation discussed in the sub-section 2.1.1. We first divide the whole lattice


Figure 2.2: Site configuration of the one-dimensional system for cluster size with (a) one site and (b) two sites. The solid line represents the exact hopping within the cluster, and the dotted lines represent the hopping term approximated using the mean-field decoupling $\langle \hat{a}_j \rangle + \delta \hat{a}_j$.

into $N_C$ clusters of equal length $L$. For example, Fig. 2.2(a) and (b) show a cluster consisting of one site and two sites. The BH Hamiltonian (2.1) is then written as

$$\hat{H} = \sum_p \hat{H}_p^{loc} + \sum_p \hat{H}_p^{hop} \tag{2.9}$$

where $p$ represents the cluster index, and $\hat{H}_p^{loc}$ is the local Hamiltonian of the $p^{\text{th}}$ cluster, which is given by

$$\hat{H}_p^{loc} = -t \sum_j \left( \hat{a}_{p,j+1}^\dagger \hat{a}_{p,j} + \hat{a}_{p,j}^\dagger \hat{a}_{p,j+1} \right) + \frac{U}{2} \sum_j \hat{n}_{p,j}(\hat{n}_{p,j} - 1) - \sum_j \mu \hat{n}_{p,j}. \tag{2.10}$$

Here $\hat{a}_{p,j}^\dagger$ ($\hat{a}_{p,j}$) is the boson creation (annihilation) operator and $\hat{n}_{p,j} = \hat{a}_{p,j}^\dagger \hat{a}_{p,j}$ is the number operator for the site $j$ in the cluster $p$. The second term in the Hamiltonian Eq. (2.9) represents the hopping of bosons between the clusters and is given by

$$\hat{H}_p^{hop} = -t \left( \hat{a}_{p,1}^\dagger \hat{a}_{p-1,L} + \hat{a}_{p-1,L}^\dagger \hat{a}_{p,1} \right) - t \left( \hat{a}_{p,L}^\dagger \hat{a}_{p+1,1} + \hat{a}_{p+1,1}^\dagger \hat{a}_{p,L} \right), \tag{2.11}$$

where first term represents hopping between site $L$ of cluster $p-1$ and site 1 of cluster $p$ and the second term represents hopping between site $L$ of cluster $p$ and site 1 of the cluster $p+1$ as shown in Fig. 2.3.

We now decouple cluster $p$ from its neighbour clusters by using standard mean-field decoupling, i.e., $\hat{a}_{p,j} = \langle \hat{a}_{p,j} \rangle + \delta \hat{a}_{p,j}$ where $\langle \hat{a}_{p,j} \rangle = \psi_{p,j}$. Decoupling $p$ from

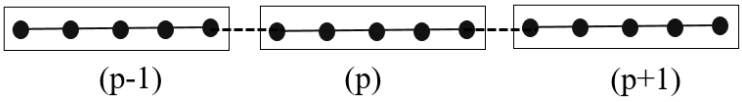


Figure 2.3: Site configuration of the one-dimensional system for cluster size L. Here, the cluster $p$ is decoupled from the neighbouring clusters, $p-1$ and $p+1$, using the mean-field decoupling. The dotted line represents the approximated hopping between the clusters.

$p-1$ cluster

$$\hat{a}^{\dagger}_{p,1}\hat{a}_{p-1,L} + \hat{a}^{\dagger}_{p-1,L}\hat{a}_{p,1} = \hat{a}^{\dagger}_{p,1}\psi_{p-1,L} + \hat{a}_{p,1}\psi^{*}_{p-1,L} + \hat{a}^{\dagger}_{p-1,L}\psi_{p,1} + \hat{a}_{p-1,L}\psi^{*}_{p,1} - \left(\psi^{*}_{p-1,L}\psi_{p,1} + \psi_{p-1,L}\psi^{*}_{p,1}\right) + \delta\hat{a}^{\dagger}_{p,1}\delta\hat{a}_{p-1,L} + \delta\hat{a}^{\dagger}_{p-1,L}\delta\hat{a}_{p,1} \tag{2.12}$$

Considering the fluctuation $\delta a_{p,j}$ to be small and thus neglecting second-order fluctuations, we approximate the above term for cluster $p$ to

$$\hat{a}^{\dagger}_{p,1}\hat{a}_{p-1,L} + \hat{a}^{\dagger}_{p-1,L}\hat{a}_{p,1} \approx \hat{a}^{\dagger}_{p,1}\psi_{p-1,L} + \hat{a}_{p,1}\psi^{*}_{p-1,L} - \frac{1}{2}\left(\psi^{*}_{p-1,L}\psi_{p,1} + \psi_{p-1,L}\psi^{*}_{p,1}\right), \tag{2.13}$$

we multiply the third term by $1/2$ to account for the double counting. Similarly, decoupling $p$ from cluster $p+1$,

$$\hat{a}^{\dagger}_{p,L}\hat{a}_{p+1,1} + \hat{a}^{\dagger}_{p+1,1}\hat{a}_{p,L} \approx \hat{a}^{\dagger}_{p,L}\psi_{p+1,1} + \hat{a}_{p,L}\psi^{*}_{p+1,1} - \frac{1}{2}\left(\psi^{*}_{p+1,1}\psi_{p,L} + \psi_{p+1,1}\psi^{*}_{p,L}\right). \tag{2.14}$$

Assuming, without loss of generality, the superfluid order parameter $\psi_{p,j}$ to be real and homogeneous, Eq. (2.11) is written as

$$\hat{H}^{hop}_{p} = -t\left((\hat{a}^{\dagger}_{p,1} + \hat{a}_{p,1})\psi - \psi^{2}\right) - t\left((\hat{a}^{\dagger}_{p,L} + \hat{a}_{p,L})\psi - \psi^{2}\right). \tag{2.15}$$

Using Eqs. (2.10) and (2.15) in Eq. (2.9), we get

$$\hat{H} = \sum_{p} \hat{H}_p^C \tag{2.16}$$

where $\hat{H}_p^C$ is the Hamiltonian for a cluster of $L$ sites. Dropping the cluster index $p$

$$\begin{aligned}\hat{H}^C = &- t \sum_{j=1}^{L-1} \left( \hat{a}_{j+1}^\dagger \hat{a}_j + \hat{a}_j^\dagger \hat{a}_{j+1} \right) + \frac{U}{2} \sum_{j=1}^{L} \hat{n}_j (\hat{n}_j - 1) - \sum_{j=1}^{L} \mu \hat{n}_j \\ &- t \left( (\hat{a}_1^\dagger + \hat{a}_1)\psi - |\psi|^2 \right) - t \left( (\hat{a}_L^\dagger + \hat{a}_L)\psi - |\psi|^2 \right). \end{aligned} \tag{2.17}$$

The analytical solution of the cluster Hamiltonian is not possible even in the hard-core limit. The numerical solution of Eq. (2.17) follows the iterative procedure described below.

- For the initial guess of $\psi$, Hamiltonian matrix is constructed on the Fock state basis $\{|n_1, n_2, ..., n_L\rangle\}$, where $n_i = 0, 1, 2, ...., n_{\max}$ and $i = 1, 2, ..., L$. The dimension of the Hilbert space of cluster Hamiltonian is $(\mathrm{n_{max}} + 1)^{\mathrm{L}}$ in the Fock basis.

- The Hamiltonian $\hat{H}^C$ is diagonalized to obtain the ground state energy $E_{GS}$ and wavefunction $|\Psi_{GS}\rangle = \sum_{n_1,n_2,...,n_L=0}^{\mathrm{n_{max}}} C_{n_1,n_2,....,n_L} |n_1, n_2, ....., n_L\rangle$.

- Using the ground state wavefunction, we re-estimate the superfluid order

parameter $\psi'$;

$$\begin{aligned}
\psi_i' &= \langle \hat{a}_i \rangle = \langle \Psi_{GS} | \hat{a}_i | \Psi_{GS} \rangle \\
&= \sum_{n_1,n_2,\cdots,n_i,\cdots,n_L=0}^{\mathrm{n_{max}}} \quad \sum_{n_1',n_2',\cdots,n_i',\cdots,n_L'=0}^{\mathrm{n_{max}}} C^*_{n_1',n_2',\cdots,n_i',\cdots,n_L'} C_{n_1,n_2,\cdots,n_i,\cdots,n_L} \\
&\qquad \langle n_1', n_2', \cdots, n_i', \cdots, n_L' | \hat{a}_i | n_1, n_2, \cdots, n_i, \cdots, n_L \rangle \\
&= \sum_{n_1,n_2,\cdots,n_i,\cdots,n_L=0}^{\mathrm{n_{max}}} \quad \sum_{n_i'=0}^{\mathrm{n_{max}}} C^*_{n_1,n_2,\cdots,n_i',\cdots,n_L} C_{n_1,n_2,\cdots,n_i,\cdots,n_L} \\
&\qquad \langle n_1, n_2, \cdots, n_i', \cdots, n_L | \hat{a}_i | n_1, n_2, \cdots, n_i, \cdots, n_L \rangle \quad (2.18)
\end{aligned}$$

- Replacing $\psi$ with $\psi'$, we re-calculate Hamiltonian 2.17 and diagonalized to obtain $E_{GS}$ and $|\Psi_{GS}\rangle$.

- The iterative process is repeated till $\psi$ is calculated self-consistently.

After calculating the superfluid order parameter $\psi$ self-consistently, boson density $\rho$ is obtained from the ground state wavefunction $\Psi_{GS}$. Different phases are characterized based on the behavior of $\psi$ and $\rho$. In the limit $L = 1$, Eq. (2.17) reproduces the single site mean-field theory Hamiltonian [22], [28]. McIntosh et al. have considered this Hamiltonian with cluster size up to $L = 8$ [48]. The CMFT results of BH models show the improvement in the phase boundaries with the increasing cluster size.

There are certain advantages with the CMFT compared to the single-site MFT. The CMFT method incorporates fluctuations neglected by the single-site MFT to some extent since the hopping within the cluster is treated precisely. Calculating the superfluid order parameter improves with the cluster size $L$, thus better estimating the phase boundaries. However, the CMFT method comes with certain limitations. The Hilbert space grows exponentially with the cluster size, requiring substantial computational resources to study larger cluster systems. In this context, the density matrix renormalization group (DMRG) technique is more accurate in handling larger system sizes. We review the DMRG method in the

following sub-section below before combining CMFT and DMRG methods in sub-section 2.1.4.

### 2.1.3 Density-Matrix Remormalization Group Theory

The density-matrix renormalization (DMRG) method [50], [51] is a powerful numerical technique for solving 1D systems. With moderate computational resources, the DMRG method provides highly accurate results for the ground and low-lying excited states, allowing us to analyze and understand the physical properties of condensed matter systems.

The DMRG method is based on the numerical renormalization (RG) method, a breakthrough technique in solving the Kondo problem [52]. The real-space version of the RG method (RSRG) assumes that only the lowest eigenstates dominate in forming the states of larger blocks and iteratively growing the system size. We briefly describe the iterative procedure of RSRG applied to 1-D systems below.

- The one-dimensional infinite chain is divided into identical blocks $A$ of length $L$. Let the basis of $M$ states $\{|\mu_A\rangle\}$ represent the block $A$.

- Two neighbouring blocks are grouped into a superblock, denoted by $A' \equiv AA$ having length $2L$ as shown in Fig. 2.4. The Hilbert's space of superblock $A'$ is $M^2$. The Hamiltonian $\hat{H}_{A'}$ is constructed and diagonalized

$$\hat{H}_{A'}|\alpha\rangle = E_\alpha|\alpha\rangle \tag{2.19}$$

  to obtain eigenstates

$$|\alpha\rangle = \sum_{\mu_A,\mu'_A} C^\alpha_{\mu_A,\mu'_A}|\mu_A\mu'_A\rangle \tag{2.20}$$

  and energy $E_\alpha$.

- We truncate the basis states of superblock $A'$ from $M^2$ to $M$ using $M$ lowest

eigenstates of $H_{A'}$. Thus, superblock $A'$ is represented by $M$ lowest eigenstates of $H_{A'}$.

- The above process is repeated with new block $A' \rightarrow A$.
- The length of the superblock doubles at each iteration, and the process is repeated till the system reaches the desired length.

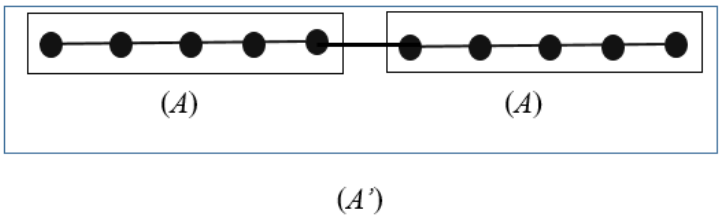


Figure 2.4: Schematic representation of RSRG for 1D system.

Restricting the number of states in the superblock to $M$ lowest energy states controls the Hilbert space dimension from growing exponentially, reducing the computational cost required to study the large system sizes. However, the RSRG method has yet to be successful in the calculation of the ground state energy. The basis states $\{|\mu_A\rangle\}$ representing the block $A$ is the eigen states of $\hat{H}_A$. Since $\hat{H}_A$ is diagonalized with open boundary conditions, state $\{|\mu_A\rangle\}$ has nodes at the edges. Therefore, $|\alpha\rangle = \sum_{\mu_A,\mu'_A} C^{\alpha}_{\mu_A,\mu'_A} |\mu_A \mu'_A\rangle$ also has nodes at the center of the system where the two $A$ Blocks meet. The presence of these nodes means states $|\alpha\rangle$, which represents the superblock $A'$, do not represent true low energy states, leading to errors in determining the ground state energy.

Eliminating the edge effect by changing the boundary conditions on a block and retaining the states with different boundary conditions improves the ground state energy[50], [51]. The DMRG technique, discussed below, is the consequence of these studies.

The principle idea behind the DMRG technique lies in the approach chosen to truncate the block's exponentially growing Hilbert space dimension. In DMRG, the most weighted eigenstates of the block density matrix are selected as states representing the block, unlike the lowest eigenstates as in RSRG. To demonstrate

this, we consider a superblock $SE$ with an open boundary condition comprising two identical blocks $S$ and $E$. Here, $S$ stands for the system and $E$ for the environment. Let $\{|\mu_S\rangle\}$ and $\{|\mu_E\rangle\}$ represent $M$ basis states of the blocks $S$ and $E$ respectively. We can write the states of the superblock system $SE$ in terms of $|\mu_S\rangle$ and $|\mu_E\rangle$ as

$$|\Psi\rangle = \sum_{\mu_S=1}^{M} \sum_{\mu_E=1}^{M} C_{\mu_S,\mu_E} |\mu_S\rangle|\mu_E\rangle. \tag{2.21}$$

Integrating the environment block $E$, we get the reduced density matrix of system block $S$ i.e.,

$$\rho^S_{\mu_S\mu'_S} = \sum_{\mu_E} C^*_{\mu_S,\mu_E} C_{\mu'_S,\mu_E}. \tag{2.22}$$

Diagonalising $\rho^S_{\mu_S\mu'_S}$ we get the eigenvalue $\omega_\alpha$ and eigenvector

$$|u_\alpha\rangle = \sum_{\mu_S} O^\alpha_{\mu_S} |\mu_S\rangle \tag{2.23}$$

of the density matrix. The eigenvalue $\omega_\alpha$ is nothing but the probability that the superblock state $|\Psi\rangle$ contains block state $\mu_S$ and satisfies $\sum_\alpha \omega_\alpha = 1$. Keeping the highest weighted states, say $m$ states such that $\sum_{\alpha=1}^{m} \omega_\alpha \approx 1$, the dimension of the Hamiltonian of the block is effectively reduced from $M$ to $m$ states. The $m$ eigenstates of the reduced density matrix $|u_\alpha\rangle$ represent the system block $S$. Similarly, the environment block $E$ is then represented by the $m$ eigenstates of the reduced density matrix $|v_\alpha\rangle$, where

$$|v_\alpha\rangle = \sum_{\mu_E} O^\alpha_{\mu_E} |\mu_E\rangle. \tag{2.24}$$

The state of the superblock system

$$|\Psi\rangle \approx \sum_{\alpha,\alpha'=1}^{m} a_{\alpha\alpha'} |u_\alpha\rangle|v_{\alpha'}\rangle. \tag{2.25}$$

We discuss the iterative process to calculate the ground state of the system using the DMRG method below. It is a stable procedure, as the truncation error from

the previous iteration does not propagate to the next iteration. Figure 2.5 gives the Schematic of the DMRG method.

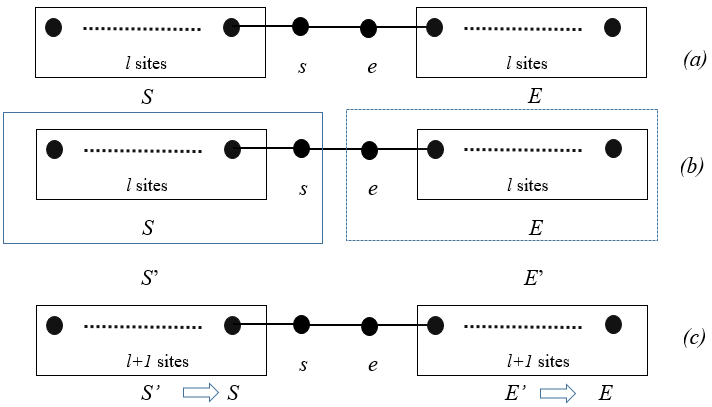


Figure 2.5: Schematic representation of DMRG iteration for the 1D system. (a) A superblock consists of the system block $S$ and the environment block $E$, and the two sites $(s, e)$, (b) Single site $s$ is added to the system block $S$ to form new system block $S'$ and (c) the new superblock is formed replacing $S$ with $S'$ and $E$ with $E'$, and two new sites $s$ and $e$.

**Step I** Consider a superblock configuration consisting of system block $S$ with $l$ sites, environment block $E$ with $l$ sites and two single sites $s$ and $e$ as shown in the Fig. 2.5(a). $l = 1$ in the first iteration and it increases from $l$ to $l + 1$ in every iteration. The Hilbert space dimension of the system block $S$ (environment block $E$) and the two sites are, say, $M_S$ and $N_s$, respectively. $M_S = N_s$ in the first iteration since $l = 1$. The superblock has $L = 2l + 2$ sites. Let $|\mu_{S(E)}\rangle$ represent the basis states for the system (environment) block. Similarly $|\sigma_{s(e)}\rangle$ represents the basis states for the single site $s(e)$.

**Step II** The Hamiltonian of the superblock

$$\hat{H}_{2l+2} = \hat{H}_S + \hat{H}_s + \hat{H}_e + \hat{H}_E + \hat{H}_{Ss} + \hat{H}_{se} + \hat{H}_{eE} \tag{2.26}$$

where $\hat{H}_S$ ($\hat{H}_E$) is the system (environment) block Hamiltonian, $\hat{H}_{s(e)}$ is the single site Hamiltonian, $\hat{H}_{Ss}$ is the Hamiltonian connecting the system block $S$ with the single site $s$, $\hat{H}_{se}$ is the Hamiltonian connecting the single site $s$ with the single site $e$, and finally $\hat{H}_{eE}$ is the Hamiltonian connecting the

single site $e$ with the environment block $E$.

**Step III** Construct the Hamiltonian $\hat{H}_{2l+2}$ and diagonalize it to obtain ground state energy $E_{GS}$, the wave function

$$|\Psi_{GS}\rangle = \sum_{\mu_S,\sigma_s,\sigma_e,\mu_E} C_{\mu_S\sigma_s\sigma_e\mu_E}|\mu_S\sigma_s\sigma_e\mu_E\rangle. \tag{2.27}$$

Calculate the expectation values of various operators and the correlation functions at this stage using the ground state wavefunction $|\Psi_{GS}\rangle$.

**Step IV** Construct the new system block $S'$ combining the system block $S$ and the single site $s$, i.e., $S' = S + s$ as shown in Fig. 2.5(b). Construct the reduced density matrix of $S'$.

$$\hat{\rho}_{\mu_S\sigma_s,\mu'_S\sigma'_s} = \sum_{\mu_E\sigma_e} C^*_{\mu_S\sigma_s\sigma_e\mu_E} C_{\mu'_S\sigma'_s\sigma_e\mu_E} \tag{2.28}$$

**Step V** Digonalize $\hat{\rho}_{\mu_S\sigma_s,\mu'_S\sigma'_s}$ to obtain the eigenvalues $\omega_\alpha$ and eigenstates

$$|u_\alpha\rangle = \sum_{\mu_S,\sigma_s} O^\alpha_{\mu_S\sigma_s}|\mu_S\sigma_s\rangle. \tag{2.29}$$

$\omega_\alpha$ measures the weight of the state $|u_\alpha\rangle$ in the ground state $|\Psi_{GS}\rangle$ and satisfy $\sum_\alpha \omega_\alpha = 1$.

**Step VI** New system blocks $S'$ has $M_S \times N_s$ states. We transform the basis states for $S'$ from $|\mu_S\sigma_s\rangle$ to $|u_\alpha\rangle$ keeping $M_S$ eigenstates with the largest $\omega_\alpha$. This way, we have truncated the Hilbert basis of the system block $S'$ from $M_S \times N_s$ to $M_S$. This step is the most critical step of the DMRG method. Hamiltonian $\hat{H}_{S'}$ for the new system block $S'$ and other operators are transformed from the old basis $\{|\mu_S\sigma_s\rangle\}$ to new basis $\{|u_\alpha\rangle\}$

$$\hat{H}^{new}_{S'} = O^\dagger \hat{H}^{old}_{S'} O \tag{2.30}$$

where $O$ is the transformation matrix in Eq. (2.29) and

$$\hat{H}^{old}_{S'} = \hat{H}_S + \hat{H}_s + \hat{H}_{Ss}. \tag{2.31}$$

**Step VII** Replace the system block $S$ with $S'$ and similarly environment block $E$ with $E'$ as shown in Fig. 2.5(c) and repeat from **[Step I]**.

The DMRG method works well when the ground state has a gap in the energy spectrum [50], [51], [53]. When applied to the Bose-Hubbard model, the superfluid and Mott insulator phases are determined by analyzing the behavior of the gap in the energy spectrum and the correlation functions such as single-particle density matrix $\langle \hat{a}^\dagger_j \hat{a}_{j+r} \rangle$ and density-density correlation $\langle \hat{n}_j \hat{n}_{j+r} \rangle$ [35], [44], [54]. These studies have elucidated the phase diagram of the model accurately [35], [44], [54].

However, the DMRG method, applied to Bose-Hubbard-like systems, can't be used to determine the superfluid order parameter $\psi$, which is the order parameter distinguishing superfluid to Mott insulator phases. Since it generally works in the canonical ensemble, $\psi = \langle \hat{a} \rangle = 0$ in all the phases. Several extensions of the Bose-Hubbard model, like the extended Bose-Hubbard model and the spin-1 Bose-Hubbard model, show novel exotic gapless phases like supersolid, polar/Ferro superfluid, phase separation, and pair superfluids. The superfluid order parameters are convenient to characterize these exotic gapless phases. Unlike the mean-field theories, the DMRG method can't resolve these phases directly due to its limitation in determining superfluid order parameters. In the following section, we provide a new approach that utilizes the DMRG capability to handle larger system sizes and the simplicity of the CMFT method to determine the superfluid order parameter.

### 2.1.4 Cluster mean-field Plus Density matrix Renormalization Group Method

The CMFT improves the phase boundary compared to simple single-site mean-field theory [48], [49]. However, there are limitations forming bigger cluster sizes for the CMFT calculations as the Hilbert space of the cluster increases exponentially with the number of sites. There have been recent reports of overcoming this limitation to build larger cluster sizes using the CMF + S analysis with 2D DMRG solver [55]–[57]. In this section, we provide a different approach that utilizes the

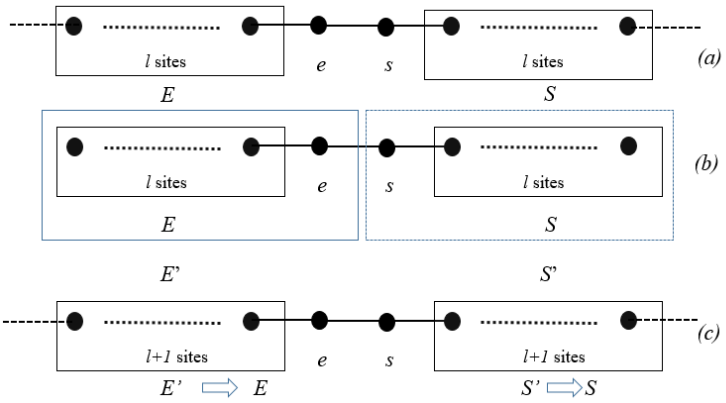


Figure 2.6: Schematic representation of CMFT+DMRG iteration for the 1D system. (a) A superblock consists of the system block $S$ and the environment $E$ and the two sites $(s, e)$, (b) The single site $s$ is added to the system block $S$ to form new system block $S'$ and (c) new superblock is formed replacing $S$ with $S'$ and $E$ with $E'$ and two new sites $s$ and $e$.

DMRG capability to handle larger system sizes and the simplicity of the CMFT method. We solve large cluster Hamiltonian using the DMRG procedure to provide a direct probe into the gapless phases using the superfluid order parameters. In this way, this new approach captures the success of both the DMRG and the CMFT methods.

We discuss the CMFT+DMRG method for two cases: lattice with translational symmetry and bipartite lattice. In the former, the superblock configuration of the DMRG is kept unchanged, while in the latter case, the configuration is modified to accommodate the bipartite symmetry of the wave function.

#### 2.1.4.1 Translational Symmetry Case

Here, we explain the CMFT+DMRG formalism using the Bose-Hubbard model. Following the CMFT formalism discussed in the sub-section 2.1.2, the Bose-Hubbard model for a cluster of length $L$ is given by (see Eq. (2.17))

$$\begin{aligned}\hat{H}^C = &- t\sum_{j=1}^{L-1}\left(\hat{a}_{j+1}^\dagger\hat{a}_j + \hat{a}_j^\dagger\hat{a}_{j+1}\right) + \frac{U}{2}\sum_{j=1}^{L}\hat{n}_j(\hat{n}_j-1) - \sum_{j=1}^{L}\mu\hat{n}_j \\ &- t\left((\hat{a}_1^\dagger+\hat{a}_1)\psi - |\psi|^2\right) - t\left((\hat{a}_L^\dagger+\hat{a}_L)\psi - |\psi|^2\right). \qquad (2.32)\end{aligned}$$

The DMRG method for the Bose-Hubbard model (2.1 with $\mu = 0$) works in the canonical ensemble; the number of particles in the system is fixed, $[\hat{H}, \hat{N}] = 0$, hence the superfluid order parameter $\psi = \langle a\rangle = 0$ in all the phases. However, the cluster Hamiltonian (2.32) works in the grand-canonical ensemble and commutation $[\hat{H}^C, \hat{N}] \neq 0$. Consequently, the superfluid parameter $\psi = \langle a\rangle$ is finite to characterize the superfluid phase. In the Mott insulator phase, however, $\psi = 0$. Consequently, the Hamiltonian $\hat{H}^C$ commute with the $\hat{N}$, which implies that the CMFT+DMRG study reproduces earlier DMRG results. Thus, the CMFT+DMRG method interplays between single-site mean-field theory and the DMRG in the one-dimensional Bose-Hubbard model.

The task now is to obtain the ground state energy and the wave function of the Hamiltonian (2.32) for any given length $L$. We use the iteration procedure of DMRG to solve the CMFT Hamiltonian (2.32). We briefly describe these steps below.

**Step I** Consider a superblock configuration consisting of system block $S$ with $l$ sites, environment block $E$ with $l$ sites and two single sites $s$ and $e$ as shown in the Fig. 2.6(a). $l = 1$ in the first iteration and it increases from $l$ to $l+1$ in every iteration. The Hilbert space dimension of the $S$ ($E$) block and the two sites $s, e$ are, say, $M_S$ and $N_s$, respectively. For the first iteration, $l = 1$ and $M_S = N_s$. The superblock has $L = 2l+2$ sites. Let $|\mu_{S(E)}\rangle$ represent the

basis states for the system (environment) block. Similarly $|\sigma_{s(e)}\rangle$ represents the basis states for the single site $s(e)$.

**Step II** The Hamiltonian (2.32) of the superblock

$$\hat{H}_{2l+2} = \hat{H}_S + \hat{H}_s + \hat{H}_e + \hat{H}_E + \hat{H}_{Ss} + \hat{H}_{se} + \hat{H}_{eE} + \hat{H}_1 + \hat{H}_L \tag{2.33}$$

where $\hat{H}_S$ ($\hat{H}_E$) is the system (environment) block Hamiltonian, $\hat{H}_{s(e)}$ is the single site Hamiltonian, $\hat{H}_{Ss}$ is the Hamiltonian connecting the system block $S$ with single site $s$, $\hat{H}_{se}$ is the Hamiltonian connecting the system single site $s$ with single site $e$, and $\hat{H}_{eE}$ is the Hamiltonian connecting the single site $e$ with environment block $E$. $\hat{H}_1$ and $\hat{H}_L$ are the mean-field term in (2.32) i.e., $\hat{H}_1 = -t\left((\hat{a}_1^\dagger + \hat{a}_1)\psi - |\psi|^2\right)$ and $\hat{H}_L = -t\left((\hat{a}_L^\dagger + \hat{a}_L)\psi - |\psi|^2\right)$.

**Step III** Construct the Hamiltonian $\hat{H}_{2l+2}$ for a given initial guess for $\psi$ and diagonalize it to obtain ground state energy $E_{GS}(\psi)$, the wave function

$$|\Psi_{GS}(\psi)\rangle = \sum_{\mu_S,\sigma_s,\sigma_e,\mu_E} C_{\mu_S\sigma_s\sigma_e\mu_E}(\psi)|\mu_S\sigma_s\sigma_e\mu_E\rangle. \tag{2.34}$$

Minimize the ground state energy $E_{GS}(\psi)$ with respect to $\psi$ to obtain global ground state energy $E_{GS}$, the wave function $|\Psi_{GS}\rangle$. At this stage, calculate the expectation values of various operators and the correlation functions on the ground state.

**Step IV** Construct the new system block $S'$ combining the system block $S$ and single site $s$, i.e., $S' = S + s$ as shown in Fig. 2.6(b). Construct the reduced density matrix of $S'$

$$\hat{\rho}_{\mu_S\sigma_s,\mu'_S\sigma'_s} = \sum_{\mu_E\sigma_e} C^*_{\mu_S\sigma_s\sigma_e\mu_E} C_{\mu'_S\sigma'_s\sigma_e\mu_E} \tag{2.35}$$

**Step V** Digonalize $\hat{\rho}_{\mu_S\sigma_s,\mu'_S\sigma'_s}$ to obtain the eigenvalues $\omega_\alpha$ and eigenstates

$$|u_\alpha\rangle = \sum_{\mu_S,\sigma_s} O^\alpha_{\mu_S\sigma_s}|\mu_S\sigma_s\rangle. \tag{2.36}$$

$\omega_\alpha$ measures the weight of the state $|u_\alpha\rangle$ in the ground state $|\Psi_{GS}\rangle$ and satisfy $\sum_\alpha \omega_\alpha = 1$.

**Step VI** New system blocks $S'$ has $M_S \times N_s$ states. We transform the basis states for $S'$ from $|\mu_S\sigma_s\rangle$ to $|u_\alpha\rangle$ keeping $M_S$ eigenstates with the largest $\omega_\alpha$. This way, we have truncated the Hilbert basis of the system block $S'$ from $M_S \times N_s$ to $M_S$. This step is also the most critical step of the CMFT+DMRG method. Hamiltonian $\hat{H}_{S'}$ for the new system block $S'$ and other operators are transformed from the old basis $\{|\mu_S\sigma_s\rangle\}$ to new basis $\{|u_\alpha\rangle\}$

$$\hat{H}^{new}_{S'} = O^\dagger \hat{H}^{old}_{S'} O \tag{2.37}$$

where $O$ is the transformation matrix in Eq. (2.36) and

$$\hat{H}^{old}_{S'} = \hat{H}_S + \hat{H}_s + \hat{H}_{Ss}. \tag{2.38}$$

We don't add $\hat{H}_1$ in the system block Hamiltonian $\hat{H}^{old}_{S'}$. It is included only at the level of constructing the superblock Hamiltonian described in the **Step II**.

**Step VII** Replace system block $S$ with $S'$ and similarly environment block $E$ with $E'$ as shown in Fig. 2.6 and repeat the iteration from **[Step I]**.

#### 2.1.4.2 Bipartite lattice

We now discuss the CMFT+DMRG method applied to a bipartite lattice. The extended Bose-Hubbard model contains nearest-neighbour interaction, which supports density wave and supersolid phases. The lattice can be divided into two sub-lattices, say $A$ and $B$, and one sub-lattice interacts with the other. Applying

the CMFT+DMRG method to the extended Bose-Hubbard model, we find that working with an odd number of sites is preferred over systems with an even number of lattice sites. Since the lattice has left-right symmetry, the density of bosons at the left edge site ($\rho_1$) and the right edge site ($\rho_L$) are equal. This symmetry forces $\rho_{\frac{L}{2}} = \rho_{\frac{L}{2}+1}$ if $L$ is even in all the possible phases, including the density wave phase. Since the density of bosons alternates between the nearest neighbouring sites in the density wave phase, this symmetry forces density variation to have a node at the center, which is not the actual ground state. However, if $L$ is an odd integer, the left-right symmetry is preserved with no such nodes at the center. For this reason, we take Figure 2.7 as the superblock configuration in the CMFT+DMRG formalism and discuss the same using the extended Bose-Hubbard model below.

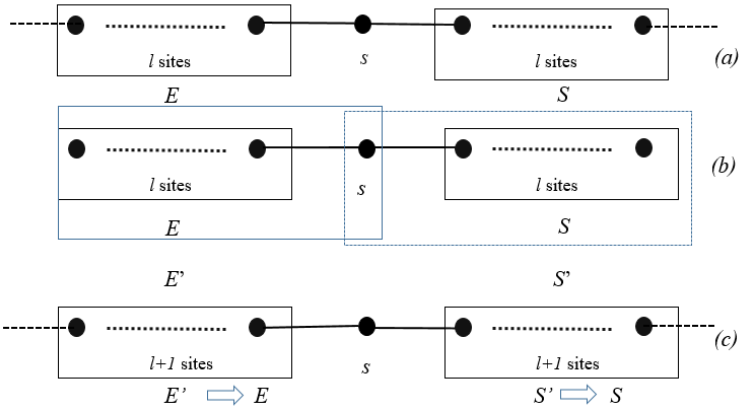


Figure 2.7: Schematic representation of the CMFT+DMRG method for a bipartite lattice. The dotted lines represent the mean-field decoupling, and the solid lines represent the exact hopping in the superblock. (a) represents the superblock constructed from symmetric blocks $S$ and $E$ with the site $s$ in between, (b) the formation of new block $S'$, and (c) a new superblock formed using $S'$ and $E'$.

We first obtain the cluster Hamiltonian for the EBH model

$$\hat{H} = -t\sum_j \left(\hat{a}^\dagger_{j+1}\hat{a}_j + \hat{a}^\dagger_j\hat{a}_{j+1}\right) + \frac{U}{2}\sum_j \hat{n}_j(\hat{n}_j - 1) + V\sum_j \hat{n}_j\hat{n}_{j+1} - \mu\sum_j \hat{n}_j \tag{2.39}$$

the third term is the nearest neighbour interaction with strength $V > 0$. The other terms have the same meaning as in the Eq.(2.1). In the hard-core limit

($U = \infty$) and for $\mu = V$, the model (2.39) maps into spin-1/2 XXZ model, which has a BKT transition from the superfluid phase (equivalent to XY order) to the density wave phase (Ising order) at $V = 2$ [58]. The density of bosons alternates between $\rho_A$ and $\rho_B \neq \rho_A$ in the density wave phase. Here, $\rho_{A(B)}$ represents the density of bosons at $A(B)$ sub-lattices.

We divide the whole lattice into A and B sub-lattices, assuming cluster size $L$ to be an odd integer, and the edge sites are of the same sub-lattice, the resulting Hamiltonians (4.2) is then written as

$$\hat{H} = \sum_p \hat{H}_p^{loc} + \sum_p \hat{H}_p^{hop+V} \tag{2.40}$$

where $p$ represents the cluster index and

$$\begin{aligned}\hat{H}_p^{loc} = &-t\sum_{j=1}^{L-1}\left(\hat{a}_{p,j+1}^\dagger \hat{a}_{p,j} + \hat{a}_{p,j}^\dagger \hat{a}_{p,j+1}\right) + \frac{U}{2}\sum_{j=1}^{L}\hat{n}_{p,j}(\hat{n}_{p,j}-1) - \mu\sum_{j=1}^{L}\hat{n}_{p,j} \\ &+ V\sum_{j=1}^{L-1}\hat{n}_{p,j}\hat{n}_{p,j+1}.\end{aligned} \tag{2.41}$$

Here $\sum_j$ runs over all the sites in cluster $p$, $\hat{a}_{p,j}^\dagger$ ($\hat{a}_{p,j}$) is the boson creation (annihilation) operator for the site $j$ in the cluster $p$ and $\hat{n}_{p,j} = \hat{a}_{p,j}^\dagger \hat{a}_{p,j}$ is the number operator.

The second term in the Hamiltonian Eq. (2.40) represents the hopping of bosons and interactions between the clusters and is given by

$$\begin{aligned}\hat{H}_p^{hop+V} = &-t\left(\hat{a}_{p,1}^\dagger \hat{a}_{p-1,L} + \hat{a}_{p-1,L}^\dagger \hat{a}_{p,1}\right) - t\left(\hat{a}_{p,L}^\dagger \hat{a}_{p+1,1} + \hat{a}_{p+1,1}^\dagger \hat{a}_{p,L}\right) \\ &+ V\left(\hat{n}_{p,1}\hat{n}_{p-1,L}\right) + V\left(\hat{n}_{p,L}\hat{n}_{p+1,L}\right)\end{aligned} \tag{2.42}$$

where the first and third term represent the hopping and interaction between bosons on-site $L$ of cluster $p-1$ and site 1 of cluster $p$, respectively. Similarly, the second and fourth term represent the hopping and interaction between the bosons on-site $L$ of cluster $p$ and site 1 of cluster $p+1$.

Decouple each cluster from its neighbor clusters by using standard mean-field decoupling,

$$\hat{a}_{p,j} = \langle \hat{a}_{p,j} \rangle + \delta\hat{a}_{p,j}$$

and

$$\hat{n}_{p,j} = \langle \hat{n}_{p,j} \rangle + \delta\hat{n}_{p,j}$$

where $\langle \hat{a}_{p,j} \rangle = \psi_{p,j}$ is the superfluid order parameter and $\langle \hat{n}_{p,j} \rangle = \rho_{p,j}$ is the boson density.

Considering the fluctuation $\delta\hat{a}_{p,j}$ and $\delta\hat{n}_{p,j}$ to be small and thus neglecting second-order in fluctuations, we decouple $p$ and $p-1$ clusters

$$\begin{aligned} -t(\hat{a}^\dagger_{p,1}\hat{a}_{p-1,L} + \hat{a}^\dagger_{p-1,L}\hat{a}_{p,1}) + V(\hat{n}_{p,1}\hat{n}_{p-1,L}) \approx & -t\big(\hat{a}^\dagger_{p,1}\psi_{p-1,L} + \hat{a}_{p,1}\psi^*_{p-1,L}\big) \\ & + \frac{t}{2}\left(\psi^*_{p-1,L}\psi_{p,1} + \psi_{p-1,L}\psi^*_{p,1}\right) \\ & + V(\hat{n}_{p,1}\rho_{p-1,L} - \frac{1}{2}\rho_{p,1}\rho_{p-1,L}). \end{aligned} \quad (2.43)$$

The edge sites of cluster $p$, say belong to the $A$ sub-lattice. Since $L$ is odd, the edge sites of clusters $p-1$ and $p+1$ then belong to $B$ sub-lattice. So we replace $\psi_{p-1,L} = \psi_B$, $\psi_{p,1} = \psi_A$, $\rho_{p-1,L} = \rho_B$ and $\rho_{p,1} = \rho_A$, we re-write Eq. (2.43) as

$$\begin{aligned} -t(\hat{a}^\dagger_{p,1}\hat{a}_{p-1,L} + \hat{a}^\dagger_{p-1,L}\hat{a}_{p,1}) + V(\hat{n}_{p,1}\hat{n}_{p-1,L}) \approx & -t\big(\hat{a}^\dagger_{p,1}\psi_B + \hat{a}_{p,1}\psi^*_B\big) \\ & + \frac{t}{2}\left(\psi^*_B\psi_A + \psi_B\psi^*_A\right) \\ & + V(\hat{n}_{p,1}\rho_B - \frac{1}{2}\rho_A\rho_B). \end{aligned} \quad (2.44)$$

Similarly, decoupling $p$ and $p+1$ clusters

$$\begin{aligned} -t(\hat{a}^\dagger_{p,L}\hat{a}_{p+1,1} + \hat{a}^\dagger_{p+1,1}\hat{a}_{p,L}) + V(\hat{n}_{p,L}\hat{n}_{p+1,1}) \approx & -t(\hat{a}^\dagger_{p,L}\psi_B + \hat{a}_{p,L}\psi^*_B) \\ & + \frac{t}{2}\left(\psi^*_A\psi_B + \psi_A\psi^*_B\right) \\ & + V(\hat{n}_{p,L}\rho_B - \frac{1}{2}\rho_A\rho_B) \end{aligned} \quad (2.45)$$

Assuming, without loss of generality, the superfluid order parameter $\psi_{p,j}$ in a given sub-lattice to be real and homogeneous, Eq. (2.40) can be written as

$$\hat{H} = \sum_{p} \hat{H}_p^C \tag{2.46}$$

where $\hat{H}_p^C$ is the Hamiltonian for a cluster of $L$ sites. Dropping the cluster index $p$

$$\begin{aligned}\hat{H}^C = &- t\sum_{j=1}^{L-1}\left(\hat{a}_{j+1}^\dagger \hat{a}_j + \hat{a}_j^\dagger \hat{a}_{j+1}\right) + \frac{U}{2}\sum_{j=1}^{L}\hat{n}_j(\hat{n}_j - 1) + V\sum_{j=1}^{L-1}\hat{n}_j\hat{n}_{j+1} - \sum_{j=1}^{L}\mu\hat{n}_j \\ &- t\left((\hat{a}_1^\dagger + \hat{a}_1)\psi_B - \psi_A\psi_B\right) - t\left((\hat{a}_L^\dagger + \hat{a}_L)\psi_B - \psi_A\psi_B\right) \\ &+ V(\hat{n}_1 + \hat{n}_L)\rho_B - V\rho_A\rho_B. \end{aligned} \tag{2.47}$$

Here, $\psi_A$ ($\psi_B$) and $\rho_A$ ($\rho_B$) are the superfluid order parameter and the density of bosons of A(B) sub-lattices, respectively. The minimization of the ground state energy is done with respect to $\psi_{A(B)}$ and $\rho_{A(B)}$. The phases are characterized based on the values of $\psi_{A(B)}$ and $\rho_{A(B)}$. For example, the superfluid phase has non-zero $\psi_A$ and $\psi_B$, the density wave phase has $\psi_A = \psi_B = 0$ and $\rho_A \neq \rho_B$ with $\rho_A + \rho_B$ is an integer, and supersolid has non-zero $\psi_A$ and $\psi_B$ and $\rho_A \neq \rho_B$.

Next, we describe the steps involved in calculating the ground state energy and the wave function of the Hamiltonian Eq. (2.47) using the CMFT+DMRG method. For odd $L$, the CMFT+DMRG formalism is discussed as follows:

**Step I** Consider a superblock configuration consisting of system block $S$ with $l$ sites, environment block $E$ with $l$ sites and a single site $s$ as shown in the Fig. 2.7(a). $l = 1$ in the first iteration and it increases from $l$ to $l + 1$ in every iteration. The Hilbert space dimension of the $S$ ($E$) block and the site $s$ are, say, $M_S$ and $N_s$, respectively. For the first iteration, $l = 1$ and $M_S = N_s$. The superblock has $L = 2l + 1$ sites. Let $|\mu_{S(E)}\rangle$ represent the basis states for the system (environment) block. Similarly, $|\sigma_s\rangle$ represents

the basis states for the single site $s$.

**Step II** The Hamiltonian (2.47) of the superblock

$$\hat{H}_{2l+1} = \hat{H}_S + \hat{H}_s + \hat{H}_E + \hat{H}_{Ss} + \hat{H}_{sE} + \hat{H}_1 + \hat{H}_L \tag{2.48}$$

where $\hat{H}_S$ ($\hat{H}_E$) is the system (environment) block Hamiltonian, $\hat{H}_s$ is the single site Hamiltonian, $\hat{H}_{Ss}$ is the Hamiltonian connecting the system block $S$ with single site $s$, $\hat{H}_{sE}$ is the Hamiltonian connecting the system single site $s$ with environment block $E$. $\hat{H}_1$ and $\hat{H}_L$ are the mean-field term in (2.47) i.e., $\hat{H}_1 = -t\left((\hat{a}_1^\dagger + \hat{a}_1)\psi_B - \psi_A\psi_B\right) + V\hat{n}_1\rho_B - \frac{V}{2}\rho_A\rho_B$ and $\hat{H}_L = -t\left((\hat{a}_L^\dagger + \hat{a}_L)\psi_B - \psi_A\psi_B\right) + V\hat{n}_L\rho_B - \frac{V}{2}\rho_A\rho_B$.

**Step III** Construct the Hamiltonian $\hat{H}_{2l+1}$ for a given initial guess for $\psi_{A(B)}$ and $\rho_{A(B)}$. Diagonalize it to obtain ground state energy $E_{GS}(\psi_{A(B)}, \rho_{A(B)})$, the wave function

$$|\Psi_{GS}(\psi_{A(B)}, \rho_{A(B)})\rangle = \sum_{\mu_S,\sigma_s,\mu_E} C_{\mu_S\sigma_s\mu_E}(\psi_{A(B)}, \rho_{A(B)})|\mu_S\sigma_s\mu_E\rangle. \tag{2.49}$$

Minimize the ground state energy $E_{GS}(\psi_{A(B)}, \rho_{A(B)})$ with respect to $\psi_A$, $\psi_B$, $\rho_A$ and $\rho_B$ to obtain global ground state energy $E_{GS}$, the wave function $|\Psi_{GS}\rangle$. At this stage, calculate the expectation values of various operators and the correlation functions on the ground state.

**Step IV** Construct the new system block $S'$ combining the system block $S$ and single site $s$, i.e., $S' = S + s$ as shown in Fig. 2.7(b). Similarly, construct the new environment block $E'$ combining the block $E$ and single site $s$, i.e., $E' = E + s$ as shown in Fig. 2.7(b). Construct the reduced density matrices of $S'$ and $E'$

$$\hat{\rho}_{\mu_S\sigma_s,\mu'_S\sigma'_s} = \sum_{\mu_E} C^*_{\mu_S\sigma_s\mu_E} C_{\mu'_S\sigma'_s\mu_E} \tag{2.50}$$

$$\hat{\rho}_{\mu_E\sigma_s,\mu'_E\sigma'_s} = \sum_{\mu_S} C^*_{\mu_S\sigma_s\mu_E} C_{\mu_S\sigma'_s\mu'_E}. \tag{2.51}$$

**Step V** Digonalize $\hat{\rho}_{\mu_S\sigma_s,\mu'_S\sigma'_s}$ to obtain the eigenvalues $\omega_\alpha$ and eigenstates

$$|u_\alpha\rangle = \sum_{\mu_S,\sigma_s} O^\alpha_{\mu_S\sigma_s}|\mu_S\sigma_s\rangle. \tag{2.52}$$

$\omega_\alpha$ measures the weight of the state $|u_\alpha\rangle$ in the ground state $|\Psi_{GS}\rangle$ and satisfy $\sum_\alpha \omega_\alpha = 1$. Similarly, diagonalize $\hat{\rho}_{\mu_E\sigma_s,\mu'_E\sigma'_s}$.

**Step VI** New system blocks $S'$ has $M_S \times N_s$ states. We transform the basis states for $S'$ from $|\mu_S\sigma_s\rangle$ to $|u_\alpha\rangle$ keeping $M_S$ eigenstates with the largest $\omega_\alpha$. This way, we have truncated the Hilbert basis of the system block $S'$ from $M_S \times N_s$ to $M_S$. This step is also the most critical step of the CMFT+DMRG method. Hamiltonian $\hat{H}_{S'}$ for the new system block $S'$ and other operators are transformed from the old basis $\{|\mu_S\sigma_s\rangle\}$ to new basis $\{|u_\alpha\rangle\}$

$$\hat{H}^{new}_{S'} = O^\dagger \hat{H}^{old}_{S'} O \tag{2.53}$$

where $O$ is the transformation matrix in Eq. (2.52) and

$$\hat{H}^{old}_{S'} = \hat{H}_S + \hat{H}_s + \hat{H}_{Ss}. \tag{2.54}$$

We don't add $\hat{H}_1$ in the system block Hamiltonian $\hat{H}^{old}_{S'}$. It is included only at the level of constructing the superblock Hamiltonian described in the **Step II**.

**Step VII** Replace system block $S$ with $S'$ and similarly environment block $E$ with $E'$ as shown in Fig. 2.7 and repeat from **[Step I]**.

### 2.1.5 Conclusions

In this chapter, we have discussed the formalism of single-site MFT, CMFT, infinite-size DMRG, and CMFT+DMRG. The mean-field theory gives an oversimplified description of the SF and MI phases in the BH model with the overestima-

tion of the critical parameters. The CMFT method improves the single-site MFT results with increasing cluster sites at the cost of increased computational power due to an exponential increase in the dimension of the cluster Hamiltonian. The DMRG method, thus, proves more valuable in the study of ground state properties of large systems using density matrix states as the dominant state in the ground state of large systems. It captures the phase more accurately than MFT and CMFT in the BH model. Still, it fails to directly probe into BH models with exotic gapless phases like supersolid and polar superfluid. The CMFT+DMRG is thus proposed to utilize the advantages of CMFT and DMRG to effectively identify the exotic gapless phases. In subsequent chapters, we apply the CMFT+DMRG method to the Bose-Hubbard model and the extended Bose-Hubbard model to demonstrate the usefulness of this approach.

CHAPTER 3

# Bose Hubbard Model

## 3.1 Introduction

Cold bosonic atoms in an optical lattice in the tight-binding regime are described by the Bose Hubbard model [17] defined by

$$\hat{H} = -t \sum_j \left( \hat{a}_j^\dagger \hat{a}_{j+1} + \hat{a}_{j+1}^\dagger \hat{a}_j \right) + \frac{U}{2} \sum_j \hat{n}_j (\hat{n}_j - 1) - \mu \sum_j \hat{n}_j. \tag{3.1}$$

Here, $\hat{a}_i^\dagger$ ($\hat{a}_i$) are boson creation (annihilation) operators, and the first term represents the hopping of bosons between nearest neighbouring sites with amplitude $t > 0$. The second term is the on-site interaction between the bosons, which increases the system's energy by $U$ whenever there is more than one boson per site. The last term controls the boson number for a given chemical potential $\mu$. The ratio between $U/\rho t$, where $\rho$ is the density of bosons (the number of bosons per site), controls the ground state of the BH model. When the $t$ dominates $U$, $U/\rho t \lesssim 1$, the system goes into the superfluid phase characterized by coherent wave properties and off-diagonal long-range ordering. In this phase, the bosons are delocalized on the lattice and have a gapless excitation spectrum. On the other hand, when $U$ dominates, and at integer filling, quantum fluctuations drive the system in a gapped, localized Mott insulator phase characterized by the absence of off-diagonal long-range ordering.

The one-dimensional Bose-Hubbard model is well-studied; the phases and the

phase boundaries between the superfluid to Mott insulator phases are known to a good approximation using various approximate and numerical techniques, critical value best approximated to $U_c/t \approx 3.28$ [35], [36] for the density $\rho = 1$ MI to SF phase, making it a suitable candidate to test the CMFT+DMRG method proposed in the previous chapter. The main aim of this chapter is to demonstrate the CMFT+DMRG method applied to the Bose Hubbard Model and compare it with the DMRG method to address its advantages and limitations. We also address the Bose-Hubbard model with $t < 0$ to demonstrate the existence of a staggered superfluid, which can be captured easily within the CMFT+DMRG method.

This chapter is organized as follows. In Section 3.2, we analyze the convergence of superfluid order parameters against the system size $L$. The comparison of the CMFT+DMRG results with the DMRG results is given in Section 2.1.3. We also demonstrate the application of the CMFT+DMRG method to the Bose-Hubbard model with $t < 0$ in Section 3.4 and conclude this chapter in Section 3.5.

## 3.2 Convergence of superfluid order parameter

We perform the CMFT+DMRG calculations following the iteration procedure described in the section 2.1.4.1. We retain up to $M_S = 75$ eigenstates in the left/right block-reduced density matrix. This results a truncation error $\epsilon = 1 - \sum_{\alpha=1}^{M_S} \omega_\alpha$ of the order of $10^{-8}$. We keep up to $N_s = 5$ states per site, resulting in the maximum number of bosons per site $n_{max} = 4$. We found $n_{max} = 4$ is sufficient since we restrict the density of bosons $\rho < 2$. We set the energy scale by $t = 1$. The length of the system increases from $L$ to $L + 2$ in each CMFT+DMRG iteration. Since the ground state energy $E_{GS}(L, \psi)$ is a function of the superfluid parameter $\psi$, we calculate it self-consistently for every length $L$. We use the self-consistent value of the $\psi$ to calculate the ground state energy and eigenfunction. We calculate the expectation values of various operators and the correlation functions using this ground-state eigenfunction.

The CMFT+DMRG is an iterative procedure. We analyze, first, the convergence of the superfluid order parameters $\psi_j$ and density of the bosons $\rho_j$ as a function of lattice position $j$ for a given system size $L$. We follow it with an analysis of the convergence as a function of system size $L$.

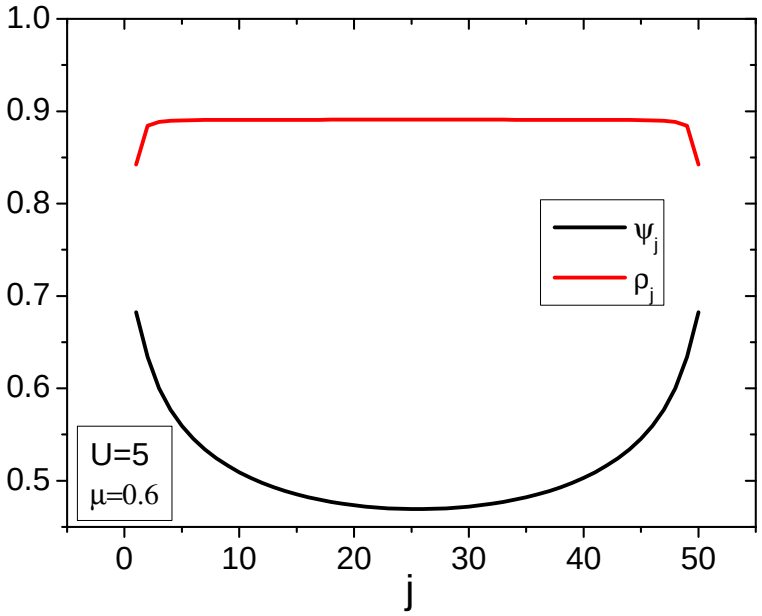


Figure 3.1: Superfluid order parameter $\psi_j$ and boson density $\rho_j$ are plotted as a function of position $j$. Here we have considered a lattice with length $L = 50$ and model parameters $U = 5$ and $\mu = 0.6$.

For $U = 5$, and $\mu = 0.6$, we plot $\psi_j$ and $\rho_j$ as a function of lattice position $j$ for a system length with $L = 50$ in Fig. 3.1. This figure depicts a typical behavior of $\psi_j$ and $\rho_j$. The edge sites have higher superfluid order parameter values compared to the center. $\psi_j$ decreases as the lattice position $j$ moves away from the edges and has the least value when $j = L/2$. Similarly, density $\rho_j$ increases from the edges to the center. The variation of $\psi_j$ with $j$ is easy to understand. The mean-field approximation affects the edge sites, and as the lattice position moves away from the edges, the effect of the approximation tampers off. The mean-field approximation is known to overestimate the superfluid phase. Hence, the superfluid order parameter values are larger at the edges than at the center. For a given system with length $L$, the $\psi_{L/2}$ is the least. To understand the converges of the superfluid order parameters with system length $L$, we plot $\psi_j$ (where $j = 1$ to

$L/2$) for different lengths; $L = 100,\ 300,\ 700,$ and, $1000$ in Fig. 3.2. The superfluid order parameters converge from the edges as the system length $L$ increases. For $L = 100$, $\psi_j$ have been converged for all $j$ except near the center of the lattice $j \sim 50$. As length increases, $\psi_j$ converges for more range of values of $j$, and eventually, for larger $L$, $\psi_j$ converges for the entire system. Similar behavior is seen for the boson density $\rho_j$ in Fig. 3.3 plotted as function of $j$ for different lengths; $L = 100,\ 300,\ 700,$ and, $1000$. The $\rho$ converges faster with $L$ compared to $\psi$.

To demonstrate the convergence the superfluid order parameters further, we plot $\psi_1$, $\psi_{L/2}$, $\rho_1$ and $\rho_{L/2}$ for system sizes up to $L = 1000$. Here again, we keep $U = 5.0$ and $\mu = 0.6$. In Fig. 3.4, the densities, $\rho_1$ and $\rho_{L/2}$, and the superfluid parameter for the edge site $\psi_1$ converge faster with $L$ compare to $\psi_{L/2}$. $\psi_{L/2}$ converges eventually as length increases. Both $\psi_1$ and $\psi_{L/2}$ converge to a finite superfluid order parameter, and we find $\psi_1 > \psi_{L/2}$ due to the edge effect: the mean-field approximation overestimates superfluid order parameter. For $\mu = 1.4$, however, in Fig. 3.5, $\psi_1$, $\psi_{L/2}$, $\rho_1$ and $\rho_{L/2}$ converges at approximately same rate and $\psi_{L/2}$ converges to zero yielding a Mott insulator phase. It may be noted that, as a consequence of mean-field decoupling of the edge sites, the superfluid order parameter at the edge site, $\psi_1$, is finite for both cases, i.e., $\mu = 0.6$ and $1.4$. However, $\psi_{L/2}$ is finite in the former case and zero in the later. From the above behavior of convergence of superfluid order parameters and densities, we conclude that $\psi_{L/2}$ and $\rho_{L/2}$ represent the converged values for the superfluid fluid order parameter and density of the system with length $L$. We denote these by $\psi$ and $\rho$, respectively.

## 3.3 Comparison of CMFT+DMRG with DMRG

This Section compares the CMFT+DMRG result with the standard DMRG, keeping the on-site interaction $U = 5$. The ground state energy $E_L(N)$ of the system of length $L$ having $N$ bosons is obtained using finite-size DMRG pro-

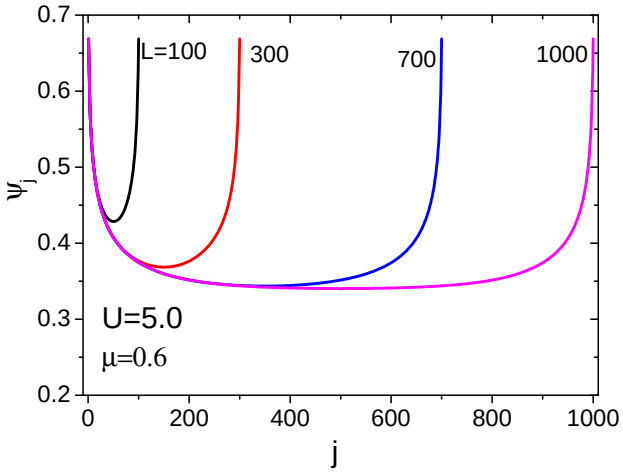


Figure 3.2: The superfluid order parameter $\psi_j$ are plotted as a function of position $j$ for different lengths $L$. Here $U = 5$ and $\mu = 0.6$.

cedure [59]. The density of the system $\rho_L = N/L$ and the chemical potential corresponding to this density is determined using the relation.

$$\mu = (\mu^+ + \mu^-)/2, \tag{3.2}$$

where $\mu^+ = E_L(N+1) - E_L(N)$ and $\mu^- = E_L(N) - E_L(N-1)$. The DMRG method characterizes different phases from the single-particle energy gap $\Delta = \mu^+ - \mu_-$, the boson density $\rho$ and compressibility $\kappa = \frac{\partial \rho}{\partial \mu}$. In the superfluid phase, $\kappa$ is finite, $\Delta = 0$; in the Mott insulator phase, $\rho$ is commensurate, and $\kappa$ is equal to zero, and the gap $\Delta$ is finite. To compare the CMFT+DMRG and DMRG, we use the density $\rho$ variation with the chemical potential $\mu$. We plot, in Fig. 3.6, the calculated density using the DMRG method (for $L = 300$) and the CMFT+DMRG method (for $L = 200$) for different chemical potentials. We observe that the density obtained from both methods agrees, though the length chosen for CMFT+DMRG is smaller than that for DMRG. Density increases with chemical potential and remains pinned at $\rho = 1$ for a range of $\mu$ values. This region corresponding to the Mott insulator phase has finite gap $\Delta = \mu^+ - \mu^-$ and vanishing compressibility $\kappa = \left(\frac{d\rho}{d\mu}\right)$. The region outside $\rho = 1$ has finite compressibility and is considered a superfluid phase. The DMRG method correctly

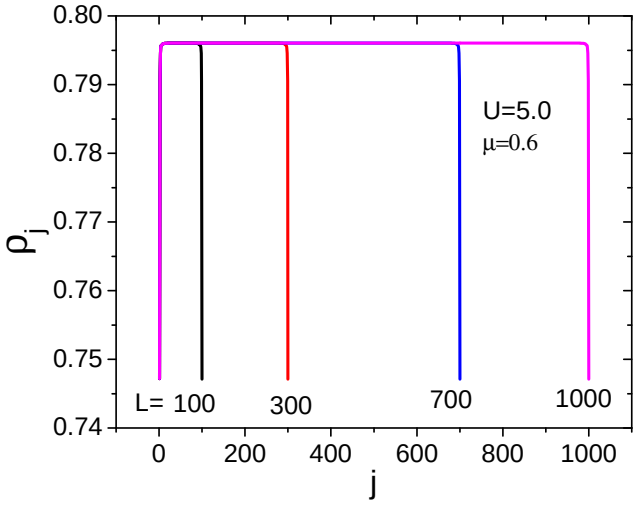


Figure 3.3: The boson density $\rho_j$ are plotted as a function of position $j$ for different lengths $L$. Here parameters $U = 5$ and $\mu = 0.6$ are same as that in Fig 3.2.

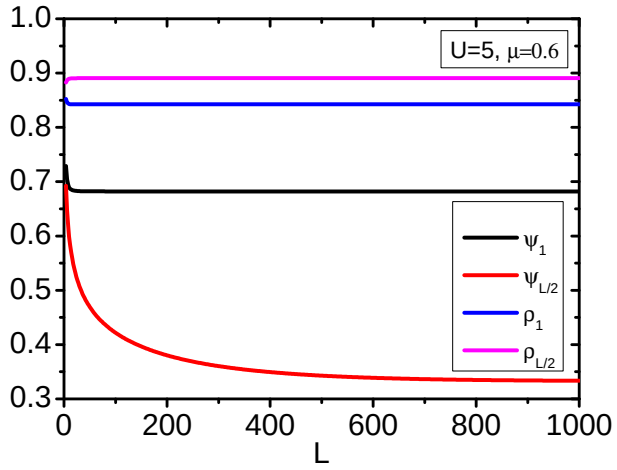


Figure 3.4: The superfluid order parameters $\psi(1)$, $\psi(L/2)$ and the boson densities $\rho(1)$ and $\rho(L/2)$ are plotted as a function length $L$ for $U = 5$ and $\mu = 0.6$.

demonstrates the phases in the BH model. However, the DMRG calculations cannot directly access superfluid order parameters to identify SF and MI phases. In the same figure, we plot the superfluid order parameter obtained from the CMFT+DMRG method (for $L = 200$ and 500). We observe that $\psi$ vanishes in the Mott insulator phase as it should and is finite in the superfluid phase. Thus, it demonstrates direct access to the different phases in the CMFT+DMRG method.

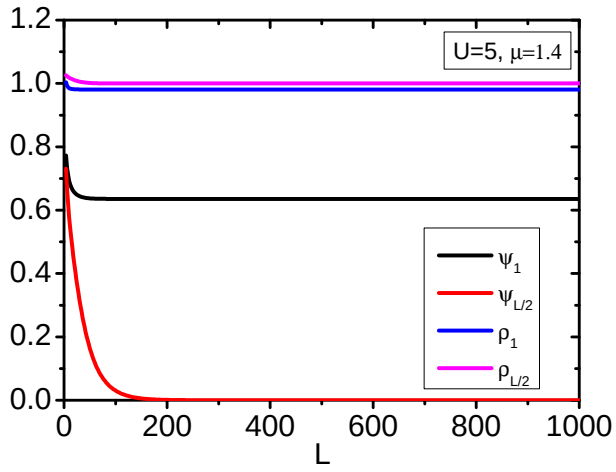


Figure 3.5: The superfluid order parameters $\psi(1)$, $\psi(L/2)$ and the boson densities $\rho(1)$ and $\rho(L/2)$ are plotted as a function length $L$ for $U = 5$ and $\mu = 1.4$.

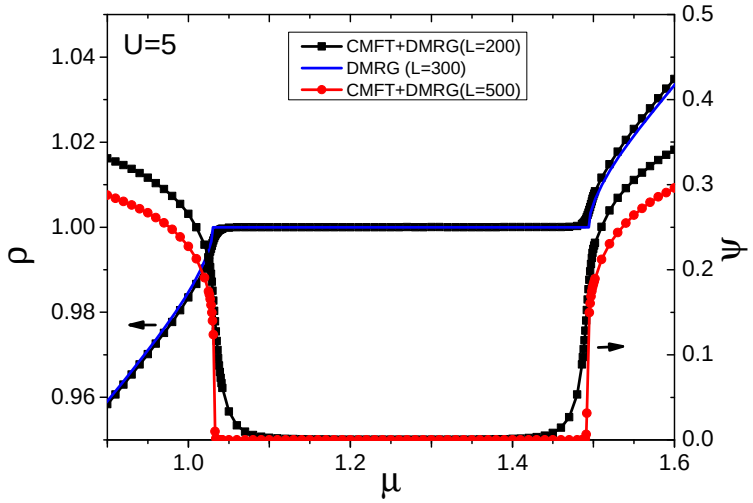


Figure 3.6: Density $\rho$ from DMRG (blue line) and CMFT+DMRG (black line with bullet) methods and $\psi$ from the CMFT+DMRG method for two different lengths.

We now address the convergence of the superfluid order parameter $\psi$ and density $\rho$ to the system length $L$. The convergence of $\psi$ and $\rho$ depends on (i) the value of the on-site interaction $U$ compared to $U_C$ and (ii) the value of chemical potential $\mu$ compared to $\mu^{-/+}$. Here $U_C$ is the critical on-site interaction for SF-MI transition for $\rho = 1$ and $\mu^-(U)$ and $\mu^+(U)$ are the lower and upper edge of the Mott lobe for a given $U$. If $U >> U_C$ and $|\mu - \mu^{-/+}(U)| >> 0$, that is, deep in the SF or MI phase, the SF order parameter and density convergence

rapidly with $L$. However, in the opposite limit, as we approach the critical $U_C$ or phase boundary, i.e., $U \sim U_C$ and $|\mu - \mu^{-/+}(U)| \sim 0$, the convergence is very slow. In these limits, the correlation length $\xi$ is large, and the convergence of the superfluid order parameter is guaranteed if and only if $L >> \xi$. To demonstrate this behavior, we plot $\psi_L$ and $\rho_L$ obtained from CMFT+DMRG for $U = 5$ and $U = 4$ in Figs. 3.7 and Fig 3.8, respectively. It may be noted that the best estimate of $U_C \sim 3.28$ [35], [36]. From Fig. 3.7, we observe that, for $U = 5$, length $L = 500$ is sufficient for converging the SF order parameter. However, as we decrease the on-site interaction, say $U = 4$, as in Fig. 3.8, the convergence is slow and requires a larger length.

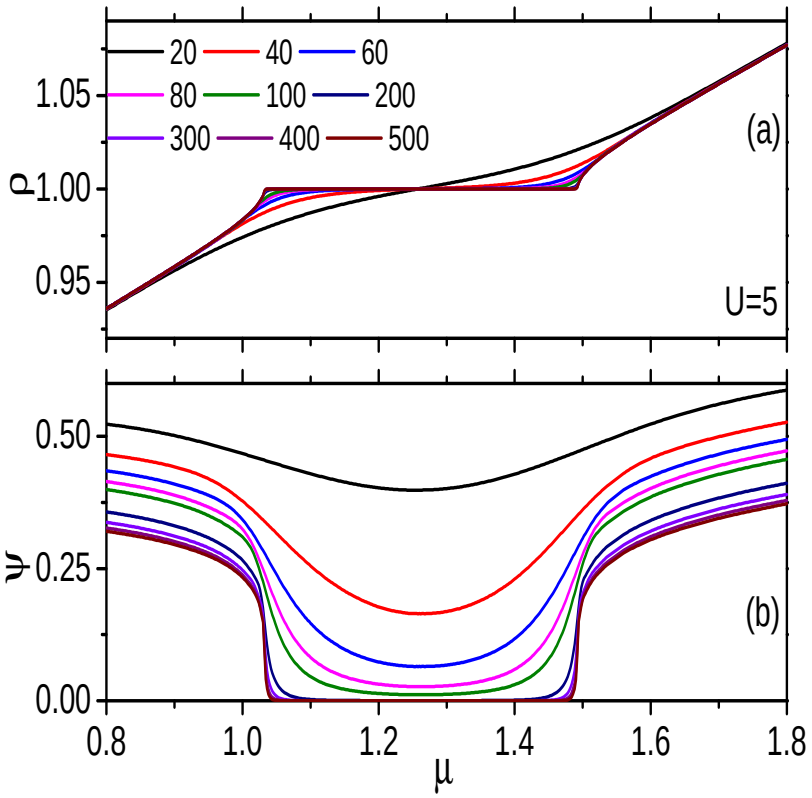


Figure 3.7: (a) $\rho$ and (b) $\psi$ for different lengths for on-site interaction $U = 5$.

The CMFT+DMRG method, like the DMRG method, also allows us to calcu-

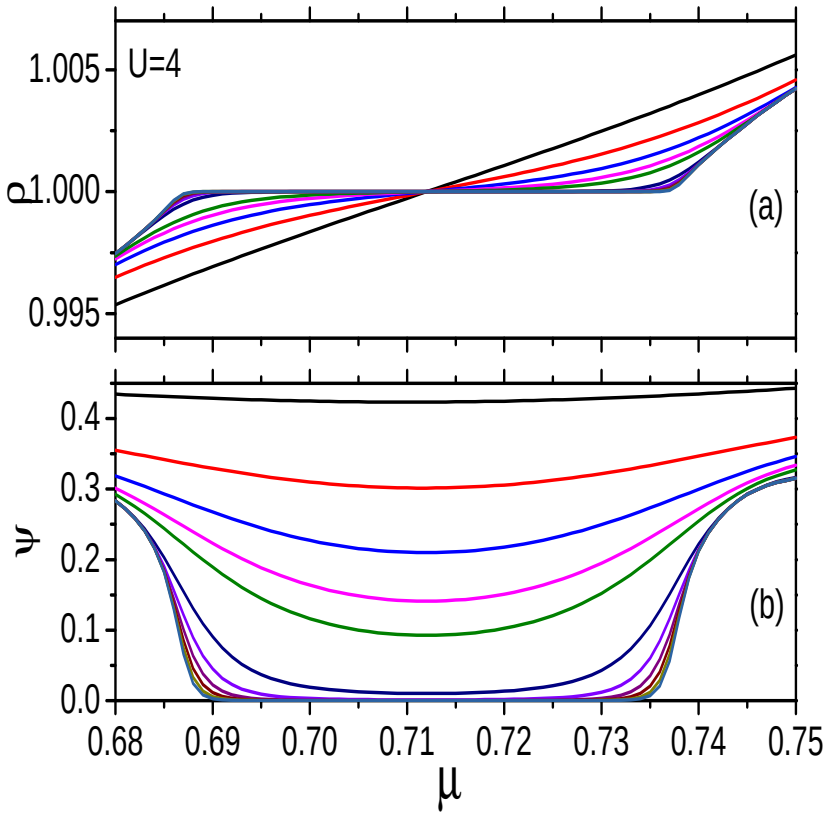


Figure 3.8: (a) $\rho$ and (b) $\psi$ for different lengths $L = 100,\ 200,\ \cdots,\ 3700$ for on-site interaction $U = 4$.

late the phase coherence correlation function

$$\Gamma(|(j - j')|) = \frac{1}{2}(\langle \hat{a}_j^\dagger \hat{a}_{j'} + H.c.\rangle). \tag{3.3}$$

Here, the brackets $\langle \cdots \rangle$ denote the mean value of an observable in the system $|\psi_{GS}\rangle$. We plot $\Gamma(r = |\ (j - j')\ |)$ for the SF and the MI phases in Fig 3.9. We consider on-site interaction $U = 5$, length $L = 1000$ and restrict $350 \leq j, j' \leq 650$ so that the $j, j'$ are far from the system edges to avoid the mean-field fluctuations and convergence of the SF order parameter in this region. In Fig 3.9(a), for $\mu = 0.5$, $\Gamma(r) \to \psi^2$ as $r \to \infty$, a powerlaw decay, analogous to the Berenzinski-Kosterlitz-Thouless transition is observed in the superfluid phase. And for $\mu = 1.25$, $\Gamma(r)$ decay exponentially with $r$ as in the Mott insulator phase.

The Fourier transform of the phase coherence correlation function

$$n(k) = \frac{1}{L^2} \sum_{j,j'} \Gamma(|j - j'|) e^{-\imath k|j-j'|} \tag{3.4}$$

gives the number of system particles with a wave vector $k$. $n(0)$ is the condensate fraction, giving the fraction of bosons occupying the superfluid ground state. We plot $n(0)$ and the superfluid density $\rho_S = \psi^2$ as a function of $\mu$ across SF-MI phase transition for $U = 5$ in Fig 3.9(b). In the Mott insulator phase, $\rho_S$ is equal to zero, and the $n(0)$ is small but finite as a small number of bosons occupy $k = 0$ state even in the MI phase. As $\rho_S$ becomes finite, more bosons occupy the $k = 0$ state, and the condensate fraction increases sharply in the superfluid phase.

Finally, we compare the phase diagram obtained using the CMFT+DMRG and the DMRG [59] in Fig. 3.10. The phase diagram in the region $U >> U_C$ agrees with each DMRG result. As $U$ approaches $U_C$, the Mott gap is tiny and scales with logarithmic correction [36]. Hence, the CMFT+DMRG method could not resolve the Mott phase from the superfluid order parameter for $U < 3.8$.

The SF-MI transition at fixed integer density belongs to Berezinskii–Kosterlitz–Thouless transition (BKT transition) [58]. The order parameter shows a discontinuity at the BKT transition. Applying the CMFT+DMRG method to observe the discontinuity at the SF-MI transition is interesting. However, we were not successful in observing this discontinuity due to (i) the lack of known accurate relation between $\mu$ and $U$ to fix density $\rho = 1$ and (ii) the need to keep a more significant number of states in the DMRG procedure when $U$ is closed to $U_C$. We could, however, observe such discontinuity across the superfluid to density wave transition in the extended Bose-Hubbard model discussed in the next chapter.

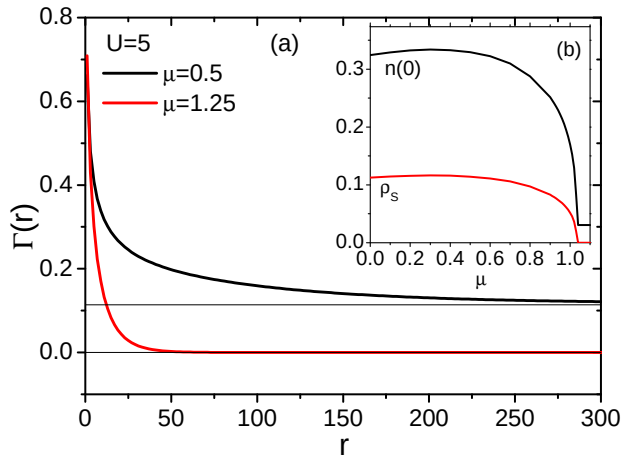


Figure 3.9: (a) Decay of phase coherence correlation function $\Gamma(r)$ with respect to $r$. $\Gamma(r) \to \psi^2$ as $r \to \infty$. (b) Variation of the condensate fraction $n(0)$ and the superfluid density $\rho_S$ across SF-MI transition.

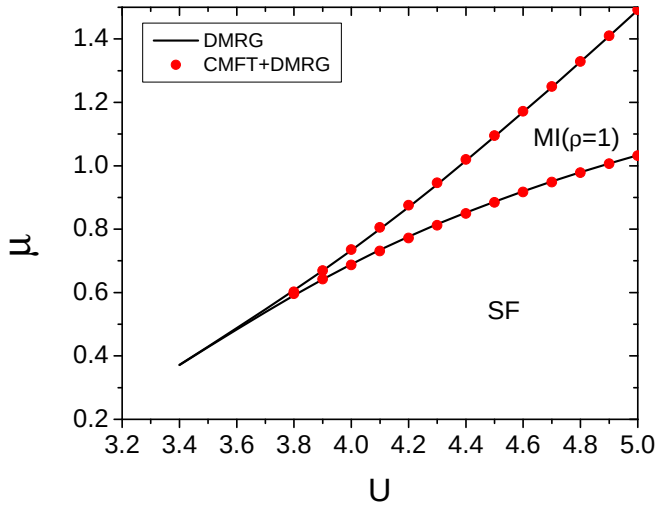


Figure 3.10: $\mu - U$ phase diagram of Bose Hubbard model close to density $\rho = 1$ using the DMRG (black line)) and CMFT+DMRG (red dot) method.

## 3.4 Staggered Superfluid Phase in Bose-Hubbard model

Manipulating the bosons in the optical lattice with either additional interactions or changing the sign of hopping amplitude may result in novel quantum phases [60], [61]. It is natural to investigate whether such models can be treated

in the CMFT+DMRG method to unravel new phases. The extended Bose Hubbard model, the Bose Hubbard model with nearest neighbour interaction, exhibits phases like a density-wave insulator, supersolid, Haldane insulators, and phase-separated superfluid beside superfluid and Mott insulators. We will be discussing the results of the extended Bose Hubbard model in the next chapter. In this Section, we focus our investigation on the Bose-Hubbard model with negative hopping amplitude. The sign of the hopping amplitude in an optical lattice can be changed by time-dependent shaking of the lattice [62], [63], or populating higher bands [64].

The Bose-Hubbard model with hopping amplitude $t$ is given by

$$\hat{H} = -t \sum_j \left( \hat{a}_j^\dagger \hat{a}_{j+1} + \hat{a}_{j+1}^\dagger \hat{a}_j \right) + \frac{U}{2} \sum_j \hat{n}_j (\hat{n}_j - 1) - \mu \sum_j \hat{n}_j. \tag{3.5}$$

Setting $U = 0$ and Fourier transforming Eq. (3.5),

$$\hat{H} = \sum_k (\epsilon_k - \mu) \hat{a}_k^\dagger \hat{a}_k \tag{3.6}$$

where the single-particle dispersion energy with the wave number $k$ is $\epsilon_k = -2t\cos(k)$. For $t > 0$, we get the standard Bose-Hubbard model. The dispersion energy $\epsilon_k$ has a minima at $k = 0$ and corresponds to bosons condensate with $k = 0$ state. We discussed the Bose-Hubbard model with positive hopping amplitude in Section 2.1.3.

However, for $t < 0$, the minima of the $\epsilon_k$ is at $k = \pm\pi$. The bosons condensate at $k = \pm\pi$ state and is known as $\pi$ superfluid ($\pi$-SF) phase. In the conventional BH model ($t > 0$), as we have seen in section 2.1.3, $\psi$ has translational symmetry, and the effect of the phase is nullified. However, for the $t < 0$ case, as shown below, $\pi$-SF is characterized by the staggering in the superfluid order parameter.

Setting $t = -|t|$ in Eq. (3.5) we get

$$\hat{H} = |t| \sum_j \left( \hat{a}_j^\dagger \hat{a}_{j+1} + \hat{a}_{j+1}^\dagger \hat{a}_j \right) + \frac{U}{2} \sum_j \hat{n}_j (\hat{n}_j - 1) - \mu \sum_j \hat{n}_j. \tag{3.7}$$

Transforming $\hat{a}_j^\dagger = (-1)^j \hat{b}_j^\dagger$, Eq. (3.7) maps into

$$\hat{H} = -|t| \sum_j \left( \hat{b}_j^\dagger \hat{b}_{j+1} + \hat{b}_{j+1}^\dagger \hat{b}_j \right) + \frac{U}{2} \sum_j \hat{n}_j (\hat{n}_j - 1) - \mu \sum_j \hat{n}_j. \tag{3.8}$$

Here $\hat{n}_j = \hat{a}_j^\dagger \hat{a}_j = \hat{b}_j^\dagger \hat{b}_j$, Eq. (3.6) is same as Eq. (3.1) studied in the previous Section and the superfluid phase is uniform $\langle \hat{b}_j \rangle$ across the lattice position. Therefore the superfluid order parameter in Eq. (3.7) $\langle \hat{a}_j \rangle = (-1)^j \langle \hat{b}_j \rangle$, alternate between positive and negative values.

We deploy the CMFT+DMRG method to understand the $\pi - SF$ phase in the BH model (3.5) with $t < 0$. We set $t = -1$, $U = 5$ and calculate superfluid order parameters $\psi_j$ and density $\rho_j$ for various chemical potential values. We plot, in Fig. 3.11, the position dependent superfluid order parameter $\psi_j$ for $\mu = 0.5$ and keeping $L = 1001$. Since the superfluid order parameters are staggered, working with odd lengths is preferred, as discussed in Sec. 2.1.4.2. The superfluid order parameter is converged to a value $|\psi| = 0.3179$ and finds $\psi_j = (-1)^j |\psi|$ demonstrating the staggered nature of the superfluid order parameter; characteristics of the $\pi$-SF phase. The density $\rho_j$, however, remains uniform across the lattice.

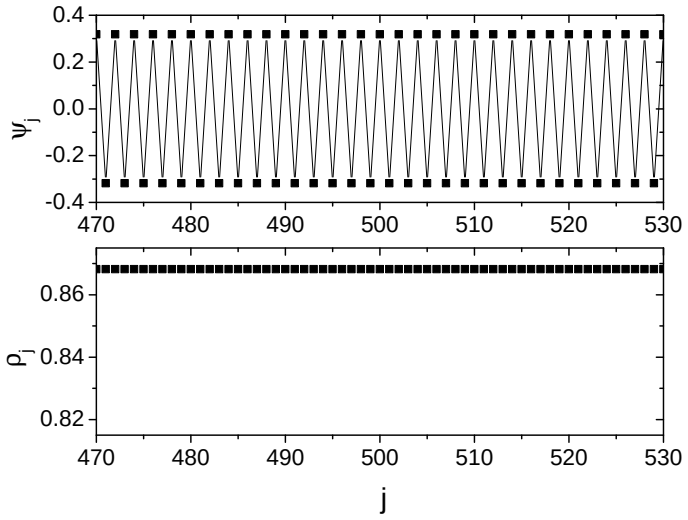


Figure 3.11: The superfluid order parameter $\psi_j$ (top panel) and density $\rho_j$ (bottom panel) are plotted as a function of position $470 < j < 530$ for length $L = 1001$. Here $t = -1$, $U = 5$, and $\mu = 0.5$.

We plot $\psi_A = \psi_{\frac{L-1}{2}}$ and $\psi_B = \psi_{\frac{L+1}{2}}$, two central adjacent sites for a system with $L = 1001$, for different values of chemical potential $\mu$ in Fig.3.12. We find, as expected, $\psi_A = -\psi_B$ for all the $\mu$ values and vanishes in the Mott insulator phase.

We compare the Bose Hubbard model with hopping amplitude $t > 0$ and $t < 0$. In the former case, we have a normal superfluid, while the latter is $\pi$-SF. We define an order parameter $\Delta_{\pi-\mathrm{SF}} = \frac{1}{2}(\psi_{L/2} - \psi_{L/2\pm1})$ to distinguish the $\pi$-SF from the normal SF. Since $\psi_j = |\psi|$ is uniform for normal SF phase, $\Delta_{\pi-\mathrm{SF}} = 0$ and $\psi_j = (-1)^j|\psi|$ in the $\pi$-SF, $\Delta_{\pi-\mathrm{SF}} = |\psi|$ remain finite. Comparing $\pi$-SF with normal SF phase for the same on-site interaction $U$, we find superfluid density and density remain the same in both cases. The only difference is the staggered superfluid order parameter in the case of $\pi$-SF. These observations are plotted in the Figs. 3.13 and 3.14. The phase diagram of the Bose-Hubbard model with $t = \pm1$ remains the same except for the nature of the superfluid phase. The former has a homogeneous superfluid, while the latter superfluid is staggered.

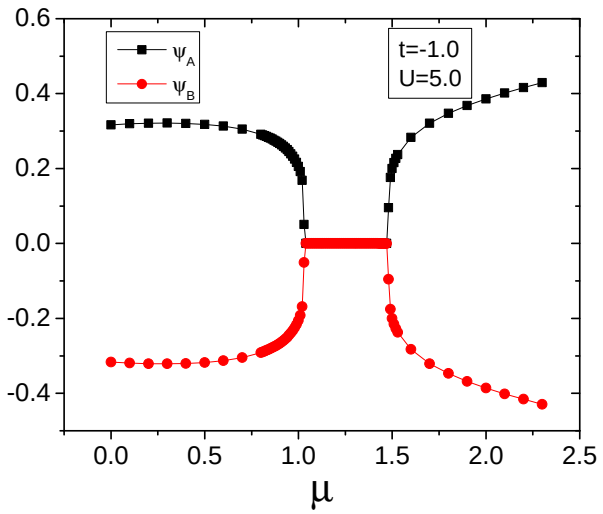


Figure 3.12: Superfluid order parameters $\psi_A = \psi_{\frac{L-1}{2}}$ and $\psi_B = \psi_{\frac{L+1}{2}}$ versus $\mu$ for $t = -1$ and $U = 5.0$.

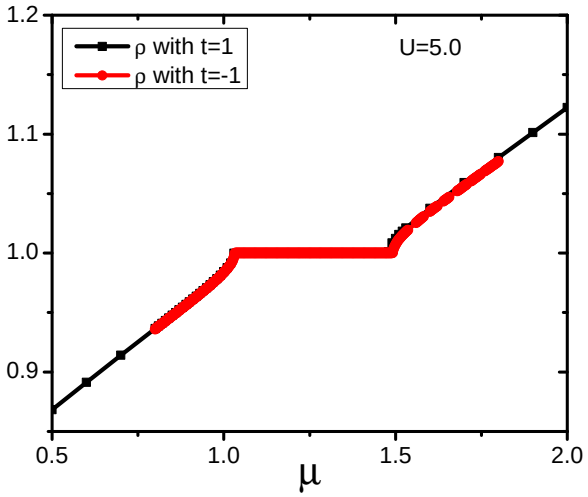


Figure 3.13: The boson densities for $t = 1$ and $t = -1$ are plotted as function of $\mu$ for $U = 5.0$.

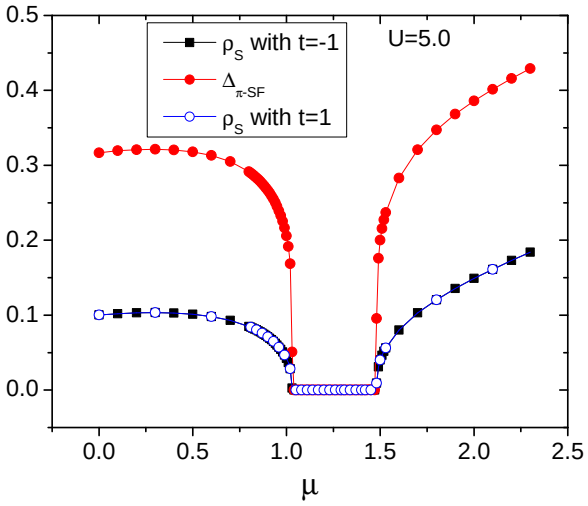


Figure 3.14: The superfluid density $\rho_S$ for $t = \pm 1$ and $\Delta_{\pi-\mathrm{SF}}$ is plotted as function of $\mu$ for $U = 5.0$. The finite $\Delta_{\pi-\mathrm{SF}}$ marks the $\pi$-SF phase.

## 3.5 Conclusions

We have developed the CMFT+DMRG method, integrating the key features of the mean-field theory and the DMRG methods to understand quantum phases in the one-dimensional Bose Hubbard models. The CMFT+DMRG method overcomes many limitations of the mean-field theory and the DMRG technique. The

small system size in the former and the direct calculation of superfluid order parameters in the latter are notable. We apply the CMFT+DMRG method to the Bose-Hubbard model. The Bose-Hubbard model ($t > 0$) has two phases: superfluid and Mott insulator. We identify these phases with the superfluid order parameters and the condensate fraction. Our results agree with the earlier studies done using the DMRG method.

We further extend our studies to $t < 0$ case where we observe the $\pi$-SF phase and the staggering in the superfluid order parameter. This method can be extended to other models, such as the soft-core extended Bose-Hubbard model, spin-1 Bose-Hubbard model, etc., to understand the exotic superfluid phases such as supersolids, polar/Ferro superfluids, and pair superfluids. The DMRG and the CMFT+DMRG methods work in complementary ways to understand the entire phase diagram of the Bose-Hubbard models. The former method works in the canonical ensemble and is most suitable for characterizing the gaped phases. The CMFT+DMRG, however, works in the grand-canonical ensemble and is very useful in understanding the gapless quantum phases.

CHAPTER 4

# Extended Bose-Hubbard Model

## 4.1 Introduction

For several decades, experiments with trapped ultra-cold quantum gases have contributed to our understanding of the behavior of quantum matter. They have proven to be excellent environments for studying strongly coupled quantum systems due to the remarkable flexibility in tuning the Hamiltonian. An example is the realization of the Bose-Hubbard (BH) model in the weakly interacting Bose gas where only s-wave scattering is relevant, and approximating the the inter-atomic potential is to good accuracy with the isotropic contact potential. The strength of the potential and the polarity depends on the $s$-wave scattering length, which can be manipulated using the Feshbach resonances [18]–[20]. As discussed in the previous chapter, the Bose-Hubbard model comprises the nearest neighbour hopping with the hopping amplitude $t$ and the on-site interaction with the strength $U$, crucial in driving the quantum phase transitions in the ground state from a coherent superfluid to a Mott insulator phase at integer densities. These phase transitions can be controlled using laser frequencies and intensities and are widely studied using theoretical techniques and verified experimentally. The remarkable flexibility in manipulating systems has led to the quest to realize quantum systems with richer interactions in strongly correlated quantum systems and to understand

the plethora of exotic phases predicted in these systems.

The supersolid (SS) phase is an example of an exotic phase exhibiting crystalline order of solid and finite superfluidity. In this phase, two continuous symmetries, U(1) and translational symmetry, are broken simultaneously. After Penrose and Onsager proposed the SS phase [65], the quest for realizing it theoretically and experimentally began to attract lots of interest [66]. The SS phase was predicted in solid $^4$He [67], yet there is yet to be a consensus on its presence [68], [69] due to heavy reliance on factors such as impurities and disorders. Kim and Chan reported its presence in solid $^4$He [70], but several studies disagree with this claim [71]. While the SS phase in $^4$He remains elusive and controversial, the recent achievements in ultra-cold atoms in optical lattices have renewed the interest in studying the SS phase in these systems.

The short-range Van der Waals interactions are essential in the standard BH model. This model does not realize the SS phase due to the short-range interaction. However, recent achievements in dipolar bosons with permanent or induced magnetic or electric dipoles have paved the way for realizing quantum gases with long-range interaction and understanding the phenomena of supersolidity. Rydberg atoms are also promising in engineering long-range interactions. A breakthrough in the area is the experimental realization of Bose-Einstein condensation (BEC ) in $^{52}$Cr atoms [72]–[75]. More realizations follow this in lanthanides: dysprosium Bose and Fermi gases [76], erbium[77], [78], and polar molecules with significant electric dipole moments [79]. The anisotropy and finite dipole interactions do not allow the replacement of inter-particle interaction by the isotropic contact potential. The dipole moment gives rise to the long-range interactions decaying as $r^{-3}$ ($r$ is the inter-particle distance) in addition to short-range interactions [40], [73], [79]–[82].

$$V(r-r') = \frac{4\pi\hbar a_s}{m}\delta(r-r') + \frac{d^2}{4\pi\epsilon_0}\frac{1-3\cos^2(\theta)}{|r-r'|^3} \tag{4.1}$$

Here, $|r-r'|$ is the relative position of dipoles, and $d$ and $\theta$ dipole moment and po-

larization angle, respectively. The first term contributes to the on-site interactions followed by the off-site interactions in Eq. (4.1).

## 4.2 Extended Bose-Hubbard Model

The long-range nature of the interaction is essential when the optical lattice is loaded with dipolar ions or Rydberg atoms. The ultra-cold dipolar atom trapped in optical lattices, as depicted by the extended Bose-Hubbard (EBH) model, is

$$\hat{H} = -t\sum_{j}\left(\hat{a}_{j+1}^{\dagger}\hat{a}_{j} + \hat{a}_{j}^{\dagger}\hat{a}_{j+1}\right) + \frac{U}{2}\sum_{j}\hat{n}_{j}(\hat{n}_{j}-1) + V\sum_{j}\hat{n}_{j}\hat{n}_{j+1} - \mu\sum_{j}\hat{n}_{j} \tag{4.2}$$

where $\hat{a}_j^{\dagger}$, $\hat{a}_j$ and $\hat{n}_j$ are, respectively, creation, annihilation, and number operator for site $j$ and satisfy $[\hat{a}_i, \hat{a_j}^{\dagger}] = \delta_{ij}$. $t$, $\mu$, and $U$ are the hopping amplitude, chemical potential, and on-site interaction, respectively, as in the Bose-Hubbard model (2.1). $V$ is the strength of nearest-neighbour interactions and is taken to be repulsive in this study. Due to long-range interaction, interesting phenomena appear in this model: superfluidity, phase separation, supersolidity, and density wave. The phase diagram of the extended Bose-Hubbard model described by the earlier studies using the density matrix renormalization group (DMRG) [45], [54], [83]–[85] and Quantum Monte-Carlo [86], [87] focuses primarily on the commensurate densities. We use the density matrix renormalization group with mean-field (CMFT+DMRG) and the DMRG method to extend these studies to incommensurate densities. We primarily focus on superfluid, phase-separated, supersolid, and density wave phases.

We have discussed the CMFT+DMRG scheme for the EBH model in chapter 2. In this method, the mean-field theory is used to decouple the clusters and the DMRG to obtain the ground state energy and the wave function of the cluster Hamiltonian. Since the CMFT+DMRG works in the grand canonical ensemble, studying the model (4.2) for a wide range of parameter space is possible.

The on-site interaction supports uniform densities on all sites; however, the nearest neighbour interactions create imbalances in the density at neighbouring sites. Nearest-neighbour interaction allows us to consider the lattice as a bipartite-lattice consisting of sub-lattice $A$ and $B$. The CMFT+DMRG procedure for the bipartite lattice is described in Sec. 2.1.4.2.

The CMFT+DMRG method allows us to calculate the superfluid order parameters and densities. In addition, it also allows us to calculate the correlators used to calculate condensate fraction $n(k=0)$ and structure factor $S(k)$ defined by

$$n(k) = \frac{1}{L^2} \sum_{j,j'} \langle \hat{a_j}^\dagger \hat{a}_{j'} \rangle e^{ik(j-j')}. \tag{4.3}$$

and

$$S(k) = \frac{1}{L^2} \sum_{j,j'} \langle \hat{n_j} \hat{n}_{j'} \rangle e^{ik(j-j')}. \tag{4.4}$$

The condensate fraction gives the fraction of bosons in condensate, and its value increases in the superfluid phases. The structure factor $S(k=\pi)$ is used to identify the supersolid and density wave phases. In the SF and MI phases, the $S(\pi) = 0$ as the densities are uniform across the lattice. In the density wave (DW) and supersolid (SS) phases, the densities at $A$ and $B$ sub-lattices are different, and $S(\pi)$ is finite.

The phases are characterized using the average density $\rho = (\rho_A + \rho_B)/2$, the density wave order parameter $\Delta = |\rho_A - \rho_B|$, the average superfluid order parameter $\psi = (\psi_A + \psi_B)/2$, and $\delta\psi = |\psi_A - \psi_B|$. Here $\psi_A = \psi(\frac{L+1}{2})$, $\psi_B = \psi(\frac{L-1}{2})$. Similarly, $\rho_A = \rho(\frac{L+1}{2})$, $\rho_B = \rho(\frac{L-1}{2})$. Two centrally located sites which belong to $A(B)$ sub-lattices are $\frac{L+1}{2}$ ($\frac{L-1}{2}$). In the SF and MI phases, the densities and superfluid order parameters are uniform for $A$ and $B$ sites. Subsequently, we get $\Delta = \delta\psi = 0$ and finite $\psi$ in the SF phase. In the MI phase, $\psi = 0$ and an integer $\rho$. The density wave has alternating densities with $\psi = \delta\psi = 0$, finite $\Delta$

| Phase | $\psi$ | $\rho$ | $\delta\psi$ | $\Delta$ |
|---|---|---|---|---|
| SF | Finite | Finite | 0 | 0 |
| MI | 0 | Integer | 0 | 0 |
| DW | 0 | Integer or half-integer | 0 | Finite |
| SS | Finite | Finite | Finite | Finite |

Table 4.1: Order parameter values and density for SF, MI, DW, and SS phase

and commensurate $\rho$. The SS phase has crystalline order with SF nature; hence, in the case of the SS phase, we get finite $\rho$, $\Delta$, $\psi$, and $\delta\psi$. We summarize the behaviour of the order parameters and densities in different phases in Table 4.1.

In addition, two more phases are predicted in the extended Bose-Hubbard model: solitonic phase [88], [89] and phase-separated phase [90]–[92]. The long range crystalline order at the commensurate densities in the DW phase is destroyed by the addition or removal of bosons in the ground state, resulting in modulation in the $\langle n_i \rangle$ to minimise the ground state energy [88], [89], [93]. The solitonic phase has $\rho$, $\Delta$, $\psi$, and $\delta\psi$ are finite but show oscillating behaviour. Also, the structure factor peak deviated from $k = \pi$ by a modulation vector $k_m$. The phase-separated (PS) phase has the density wave, and the superfluid phases are separated in the system. The compressibility $\kappa = \frac{d\rho}{d\mu}$ is infinite in this phase, reflected as a discontinuous jump in the $\rho$-$\mu$ plot [90]–[92], [94].

We perform the CMFT+DMRG calculations on the extended Bose-Hubbard model ( 4.2) by retaining up to $M_S = 75$ eigenstates in the left/right block-reduced density matrix. The weights of discarded states of the reduced density matrix are $10^{-8}$. We keep the maximum number of bosons per site $n_{max} = 1$ in the hard-core limit ($U \to \infty$) and $n_{max} = 5$ in the soft-core (finite $U$) case. The five bosons per site give accurate results up to $\rho < 4$ in all the phases. We set $t = 1$. The length of the lattice varies from 3 to 1001. Near the phase boundaries, however, to resolve the phases, the size is increased to 5001. We study the extended Bose-Hubbard model in two limits: hard-core and soft-core. We begin with the hard-core case below.

### 4.2.1 Hard-core case

In the hard-core limit ($U = \infty$), the maximum number of particles per site is restricted to $n_{\max} = 1$, reducing the basis for the site $\{|n_i\rangle\}$ to $|0\rangle$ and $|1\rangle$. In this limit, the EBH model maps into the quantum spin-1/2 model. Using the standard Jordon Wigner transformation

$$\begin{aligned} \hat{a}_i &= S_i^- \\ \hat{a}_i^\dagger &= S_i^+ \\ \hat{n}_i &= S_i^z - \frac{1}{2}, \end{aligned} \tag{4.5}$$

where $S_i^x, S_i^y, S_i^z$ are the spin operators at site $i$ and $S_i^+$ $(S_i^-) = S_i^x + iS_i^y$ $(S_i^x - iS_i^y)$ is the spin raising (lowering) operator. The states $|0\rangle$ and $|1\rangle$ map to spin states $|\downarrow\rangle$ and $|\uparrow\rangle$ respectively, and the $S_i^+, S_i^-$ and $S_i^z$ operators acts on these states as follows.

$$\begin{aligned} S_i^+|\downarrow\rangle &= |\uparrow\rangle \quad \rightarrow \hat{a}_i^\dagger|0\rangle = |1\rangle \\ S_i^+|\uparrow\rangle &= 0 \quad \rightarrow \hat{a}_i^\dagger|1\rangle = 0 \end{aligned} \tag{4.6}$$

$$\begin{aligned} S_i^-|\uparrow\rangle &= |\downarrow\rangle \quad \rightarrow \hat{a}_i|1\rangle = |0\rangle \\ S_i^-|\downarrow\rangle &= 0 \quad \rightarrow \hat{a}_i|0\rangle = 0 \end{aligned} \tag{4.7}$$

$$\begin{aligned} S_i^z|\downarrow\rangle = -\frac{1}{2}|\downarrow\rangle \quad &\rightarrow (\hat{n}_i - \frac{1}{2})|0\rangle = -\frac{1}{2}|0\rangle \\ S_i^z|\uparrow\rangle = \frac{1}{2}|\downarrow\rangle \quad &\rightarrow (\hat{n}_i - \frac{1}{2}|1\rangle = \frac{1}{2}|1\rangle. \end{aligned} \tag{4.8}$$

The mapped spin Hamiltonian is given by

$$\begin{aligned}\hat{H} =& -t\sum_{\langle i,j\rangle}(S_i^+S_j^- + S_i^-S_j^+) + V\sum_{\langle i,j\rangle}(S_i^z+\frac{1}{2})(S_j^z+\frac{1}{2}) - \mu\sum_i(S_i^z+\frac{1}{2}) \\ =& -t\sum_{\langle i,j\rangle}(S_i^+S_j^- + S_i^-S_j^+) + V\sum_{\langle i,j\rangle}(S_i^zS_j^z + S_i^z + \frac{1}{4}) - \mu\sum_i(S_i^z+\frac{1}{2}) \\ =& -t\sum_{\langle i,j\rangle}(S_i^+S_j^- + S_i^-S_j^+) + V\sum_{\langle i,j\rangle}S_i^zS_j^z - (\mu - \frac{Vz}{2})\sum_i S_i^z + \frac{NVz-2\mu}{4}.\end{aligned} \tag{4.9}$$

The last term in the Hamiltonian is constant and will only shift the energy by $\frac{NVz-2\mu}{4}$. Without any loss of generality, we write $\hat{H}$ as

$$\hat{H} = -t\sum_{\langle i,j\rangle}(S_i^+S_j^- + S_i^-S_j^+) + V\sum_{\langle i,j\rangle}S_i^zS_j^z - (\mu - \frac{Vz}{2})\sum_i S_i^z \tag{4.10}$$

Substituting $S_i^{\pm} = S_i^x \pm iS_i^y$, we get

$$\hat{H} = -2t\sum_{\langle i,j\rangle}(S_i^xS_j^x + S_i^yS_j^y) + V\sum_{\langle i,j\rangle}S_i^zS_j^z - H_z\sum_i S_i^z \tag{4.11}$$

where $H_z = \mu - \frac{Vz}{2}$. For $\mu = \frac{zV}{2}$, spin Hamiltonian maps into a studied XXZ model, which shows XY ordering to Ising order at $V = 2t$. In the language of bosons, XY ordering is the superfluid order, and Ising order stands for the density wave. We now reproduce these known results using the CMFT+DMRG to validate the method before discussing the soft-core cases.

First, we focus on $\rho = \frac{1}{2}$ to study the DW to SF transition. This is achieved by taking $\mu = V$ in the model(4.2), i.e., $H_z = 0$ in model(4.11). Here, we expect Berezinskii–Kosterlitz–Thouless (BKT) transition from the superfluid phase (equivalent to XY order) to the density wave phase (Ising order) at $V = 2$ [58]. Employing the CMFT+DMRG method, we calculate, self-consistently, the order parameters $\rho, \Delta, \psi$, and $\delta\psi$ to characterize different phases. In Fig. 4.1, we plot $\psi$, $\Delta$, condensate fraction $n(0)$, and $S(\pi)$ as a function of $V$. The superfluid order parameter $\psi_A = \psi_B = \psi$ is finite in the SF phase and vanishes in the density

wave phase with a universal discontinuity at the transition $V = 2$. Similarly, the density wave order parameter is finite in the density wave phase and vanishes in the SF phase with a discontinuity at $V = 2$. The condensate fraction $n(0)$ and $S(\pi)$ also show similar discontinuity at $V = 2$. These results are consistent with the BKT transition between the SF and DW phases.

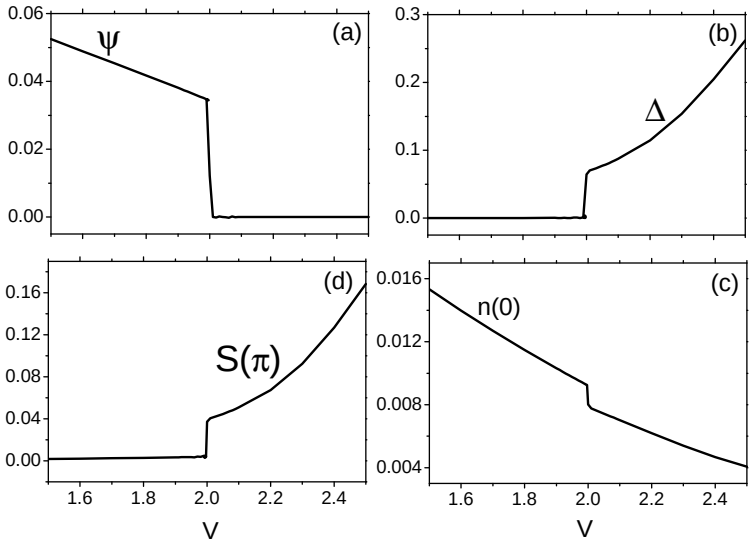


Figure 4.1: (a) superfluid order parameter, (b) density wave order parameter, (c) condensate fraction, and (d) $S(\pi)$ across SF to DW phases.

For incommensurate densities, i.e., $\rho \neq \frac{1}{2}$ and for commensurate density $\rho = \frac{1}{2}$ with $V < 2t$, the system is in the solitonic (SL) or in the SF phases. In Fig. 4.2, we plot $\rho,\ \Delta,\ \psi$, and $\delta\psi$ as a function of chemical potential $\mu$ for two values of $V$. The system is in the SF phase for $V = 1$ for all densities, Figs. 4.2(a) and (d), where we find finite $\psi$, but $\delta\psi = 0$ and $\Delta = 0$. For $V = 3$, however, we find two phases: the solitonic phase when $\rho \neq \frac{1}{2}$ and density wave for $\rho = \frac{1}{2}$. Fluctuation in the $\psi$, described below, is a consequence of the solitonic phase.

To characterize the solitonic phase, we now plot, for a system size $L = 1001$, $\psi_j$ and $\rho_j$ versus $j$ for $450 < j < 550$ for $V = 1$ in 4.3(upper panel) and $V = 3$ in 4.3(lower panel). We choose the range of lattice position $j$ far away from the edges to avoid the fluctuation effect due to mean-field decoupling. We consider three values of the chemical potential $\mu = 1,\ 2$, and 3 such that $\rho$ is close to $\frac{1}{2}$.

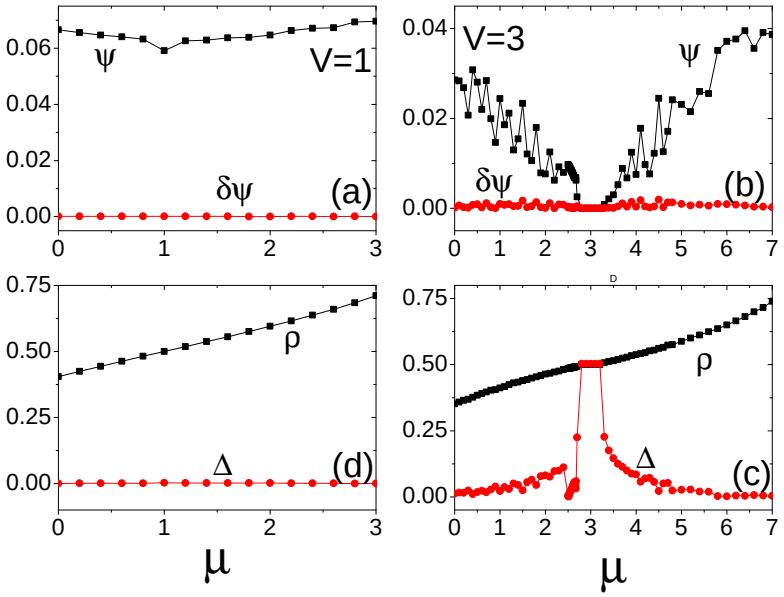


Figure 4.2: $\psi$, $\delta\psi$, $\rho$ and $\Delta$ plotted as a function of $\mu$ for $V = 1.0$ (left panel) and $V = 3.0$ (right panel)

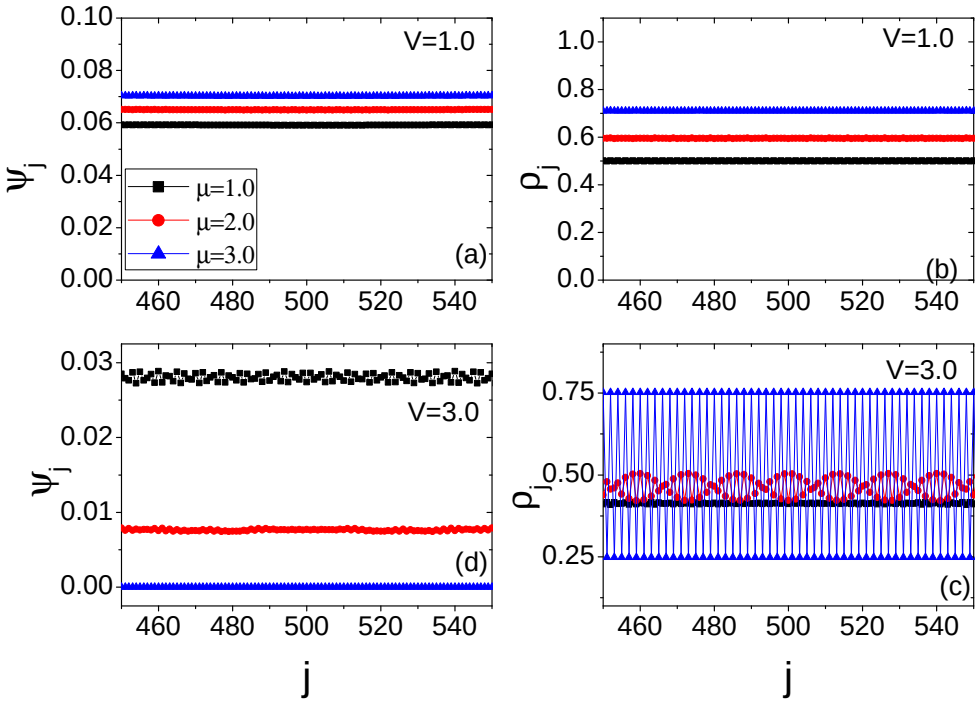


Figure 4.3: Plots of $\psi_i = \langle a_i \rangle$ and $\rho_j = \langle n_i \rangle$ as a function of lattice position $i$ for $\mu = 1.0,\ 2.0,\ 3.0$, $U = \infty$ and $V = 1.0$(top panel) and $V = 3.0$(bottom panel).

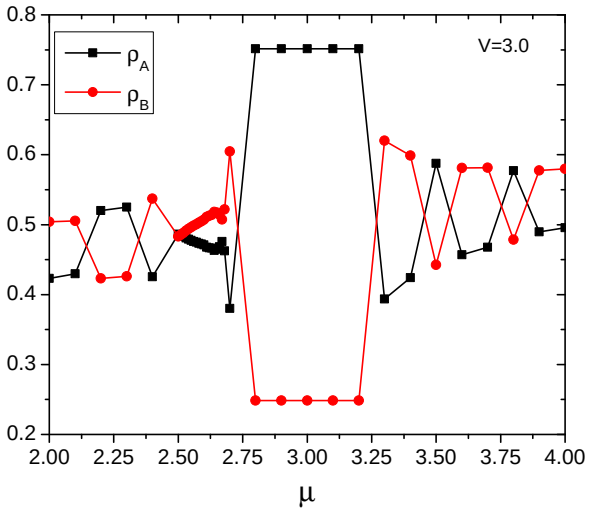


Figure 4.4: $\rho_A = \rho_{\frac{L+1}{2}}$ and $\rho_B = \rho_{\frac{L-1}{2}}$ plotted as function of lattice position $\mu$ for $V = 3.0$.

For $V = 1$, we find, for all three values of $\mu$, uniform $\psi_j$ and $\rho_j$, signatures of superfluid phase. However, for $V = 3$, we see different behavior of $\rho_j$ for $\mu = 1,\ 2$ and 3. For $\mu = 1$, $\psi_j$ shows small oscillation, and $\rho_j$ is more or less uniform with a value $\rho \approx 0.4$. However, for $\mu = 2$, $\psi_j$ is small and again shows small oscillation, but density $\rho_j$ shows a clear oscillation, a feature of the solitonic phase [88], [89]. For $\mu = 3$, the system is in the density wave phase with $\psi_j = 0$ and $\rho_j$ staggered between 0.75 and 0.25 with average $\rho = \frac{1}{2}$. The solitonic phase has oscillating $\rho_j$ and finite $\psi_j$.

In Fig. 4.3 we plot $\rho_A = \rho_{\frac{L+1}{2}}$ and $\rho_B = \rho_{\frac{L-1}{2}}$, two adjacent sites belong to $A$ and $B$ sub-lattices, to demonstrate that the solitonic phase sandwich the $\rho = \frac{1}{2}$ density wave phase. The plateau in the $\rho - \mu$ plot, vanishing $\psi$ and $\delta\psi$, finite density wave order parameter $\Delta$, confirm the density wave phase. The variation of $\rho_A$ and $\rho_B$ on either side of the density wave is due to the solitonic phase where the density is expected to oscillate as shown in the Fig. 4.3(c). We thus confirm that the phase diagram of the extended Bose-Hubbard model in the hard-core limit consists of superfluid, solitonic, and density wave phases, which agrees with the earlier results [88], [89].

### 4.2.2 Soft-core case

Now, we move our attention to the soft-core limit. Earlier studies primarily focused on the phase diagram around density $\rho = 1$ and for interactions $U \leq V$. These studies found three insulator phases for density $\rho = 1$ when interactions dominate the hopping matrix, i.e., $(U,\ V) > t$. Haldane insulator phase sandwiched between the Mott insulator $V < U/2$ and the density wave phases ($V > U/2$) [45], [54], [83]–[85]. The superfluid and supersolid phases dominate the weak interaction region of the phase diagram. Away from the integer density, the phase diagram of the model (4.2) consists of superfluid, supersolid, and solitonic phases [95], [96]. In addition to these phases, a recent study predicts a phase-separated phase when the nearest neighbour interaction dominates the on-site interaction [90], [92]. The superfluid and density wave phases are separated in this phase. In this thesis, we focus on the region of the phase diagram where the nearest neighbour interaction $V$ dominates over the on-site interaction $U$ and study the phase-separated phase in detail. We consider two values of nearest neighbour interactions $V = 2$ and 4 and check the phase diagram varying on-site interaction $U$ and $\rho$.

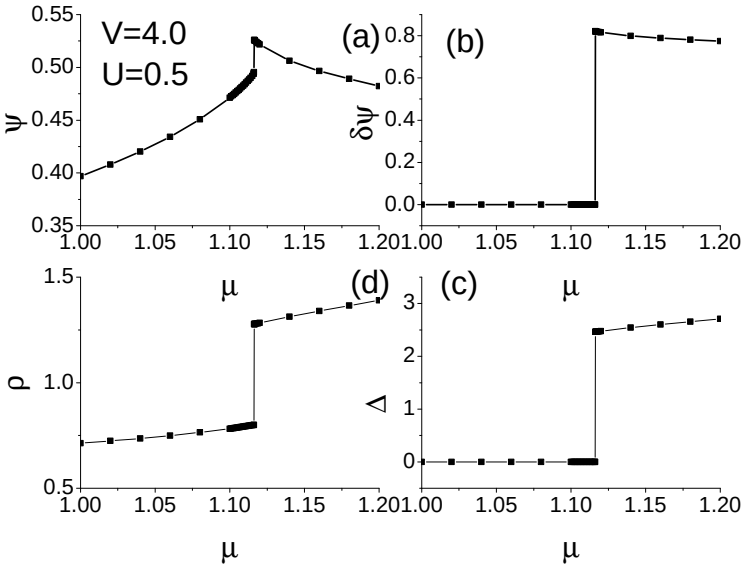


Figure 4.5: (a) $\psi$, (b) $\delta\psi$, (c) $\Delta$, and (d) $\rho$ plotted as a function of $\mu$ for a fixed $V = 4.0$ and $U = 0.5$.

First, we discussed the case $V = 4$. In Figs. 4.5, we plot order parameters $\psi = (\psi_A + \psi_B)/2$, $\rho = (\rho_A + \rho_B)/2$, $\delta\psi = |\psi_A - \psi_B|$ and $\Delta = |\rho_A - \rho_B|$ as a function of $\mu$ for $U = 0.5$. Three distinct regions can be seen in the Fig. 4.5 namely; (i) the SF phase; $\psi > 0$, $\Delta = 0$ for $\mu \leq 1.1162$, (ii) the supersolid phase; $\psi > 0$, $\Delta > 0$ for $\mu \geq 1.1163$, and (iii) the phase-separated phase; $\kappa = \frac{d\rho}{d\mu} = \infty$ for $0.800 < \rho < 1.277$. The SF-PS phase transition happens at critical density $\rho_C^{(SF-PS)} = 0.800$, and the PS-SS transition at $\rho_c^{(PS-SS)} = 1.277$. These critical densities are in agreement with earlier reported values [90], [92]. The CMFT-DMRG method works in the grand-canonical ensemble; hence, the density is not fixed. The density jumps from 0.800 to 1.277 when the chemical potential increases from $\mu = 0.1163$ to 0.1164. This sharp increase in the density reflects that the compressibility diverges at $\mu_C = 0.11635$. Divergence of compressibility reflects the phase-separation of two phases: the SF and the SS. The transition from superfluid to supersolid is through a phase-separated phase. In Fig. 4.6 we plot $\psi_j$ and $\rho_j$ for two values of $\mu$ on either side of $\mu_C$. For $\mu = 1.10$, $\psi_j$ and $\rho_j$ are uniform signaling superfluid phases. However, for $\mu = 1.12$, both $\psi_j$ and $\rho_j$ stagger with finite average $\psi$ and $\Delta$. The supersolid phase is characterized by finite superfluid and density wave order parameters. So, as we increase the chemical potential, the system goes from superfluid to supersolid discontinuously. The transition from superfluid to supersolid is through a phase-separated phase.

Phase-separated phase can be observed only at fixed density because $\frac{d\rho}{d\mu} = \infty$. In the case of $V = 4.0$, $U = 0.5$, from the Fig 4.5, the phase-separated phase is possible for $\rho_C^{SF-PS} < \rho < \rho_C^{PS-SS}$. To understand the phase-separated phase, we perform a DMRG calculation keeping fixed density $\rho_C^{SF-PS} < \rho < \rho_C^{PS-SS}$. In Fig 4.7, we plot the variation of $\rho_j$ with lattice position $j$ for $V = 4.0$, $U = 0.5$ and the average density $\rho = 1$. The DMRG calculation is performed for a system size $L = 301$. Since the density is fixed, $\psi_j = 0$ in the DMRG calculation, we plot only $\rho_j$. The PS phase is characterized by two distinct regions: the supersolid phase at the edge regions and the superfluid phase at the center region, as shown in Fig 4.7.

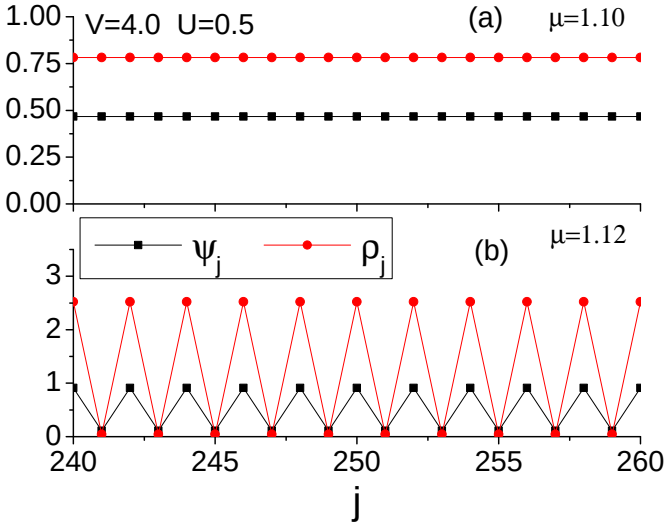


Figure 4.6: Variation of $\psi_j$ and $\rho_j$ with lattice position $j$ for (a) $\mu = 1.10$ and (b) $\mu = 1.12$ for $V = 4.0$ and $U = 0.5$.

The superfluid and supersolid region changes with density. We plot $\rho_j$ versus $j$ for five different densities in Fig. 4.8. These plots are obtained from the DMRG calculation keeping $L = 301$ and taking several bosons $N = 185,\ 270,\ 301,\ 330,$ and 399. For $\rho = 0.615 < \rho_C^{(SF-PS)}$, the whole lattice is in the SF phase as shown in the Fig. 4.8 the lower panel. As we increase the density, the SS phase appears at the edges and is phase-separated from the SF phase. With a further increase in density, the SS phase grows at the expense of the SF phase, and eventually, the whole lattice is in the SS phase for $\rho > \rho_C^{(PS-SS)}$. In Fig. 4.9(a), we plot the length of the superfluid region as a function of $\rho$ for $U = 0.5$ and $V = 4.0$. The superfluid region decreases monotonically as the density increases from $\rho_C^{SF-PS}$ to $\rho_C^{PS-SS}$. Similar behaviour is also seen in the case of other $U$ values. For example, in Fig. 4.9(b), we plot the length of the superfluid region as a function of $\rho$ for $U = 1.2$ and $V = 4.0$.

Increasing the on-site interaction reduces the phase-separated region. In addition, we also get the transition from SF to DW through the PS phase. For example, in Fig. 4.10 we plot order parameters $\psi$, $\rho$, $\delta\psi$ and $\Delta$ as a function of $\mu$ for $U = 1.3$. Four distinct regions can be seen in the Fig. 4.10 namely; (i) the SF phase; $\psi > 0$, $\Delta = 0$ for $\mu \leq 2.1$, (ii) the density wave phase; $\psi = 0$, $\rho = 1$,

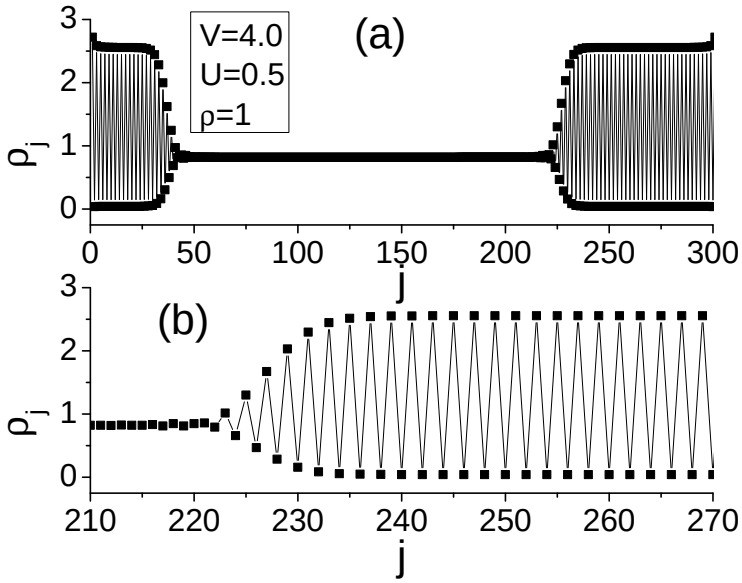


Figure 4.7: Variation of $\rho_j$ with lattice position $j$ from the DMRG calculation fixing density $\rho = 1$ for $V = 4.0$, $U = 0.5$. The lower panel is the expanded supersolid region.

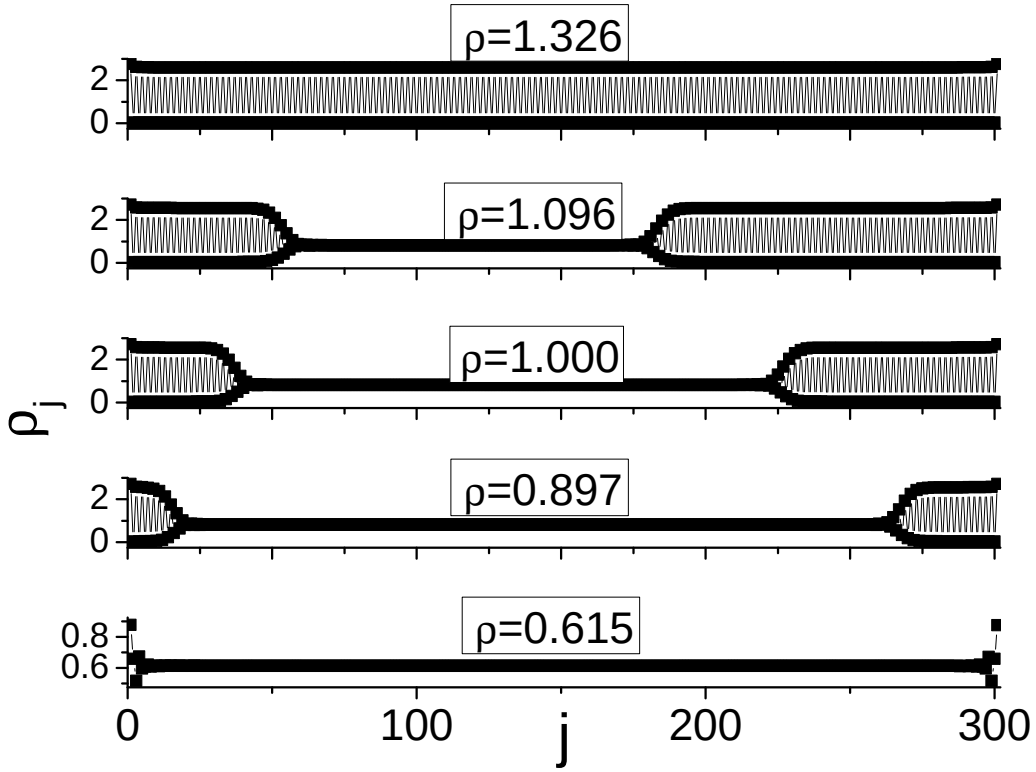


Figure 4.8: Variation of $\rho_j$ versus $j$ for five different densities from DMRG calculation with $L = 301$. Number of bosons $N = 185,\ 270,\ 301,\ 330$, and 399, corresponding to the densities $\rho = N/L = 0.615,\ 0.897,\ 1.0,\ 1.096$, and 1.326.

and $\Delta > 0$ for $2.1 < \mu < 2.27$ (iii) the phase-separated phase; $\kappa = \frac{d\rho}{d\mu} = \infty$ for $0.84 < \rho < 1.0$, and (iv) the supersolid phase; $\psi > 0$, $\Delta > 0$ for $\mu \geq 2.27$.

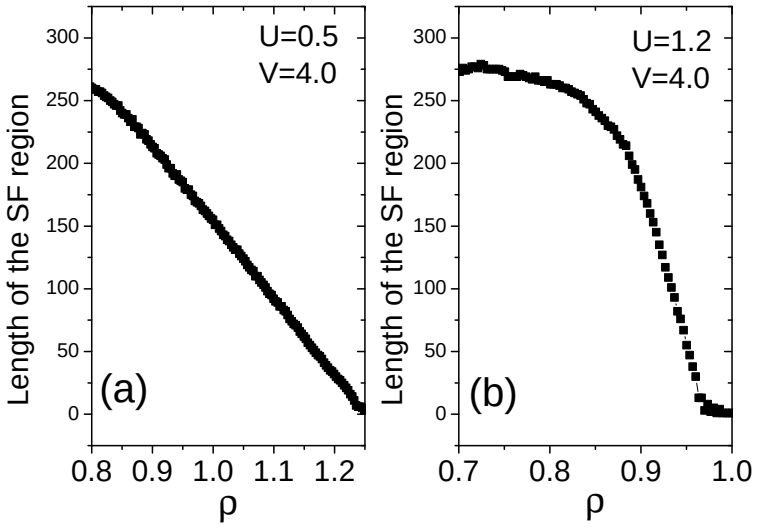


Figure 4.9: Length of the superfluid region as a function of $\rho$ for (a) $U = 0.5$ and (b) $U = 1.2$ keeping $V = 4.0$.

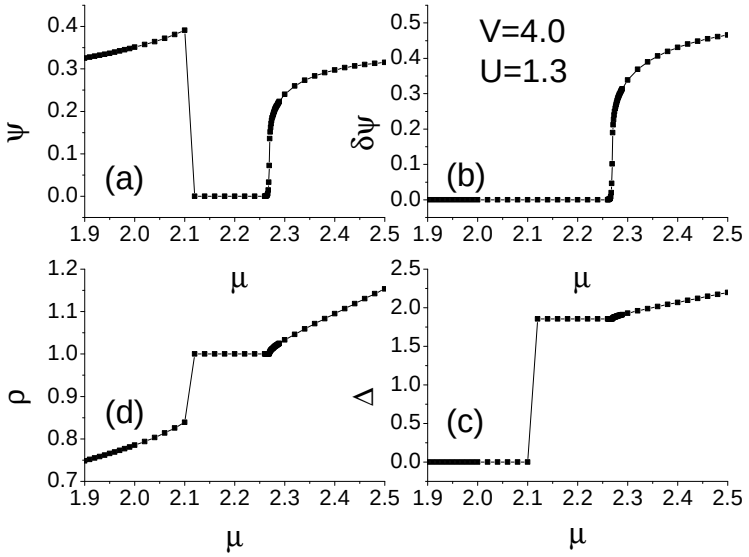


Figure 4.10: (a) $\psi$, (b) $\delta\psi$, (c) $\Delta$, and (d) $\rho$ plotted as a function of $\mu$ for a fixed $V = 4.0$ and $U = 1.3$.

The SF-PS phase transition happens at critical density $\rho_C^{(SF-PS)} = 0.84$, and the PS-DW transition at $\rho_c^{(PS-SS)} = 1.0$.

The PS phase vanishes on further increase in the on-site interaction $U$. For higher values of $U$, the transition is from SF to SS, DW, and SS. We plot in Fig 4.11, order parameters $\psi$, $\rho$, $\delta\psi$ and $\Delta$ as a function of $\mu$ for $U = 3.0$. Three distinct regions can be seen in the Fig. 4.11 namely; (i) the SF phase; $\psi > 0$, $\Delta = 0$ for $\mu \leq 3.94$, (ii) supersolid phase; $\psi > 0$ and $\Delta > 0$ for $3.94 \leq \mu \leq 3.95$, and (iii) the density wave phase; $\psi = 0$ and $\Delta > 0$ and $\rho = 1$ for $\mu > 0.95$.

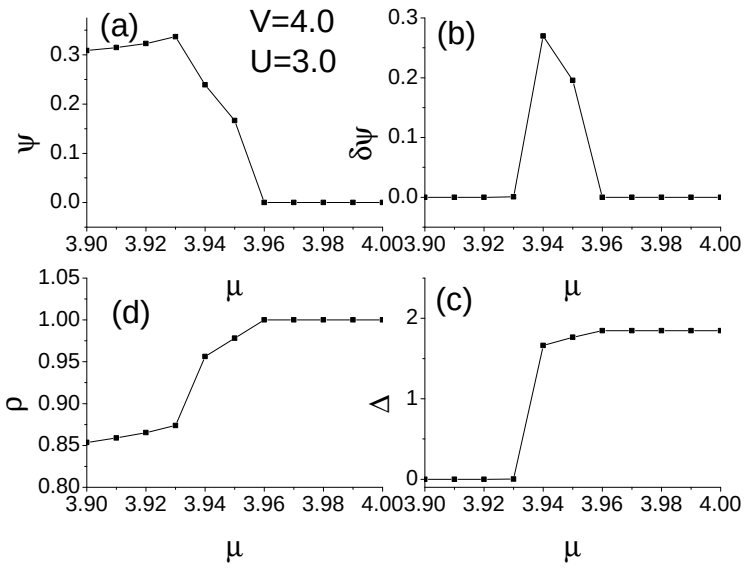


Figure 4.11: (a) $\psi$, (b) $\delta\psi$, (c) $\Delta$, and (d) $\rho$ plotted as a function of $\mu$ for a fixed $V = 4.0$ and $U = 3.0$.

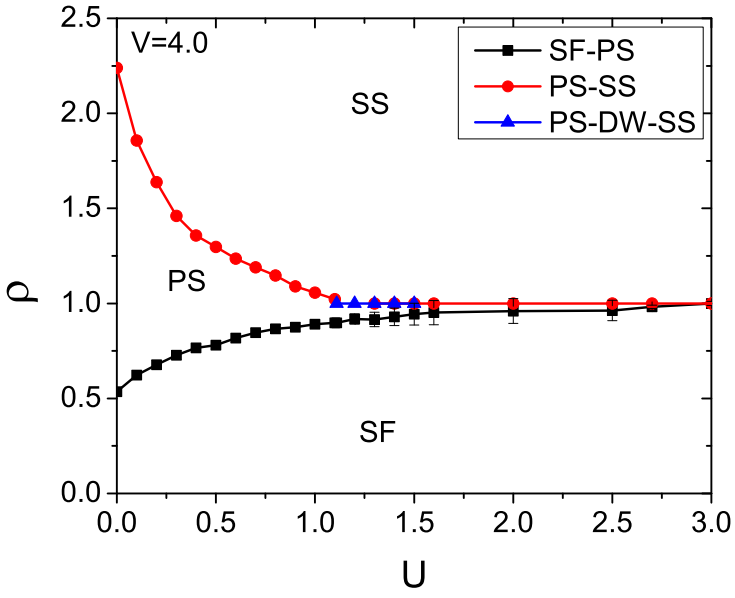


Figure 4.12: Phase diagram in $\rho - U$ for $V = 4.0$

Finally, we plot the phase diagram in the $\rho - U$ plane in Fig. 4.12. The phase diagram consists of superfluid, phase-separated, supersolid, and density wave phases. For lower values of $U$, the transition is between SF and PS and then to SS. For higher values of $U$, density wave occur, and the transitions are from SF to SS, DW, and SS. However, the supersolid and phase-separated phases with density $\rho < 1$ are very narrow. We don't get any transition from density wave to phase-separated phase for density $\rho > 1$ and in the region, the supersolid phase is

very stable.

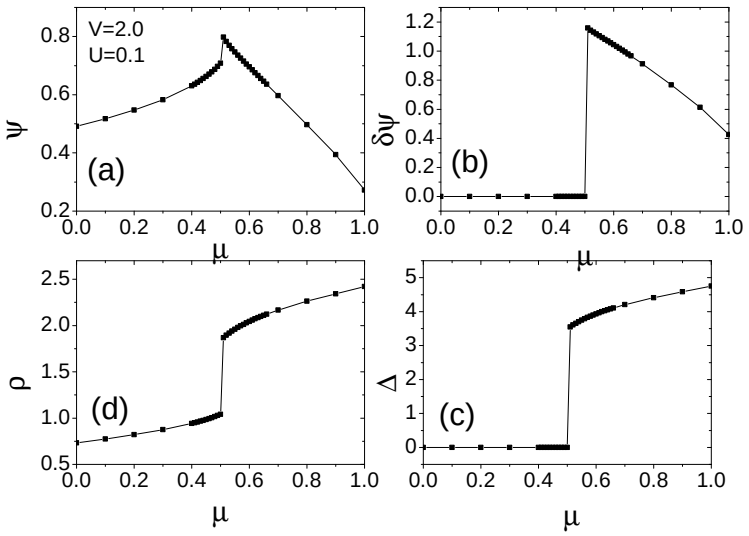


Figure 4.13: (a) $\psi$, (b) $\delta\psi$, (c) $\Delta$, and (d) $\rho$ plotted as a function of $\mu$ for a fixed $V = 2.0$ and $U = 0.1$.

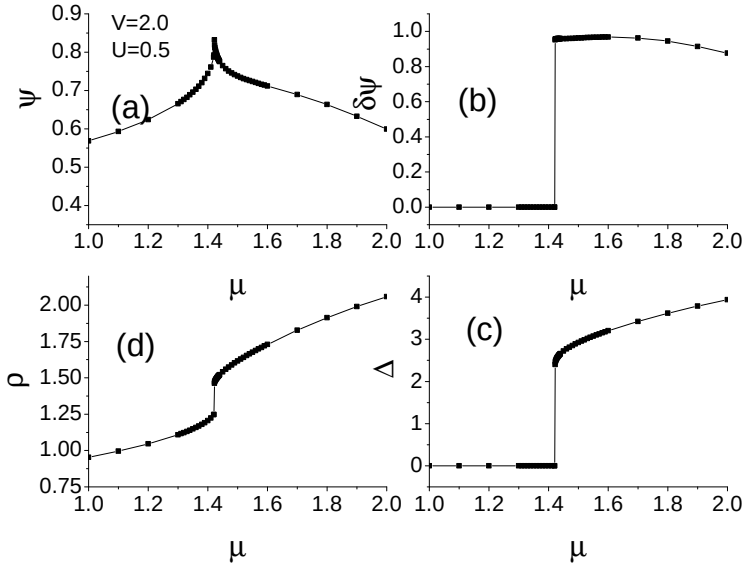


Figure 4.14: (a) $\psi$, (b) $\delta\psi$, (c) $\Delta$, and (d) $\rho$ plotted as a function of $\mu$ for a fixed $V = 2.0$ and $U = 0.5$.

Now consider the case $V = 2.0$. In Figs. 4.13, 4.14 and 4.15 we plot order parameters $\psi$, $\rho$, $\delta\psi$ and $\Delta$ as a function of $\mu$, respectively for $U = 0.1$, 0.5, and 1.0. For $U = 0.1$ and 0.5, we get superfluid, phase-separated, and supersolid phases. However, the region of the phase-separated phase is reduced in the $U = 0.5$ case compared to $U = 0.1$. For $U = 1.0$, we do not see the phase-separated phase, and the transition is directly from superfluid to supersolid. The phase diagram in

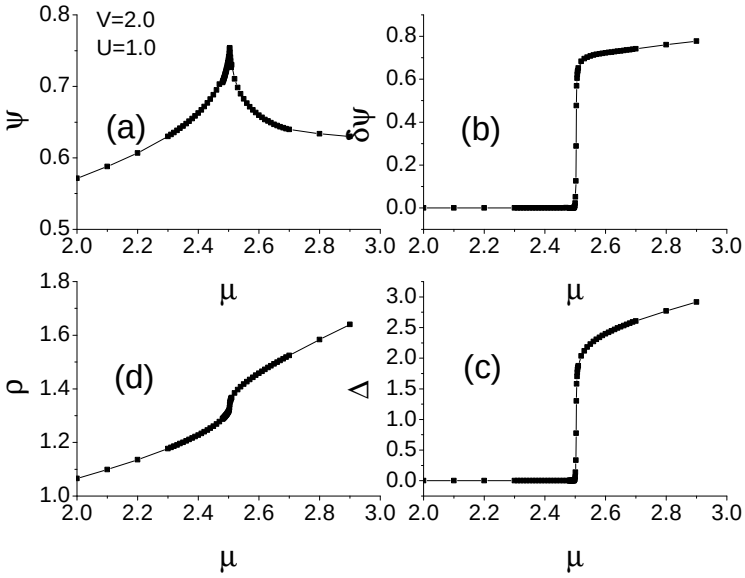


Figure 4.15: (a) $\psi$, (b) $\delta\psi$, (c) $\Delta$, and (d) $\rho$ plotted as a function of $\mu$ for a fixed $V = 2.0$ and $U = 1.0$.

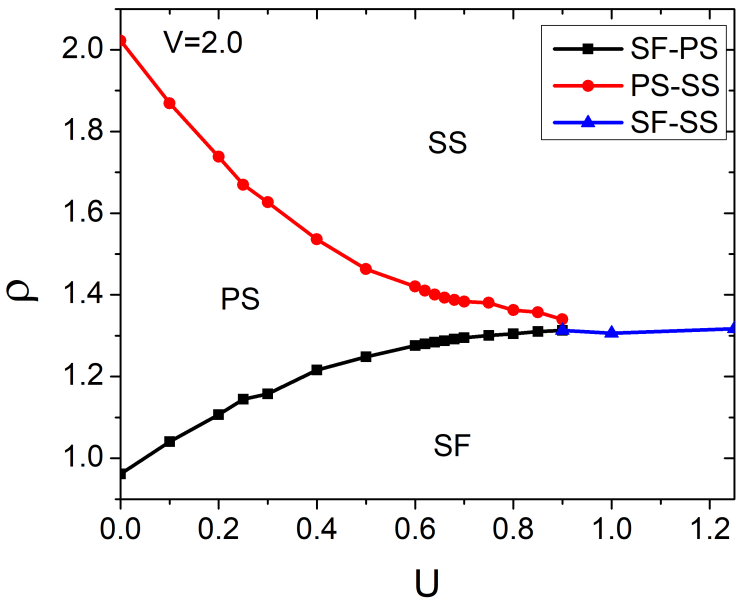


Figure 4.16: Phase diagram in $\rho - U$ for $V = 2.0$

the $\rho = U$ plane for $V = 2.0$ is plotted in Fig 4.16. Unlike the $V = 4.0$ case, we don't have a density wave for $V = 2.0$, and the phase diagram consists of SF, PS, and SS.

For $V = 2$ and 4, we do not observe the solitonic (SL) phase. However, as we shift to a higher value of $V$, we get the SL SF, PS, DW, and SS phases. We study the phase diagram for $V = 6$ for a broader range of densities and on-site interaction. We obtain the phase diagram after a detailed analysis of the order parameters $\psi$, $\rho$, $\delta\psi$, and $\Delta$ as a function of $\mu$ for on-site interaction ranging from 0 to 15 and plot in Fig. 4.17. The phase diagram is very rich and consists of SL, SF, SS, PS, DW, and MI. We see several phase transitions depending on the density and on-site interaction. For small values of $U$, we see a phase transition from SL to SF as we increase the density. Upon further increase in density, the SF phase is separated from supersolid by the phase-separated phase. For slightly larger $U$, the transition from PS to SS via DW with density $\rho = 1$. We do not get the PS phase for $U > 3$. For $U = 6 - 10$ with the increase in density, we get phase transition from SL to DW (with $\rho = 1/2$), DW to SS, SS to SF, SF to SS, SS to DW ($\rho = 1$), and finally DW to SS. We do not observe the SS phase with commensurate densities $\rho = 1/2,\ 1$. We neither observe a transition from the MI to SS varying $\mu$ or $\rho$. The transition from MI is always to SF. However, we observe DW to MI phase transition for $\rho = 1$ as predicted earlier [83].

We investigate the solitonic phase in depth using the structure factor. The solitonic phase has density modulation as shown in Fig. 4.18 where we plot $\rho_j$ versus $j$ for a set of $\mu$ values. The wavelength of the density modulation increases as we move away from the density wave. We study this behaviour using structure-function $S(k)$ defined by Eq. (4.4). The structure-function peaks at $k = \pi$ in the density wave phase. However, due to the modulation in the SL phase, the peak position of the structure-function shifts to lower values of $k$. We calculate the structure-function for different values of $\mu$ in the SL phase for $U = 8$, $V = 6$ and plot in Fig. 4.19. As we decrease the density (by changing $\mu$) from $\rho = 1/2$, the

modulations increase, and the peak position in the $S(k)$ shifts towards lower $k$. Defining the peak position in the $S(k)$ as the modulation vector $k_m$, we plot it as a function of $\mu$. We also plot $2\pi\rho$ as a function of $\mu$ and observe that $k_m \approx 2\pi\rho$.

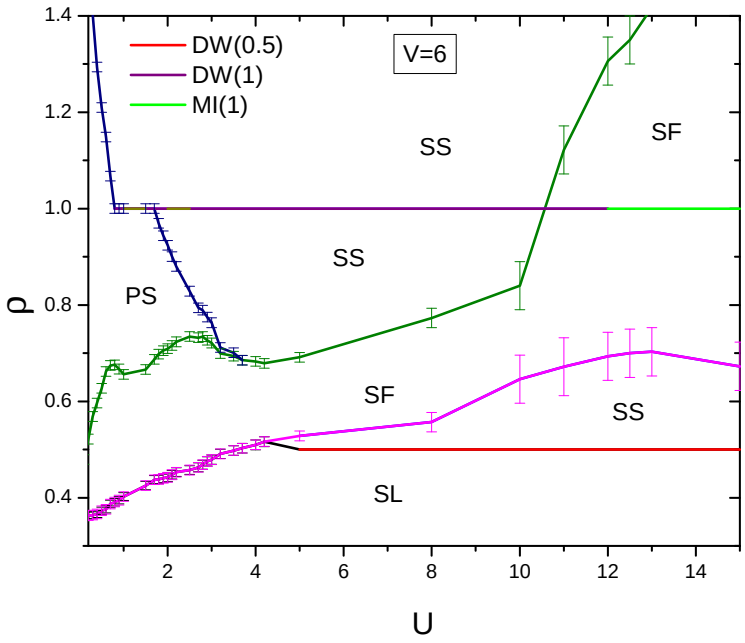


Figure 4.17: Phase diagram in $\rho - U$ for $V = 6$.

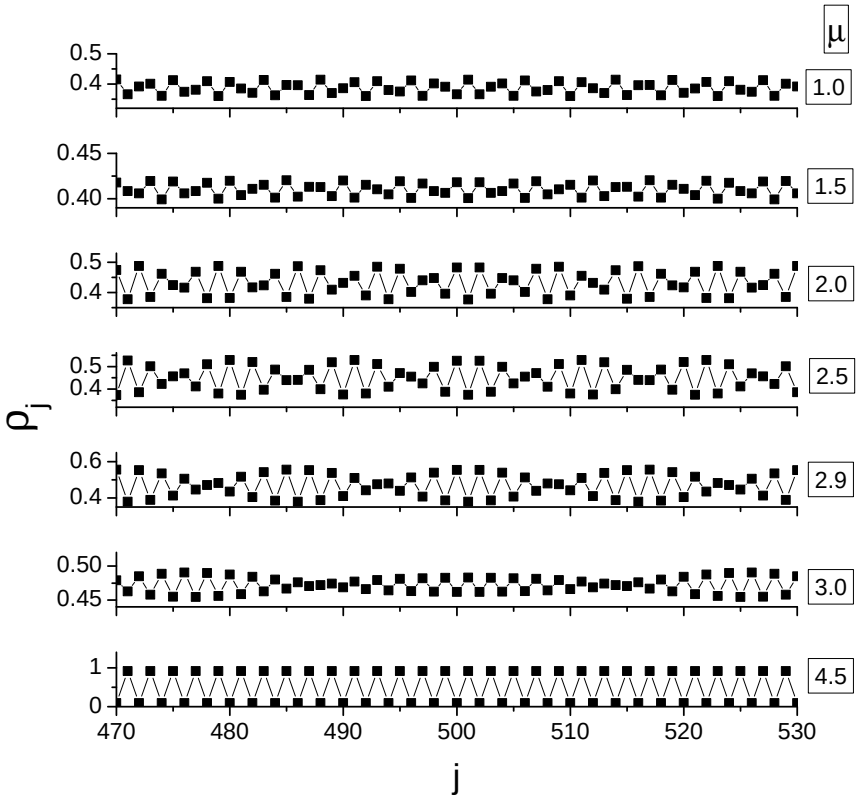


Figure 4.18: Plot of $\rho_j$ versus $j$ for a set of $\mu$ values for $V = 6.0$ and $U = 8.0$.

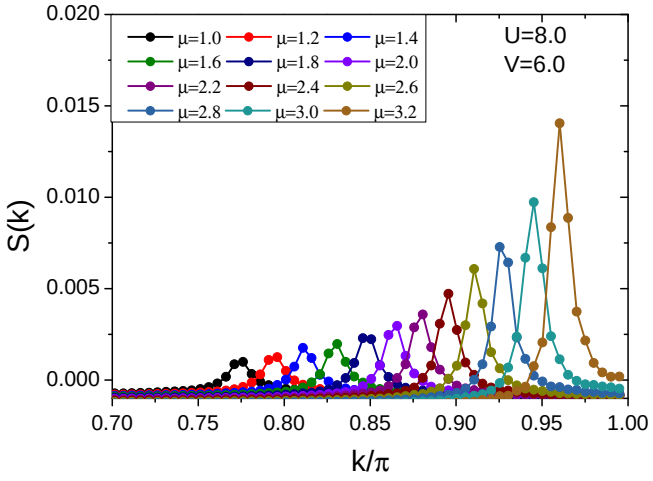


Figure 4.19: The structure factor $S(k)$ is plotted as a function of $k/\pi$ for $V = 6.0$ and $U = 8.0$ for different $\mu$. The shifted peak from $\pi$ shows the presence of SL phase.

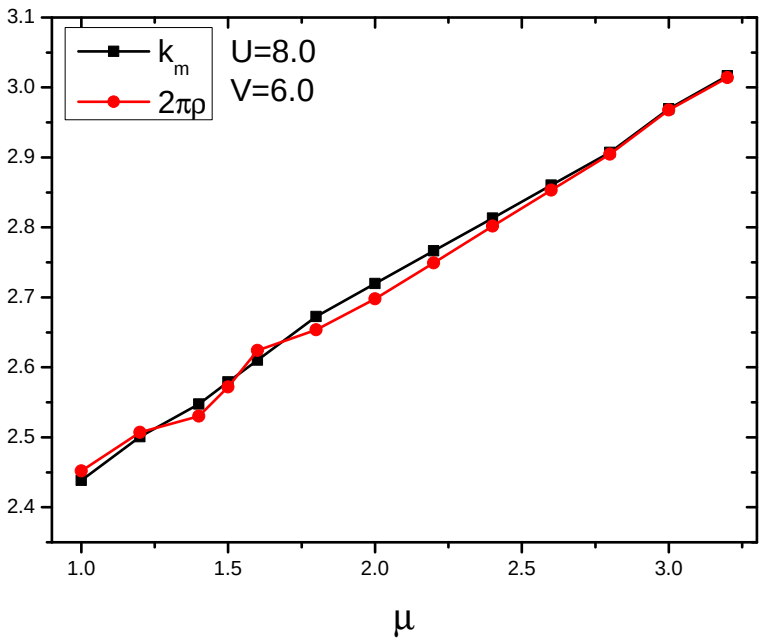


Figure 4.20: The Modulation vector $k_m$ and $2\pi\rho$ plotted as function of $\mu$.

## 4.3 Extended Bose-Hubbard Model with three body interactions

So far, we have considered the on-site and nearest neighbour interactions to understand the quantum phases in bosonic systems. These interactions are effectively two-body interactions. We neglect most higher-order interactions, assuming their strength is negligible compared to the effective two-body interactions. However, many exotic phases, such as topological and spin liquid, are associated with a Hamiltonian with three or higher-order interaction terms [97]. When the interactions are strong, the on-site interaction term deviates from the two-body. It depends on the occupational densities at the site, indicating the effect of higher Wannier bands. Recently, the dependence on density in the on-site interaction term is shown experimentally in Cs, Rb, and K, and the possibility to engineer Hamiltonians with multi-body interaction in optical systems [98]–[101].

Recent experiments have demonstrated the possibility of introducing an effective multi-body interaction in addition to the two-body interaction between the atoms in the optical lattices with sudden quench of the lattice depth [41], [102]. In

the absence of three-body interaction, even minute attractive on-site interaction leads to the collapse of the bosons on the single site. The effect of the three-body interaction in the BH model is that repulsive three-body interaction stabilizes the system against the collapse by enhancing the kinetic energy term. For repulsive $U > 0$, the BH model is in the phase coherent SF or in the MI phase when the on-site interactions are strong. The attractive three-body interaction in this case is shown to affect the MI phase with $\rho > 1$ [103], [104]. The $\rho = 1$ MI lobe is insensitive to the three-body interaction, as the hopping amplitude has to compete with only the repulsive two-body on-site interaction. On the contrary, the MI $\rho = 2$ lobe shrinks as attractive three-body interaction weakens the effective on-site interaction.

A hard-core three-body interaction model is realized when an optical lattice system has strong three-body losses [105]. Recent studies in such a model have also predicted a strange pairing of bosons, characterized by the long-range off-diagonal ordering in pair of bosons sandwiched between the MI $\rho = 1$ and $\rho = 3$ lobe. The pairing of bosons leads to a pair superfluid phase (PSF) [103], [106], [107] which leads to the shrinking of the Mott insulator lobe with density $\rho = 2$. The three-body interaction leads to atomic superfluid (ASF), PSF phase and MI phases in the BH model. The off-site interaction in BH model is seen to promote different densities at the neighbouring sites forming the DW phase, SS phase, phase separation, and the solitonic phases. We are interested in the new emergent phases due to the interplay of the multi-body on-site and off-site interactions and how they affect the stability of the existing phases.

In this section, we investigate the effect of tunable hard-core three-body interaction on the EBH model, mainly addressing its impact on the phase-separated and supersolid phases. The Hamiltonian we consider for this study is given by

$$H = -t\sum_{\langle ij\rangle}(\hat{a}_i\hat{a}_j^\dagger + h.c) + \frac{U}{2}\sum_i \hat{n}_i(\hat{n}_i - 1) + V\sum_{ij}\hat{n}_i\hat{n}_j + W\sum_i \delta_{\hat{n}_i,3} - \mu\sum_i \hat{n}_i. \tag{4.12}$$

Here, $W < 0$ is the strength of the three-body interaction. The other terms have the same meaning as in the model (4.2). The three-body interaction is engineered to be effective only when three particles are per site.

We study the Hamiltonian (4.12) using the CMFT+DMRG method discussed in the Chapter 2. The cluster Hamiltonian of size $L$ is constructed using the mean-field approximation by decoupling the neighbouring clusters using $\hat{a}_i = \langle a_i\rangle + \delta\hat{a}_i$ and $\hat{n}_i = \langle n_i\rangle + \delta\hat{n}_i$ and is given by

$$\begin{aligned}\hat{H}^C = &-t\sum_{j=1}^{L-1}\left(\hat{a}_{j+1}^\dagger\hat{a}_j + \hat{a}_j^\dagger\hat{a}_{j+1}\right) + \frac{U}{2}\sum_{j=1}^{L}\hat{n}_j(\hat{n}_j - 1) + V\sum_{j=1}^{L-1}\hat{n}_j\hat{n}_{j+1} \\ &- \sum_{j=1}^{L}\mu\hat{n}_j + \sum_{j=1}^{L}W\delta_{\hat{n}_j,3} \\ &- t\left((\hat{a}_1^\dagger + \hat{a}_1)\psi_B - \psi_A\psi_B\right) - t\left((\hat{a}_L^\dagger + \hat{a}_L)\psi_B - \psi_A\psi_B\right) \\ &+ V(\hat{n}_1 + \hat{n}_L)\rho_B - \frac{V}{2}\rho_A\rho_B.\end{aligned} \tag{4.13}$$

We carry out the CMFT+DMRG method calculations with the following parameters. The energies are scaled with $t = 1$ and are dimensionless. The $n_{\max} = 5$, sufficient for average $\rho < 3$ and keeping $M_S = 75$ states in the reduced density matrix. The weights of the discarded states are of the order $10^{-8}$.

For small $V$ and in the absence of hard-core three-body interaction, the phase transition, as we studied in the previous section in Fig. 4.16, is from the SF to SS through the PS phase for $U << V$ and gradually changing to a continuous transition from SF to SS with increasing $U$. To understand the effect of hard-core three-body interaction $W$ on the phase-separated and supersolid phases, we consider two cases: $V = 2$, $U = 0.8$, and $V = 4$, $U = 0.5$. We plot $\psi$, $\rho$, and $\Delta$ for

the former case in Fig. 4.21. For $W = -0.1$, we continue to have the transition from the SF to SS through the PS phase with no change in the critical values of the phase transition. And also see no density wave with $\rho = \frac{3}{2}$. However, as we increase the strength of $|W|$, we observe (i) the appearance of the density wave with $\rho = \frac{3}{2}$ and (ii) the enhancement of the PS phase. The density wave with $\rho = \frac{3}{2}$ has a staggering of the density $\rho_j$ between 3 and 0. $U$ being small, three body attractive interaction $W$ enhances the effective nearest neighbour interaction $V$ yielding the density wave phases. Further increase in the $W$ leads to a wider density wave region. However, the transition continues from the SF to SS through the PS phase.

In the latter case, i.e., $V = 4$, $U = 0.5$, from the Fig. 4.22, the density wave phase appears even for small $W$ with the supersolid phase existing on either side of the density wave. However, as we increase $|W|$, the PS phase enhances, as we saw in the earlier case, at the expense of the supersolid phase for $\rho < \frac{3}{2}$, and there exists direct transition from the PS to DW. The hard-core three-body interaction enhances the effective nearest-neighbour interaction in the system, and as a consequence, it enhances the phase-separated and density wave phases.

## 4.4 Conclusion

We have employed the CMFT+DMRG scheme to understand the effect of long-range and many-body interaction in optical lattice systems. We have focused our studies on the regions where the long-range and many-body interactions dominate the short-range on-site interaction. We obtain the order parameters $\psi$, $\delta\psi$, $\rho$, $\Delta$ to characterize the phases. These order parameters characterize the superfluid, phase-separated, supersolid, density wave, and Mott insulator phases. The PS phase is characterized by infinite compressibility $\kappa = \frac{d\rho}{d\mu}$, and the SL phase is characterized by the modulation in $n_i$ averages and shifted peak in the structure factor. The phase diagram of the EBH model in the hard-core limit consists of SF, DW, and SL phases. At commensurate density, $\rho = 1/2$, the BKT type transition

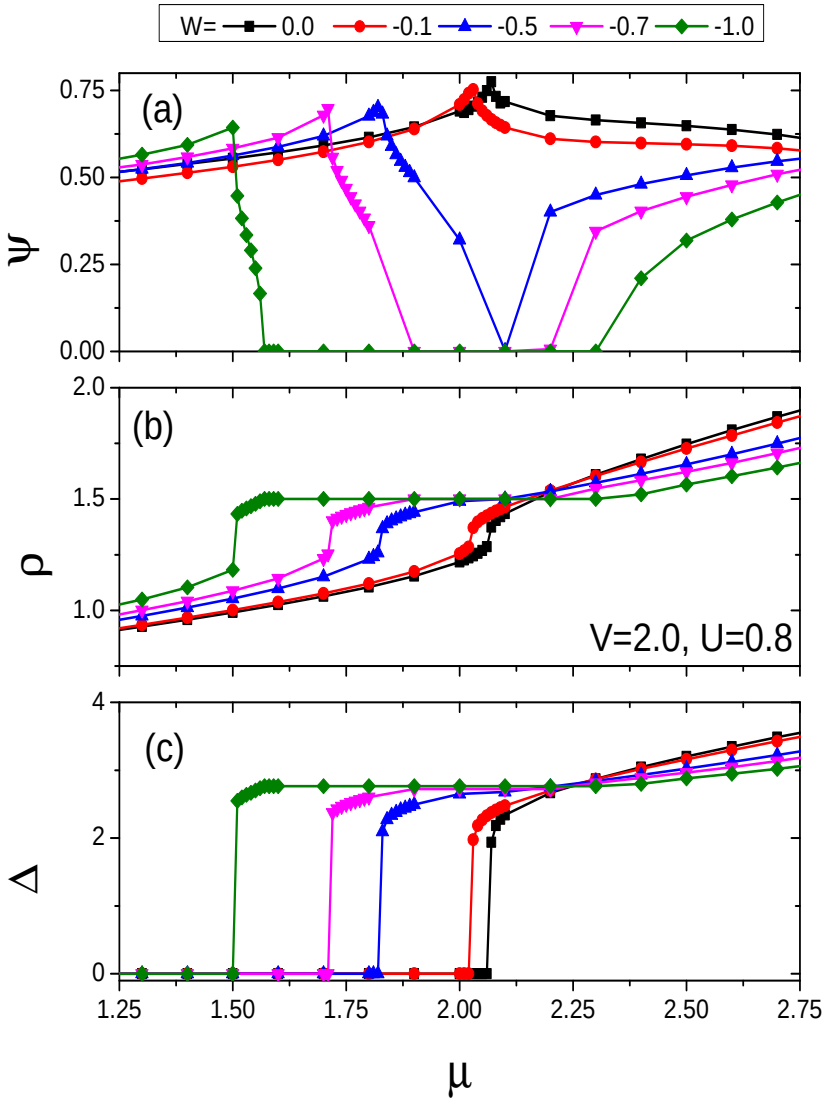


Figure 4.21: Comparison of (a) the superfluid order parameter $\psi$, (b) the density $\rho$ and (c) $\Delta$ for $U = 0.8$, $V = 2.0$ varying $W = 0, -0.1, -0.5, -0.7, -1.0$.

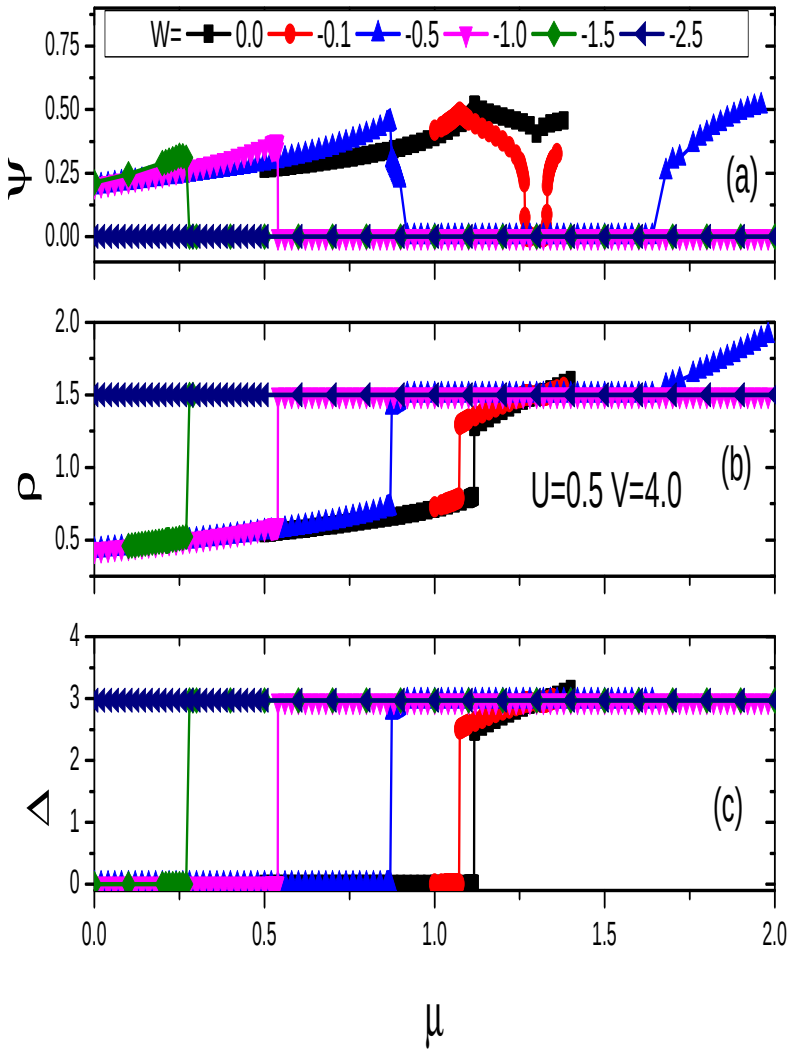


Figure 4.22: Comparison of (a) the superfluid order parameter $\psi$, (b) the density $\rho$ and (c) $\Delta$ for $U = 0.5$, $V = 4.0$ varying $W = 0, -0.1, -0.5, -1.0, -1.5, -2.5$.

from SF to DW phase is observed at $V = 2$. In the soft-core case of the EBH model, for low $V$, we see the gapless SF, SS, and PS phases. As $V$ increases, the DW and MI phases start appearing. The phase-separated phase is seen for all values of $V$ that we have considered provided $U << V$. The density range of the PS phase shrinks with an increase in the on-site interaction $U$. The SF and SS phases coexist in the PS phase but are phase-separated. The SF region in the phase-separated region shrinks monotonically with density. As a consequence, the SS phase expands with $\rho$. For $\rho < 0.5$, the SL phase is observed crossing over to SF for lower $U$ and DW for higher on-site interaction. In the SL phase, the modulation in the density $\rho_j$ causes the $S(k)$ peak to shift by a modulation wave vector $k_m$ which depends linearly on $\rho$, i.e., $k_m \approx 2\pi\rho$. The phase diagram of the EBH model in the $\rho - U$ plane is obtained, and the critical values of the SF-PS, PS-SS, SF-SS, SL-DW, SF-MI, SL-DW, and DW-MI are estimated for $V = 2,\ 4,\ 6$ in the soft-core case.

The effect of three-body interaction is observed using the hard-core three-body interaction. The $W$ in the EBH model encourages the formation of the density wave phase and enhances the PS phase. The transition for weak $|W|$ is from superfluid to supersolid and for strong $|W|$ from a superfluid to density wave through the phase-separation phase. The phase separation is shifted to a lower chemical potential $\mu$ with increasing strength of $|W|$. The density range of phase separation grows at the expense of SF and SS phases with the increasing $|W|$, and for strong $|W|$, the system collapses into the density wave phase.

CHAPTER 5

# Summary

## 5.1 Summary

Recent breakthroughs in cooling and trapping the quantum gases in optical lattice systems have provided ideal testing grounds for studying the phases and phase transitions in quantum many-body systems. These systems are free from complexities such as disorders and impurities, and many-body interactions are highly controllable and more accessible to manipulate. These model Hamiltonians are not precisely solvable, and several analytical and numerical approximations are employed to study them. In this thesis, we have developed approximate techniques named cluster mean-field theory plus density matrix renormalization group theory (CMFT+DMRG) to study the Bose-Hubbard systems.

In chapter 2 of this thesis, we discuss the mean-field theory (MFT) and the density matrix renormalization group theory (DMRG) method. The MFT method gives a simple and elegant approach to understanding the phases and phase transitions in the BH models. It accurately predicts the phases in the BH model as the inter-particle interactions are short-ranged. However, it does not provide an accurate qualitative measurement of the phase boundaries. Increasing the cluster size improves the mean-field results at the increased computational cost. Also, in the case of long-range interactions, the mean-field method may not provide compelling results, and we need to reinvent new techniques to study these systems.

The DMRG method is another successful procedure for studying the ground state phases in the BH models at large. However, it cannot resolve the phase boundaries directly in the gapless phases.

This thesis combines these two successful methods to overcome their limitations. In the CMFT+DMRG method, mean-field decoupling eliminates the edge effect in the DMRG method by including the quantum fluctuations at the edges., while giving us direct access to the gapless phases and the ability to study ground state properties of large systems using moderate computational power. Using the CMFT+DMRG method, we divide the system into clusters of length $L$ and apply mean-field approximations, decoupling the cluster from the neighbouring clusters. The Hamiltonian of the cluster is then used in the DMRG scheme to consistently calculate the system's ground state properties in a grand canonical ensemble. The system size increases with each iteration, and the ground state is minimized for every iteration using superfluid order parameters and density self consistently.

Next, we demonstrate the CMFT+DMRG method using the BH model. The CMFT+DMRG method characterizes the phases using the SF order parameter $\psi_i$ and density $\rho_i$ calculated on the self-consistent ground state. These parameters converge with increasing system size and show higher $\psi_i$ and $\rho_i$ towards the edges. The convergence rate of $\rho$ is faster than $\psi$. As the quantum fluctuations introduced by MF decoupling dampen off towards the center, the $\psi_i$ and $\rho_i$ are uniform around the center. Due to this reason, the parameters at the center $\psi(L/2)$ and $\rho(L/2)$ are used for the minimization. We obtain the signature of the superfluid (SF), $\psi \neq 0$, and Mott insulator, $\psi = 0$ phase predicted in the BH model. In the deep SF and MI phase, $\psi_i$ and $\rho_i$ converge with fewer iterations than close to the phase transition and infinite iterations at the SF to MI transition critical point. This effect is due to the increase in the correlation length as we approach the quantum critical point, limiting us in its resolution. In the end, we compare the CMFT+DMRG results with the DMRG. The DMRG works in the canonical ensemble, the chemical potential $\mu$ fixed in the CMFT+DMRG calculation; how-

ever, in the DMRG, $\mu$ is obtained from the particle and hole excitation energies. The phases in DMRG are characterized using the gap in the energy spectrum, the $\rho$, and compressibility $\kappa$. The MI phase is incompressible $\kappa = 0$, and in the SF phase, $\kappa \neq 0$ and densities are incommensurate. The CMFT+DMRG and DMRG phase diagrams are in good agreement. In addition, we calculate the correlation functions and condensate fraction in the SF and MI phases, and these quantities agree with the known results.

After establishing the CMFT+DMRG method for the BH model, we apply it to the extended Bose-Hubbard (EBH) model. The systems with long-range and many-body interactions in the Hamiltonian predict many exotic phases. The EBH model is the simplest model, with finite nearest-neighbour interactions. However, it has a rich phase diagram with superfluid phase, Mott insulator, supersolid, Haldane insulator, density wave, and solitonic wave phase. The nearest-neighbour interaction in the EBH model allows different boson densities at the neighbouring sites. Due to this effect, the entire lattice is divided into $A - B$ sub-lattices. The cluster Hamiltonian for the EBH model is obtained by performing the mean-field decoupling on hopping and nearest neighbour interaction terms. The self-consistent calculations are performed during each CMFT+DMRG iteration to compute superfluid density and density of bosons corresponding to $A - B$ sub-lattices and identify different phases using these quantities. The model maps into the quantum spin 1/2 model in the hard-core limit. For density $\rho = 1/2$, the EBH model shows a BKT transition at $V = 2t$ from the superfluid (X-Y order) to the Density wave (Ising) order with discontinuity in the superfluid density, density wave order parameter, and condensate fraction, which is in good agreement with the known results. The solitonic (SL) phase is also observed, surrounding the DW $\rho = 1/2$ phase for fixed $V$, the phase characterized by modulations in $n_i$ average. In the soft-core case, the effect of $V$ becomes prominent. In the soft-core limit, we focus on the region where the nearest neighbour interaction is more significant than the on-site interaction and obtain the phase diagram. The phase

diagram in this region is dominated by gapless superfluid, solitonic superfluid, supersolid, and phase separate (PS) phases. We observe the coexistence of SF and SS phases in the gapless phases from the $n_i$ averages. The density range in the PS phase is obtained for different $V$, and we observe that the PS phase diminishes gradually with increasing $U$. We observe the gapless SL phase for the densities below $\rho = 1/2$ transitioning into SF for low $U$ and DW for higher $U$ values. The modulation wave vector $k_m$ is obtained using the correlations from the structure factor, identified from the shifted peak position from $\pi$, and it obeys the relation $k_m = 2\pi\rho$. As densities increase, the SS and SF phases dominate the phase diagram for the incommensurate densities. The DW phase is energetically preferred when $V$ dominates for commensurate densities, which shifts the Mott insulator for higher $U$ and integer densities. Finally, we apply CMFT+DMRG to attractive three-body hard-core on-site potential in the EBH model to understand the effect of many-body interactions on the phases in the EBH model. The attractive three-body interaction in the EBH model with repulsive $U$ and $V$ enhances the PS phase at the cost of the SS phase. Direct transition from the PS phase to the DW phase is favoured for higher values of $W$.

The CMFT+DMRG method accurately captures all the gapless phases in the model we studied, like superfluid, supersolid, solitonic, and phase-separated phases. It also captures the density wave and the Mott insulator phases. However, the CMFT+DMRG model has few limitations. It fails to calculate accurately the critical values of the SF to MI transition at integer density. The correlation length diverges as we approach the critical point in the phase diagram. Convergence of the order parameter fails due to diverging correlation length. The critical parameters are accurately obtained within the DMRG method employing finite-size scaling. Such an approach is not feasible in the CMFT+DMRG method. The CMFT+DMRG method also failed to capture the Haldane phase in the EBH model at density $\rho = 1$ [84], [85]. The Haldane insulator phase is characterized by string order parameters that can't be calculated within the CMFT+DMRG

method. The eigenstate of the density matrix is not diagonal in the number operator sector in the CMFT+DMRG method, limiting the calculation of the string order parameter.

## 5.2 Outlook

Interestingly, by shaking, rotating the optical lattices, or inducing an asymmetry in the tunneling between the sites, one can introduce more complex terms in the model, like the effective artificial magnetic field, extended interaction between the atoms, spin degrees of freedom, and multi-body interactions. Additional interactions in the BH model lead to many exotic gapless phases. For example, the extended Bose-Hubbard model predicts gapless phases, like supersolid, solitonic phases and phase-separated, demonstrated using the CMFT+DMRG method. The spin-1 Bose-Hubbard model predicts polar and ferro superfluids and pair superfluids in the Bose-Hubbard model [108] with three-body interaction [41]. In addition, chiral superfluids $\pi$-superfluid phases are indicated in models with artificial gauge fields [60], [61], [63], [109]–[111]. The CMFT+DMRG method can be extended to these different model Hamiltonians to study the ground state phases and phase transitions.

CHAPTER 6

# Publications and Conferences

## 6.1 List of Publications

- P. P. Gaude, A. Das and R. V. Pai, "Cluster mean field plus density matrix renormalization theory for the Bose Hubbard models",*J.* Phys. A: Math. Theor., vol. 55, p. 265004, 2022
- P. P. Gaude, A. Das and R. V. Pai, "Superfluid, Phase-separation, Supersolid and Density Wave Phases in Extended Bose-Hubbard Model",*A*IP conference Proceedings, 2023 (accepted)
- B. K. Alavani, P. P. Gaude and R. V. Pai, "Random phase approximation and cluster mean field theory studies of hardcore Bose-Hubbard model",*A*IP conference Proceedings, vol. 1942, p. 1, 2018

## 6.2 List of Conferences attended

- Presented poster on ”Cluster mean field plus density matrix renormalization theory for the Bose Hubbard model” in StatPhys Kolkata IX (online) jointly organized by Indian Institute of Science and Education and Research and S. N. Bose National Centre for Basic Sciences, Kolkata during MArch 21-25, 2022.
- Presented poster on Superfluid, Phase-separation, Supersolid and Density Wave Phases in Extended Bose-Hubbard Model in 66 th DAE Solid state physics symposium, organized by BARC and held at BIT Mesra, Ranchi, Jharkhand, India during December 18-22, 2022

# Bibliography


[1] S. Bose, "Planck's gesetz und lichtquantenhypothese," *Zeitschrift fur Physik*, vol. 26, pp. 178–181, 1924. DOI: 10.1007/BF01327326.

[2] A. Einstein, *Sitzungsbericht der Preussischein Akademie der Wissenschaften*, p. 3, 1925.

[3] F. London, *Superfluids*. John Wiley and Sons, 1950.

[4] W. D. Phillips, "Nobel lecture: Laser cooling and trapping of neutral atoms," *Rev. Mod. Phys.*, vol. 70, pp. 721–741, 3 Jul. 1998. DOI: 10.1103/RevModPhys.70.721.

[5] W. Ketterle and N. V. Druten, "Evaporative cooling of trapped atoms," Advances In Atomic, Molecular, and Optical Physics, vol. 37, B. Bederson and H. Walther, Eds., pp. 181–236, 1996, ISSN: 1049-250X. DOI: https://doi.org/10.1016/S1049-250X(08)60101-9.

[6] M. H. Anderson, J. R. Ensher, M. R. Mathews, C. E. Wieman, and E. A. Cornell, "Observation of bose-einstein condensation in a dilute atomic vapor," *Science*, vol. 269, p. 198, 1995. DOI: 10.1126/science.269.5221.198.

[7] K. B. Davis, M. .-. Mewes, M. R. Andrews, *et al.*, "Bose-einstein condensation in a gas of sodium atoms," *Phys. Rev. Lett.*, vol. 75, pp. 3969–3973, 22 Nov. 1995. DOI: 10.1103/PhysRevLett.75.3969.

[8] C. C. Bradley, C. A. Sackett, J. J. Tollette, and R. G. Hulet, "Evidence of bose-einstein condensation in an atomic gas with attractive interactions," *Phys. Rev. Lett.*, vol. 75, p. 1687, 1995. DOI: 10.1103/PhysRevLett.75.1687.

[9] S. Kraft, F. Vogt, O. Appel, F. Riehle, and U. Sterr, "Bose-einstein condensation of alkaline earth atoms: $^{40}$Ca," *Phys. Rev. Lett.*, vol. 103, p. 130 401, 13 Sep. 2009. DOI: 10.1103/PhysRevLett.103.130401.

[10] G. Modungo, G. Ferrari, G. Roati, R. J. Brecha, A. Simoni, and M. Inguscio, "Bose-einstein condensation of potassium atoms by sympathetic cooling," *Science*, vol. 294, no. 5545, pp. 1320–1322, 2001. DOI: 10.1126/science.1066687.

[11] M. Landini, S. Roy, G. Roati, *et al.*, "Direct evaporative cooling of $^{39}$k atoms to bose-einstein condensation," *Phys. Rev. A*, vol. 86, p. 033 421, 3 Sep. 2012. DOI: 10.1103/PhysRevA.86.033421.

[12] T. Fukuhara, S. Sugawa, and Y. Takahashi, "Bose-einstein condensation of an ytterbium isotope," *Phys. Rev. A*, vol. 76, p. 051 604, 5 Nov. 2007. DOI: 10.1103/PhysRevA.76.051604.

[13] D. M. Stamper-Kurn, M. R. Andrews, A. P. Chikkatur, *et al.*, "Optical confinement of a bose-einstein condensate," *Phys. Rev. Lett.*, vol. 80, pp. 2027–2030, 10 Mar. 1998. DOI: 10.1103/PhysRevLett.80.2027.

[14] G. Modugno, G. Ferrari, G. Roati, R. J. Brecha, A. Simoni, and M. Inguscio, "Bose-einstein condensation of potassium atoms by sympathetic cooling," *Science*, vol. 294, no. 5545, pp. 1320–1322, 2001. DOI: 10.1126/science.1066687.

[15] J. Weiner, V. S. Bagnato, S. Zilio, and P. S. Julienne, "Experiments and theory in cold and ultracold collisions," *Rev. Mod. Phys.*, vol. 71, pp. 1–85, 1 Jan. 1999. DOI: 10.1103/RevModPhys.71.1.

[16] E. Cornell, "Very cold indeed: The nanokelvin physics of Bose-Einstein condensation," *J. Res. Natl. Inst. Stand. Technol.*, vol. 101, no. 4, pp. 419–434, Jul. 1996. DOI: 10.6028/jres.101.045.

[17] D. Jaksch, C. Bruder, J. I. Cirac, C. Gardiner, and P. Zoller, "Cold bosonic atoms in optical lattices," *Phys. Rev. Lett.*, vol. 81, pp. 3108–3111, 1998. DOI: 10.1103/PhysRevLett.81.3108.

[18] P. Courteille, R. S. Freeland, D. J. Heinzen, F. A. van Abeelen, and B. J. Verhaar, "Observation of a feshbach resonance in cold atom scattering," *Phys. Rev. Lett.*, vol. 81, pp. 69–72, 1 Jul. 1998. DOI: 10.1103/PhysRevLett.81.69.

[19] D. M. Stamper-Kurn, M. R. Andrews, A. P. Chikkatur, *et al.*, "Optical confinement of a bose-einstein condensate," *Phys. Rev. Lett.*, vol. 80, pp. 2027–2030, 10 Mar. 1998. DOI: 10.1103/PhysRevLett.80.2027.

[20] C. Chin, R. Grimm, P. Julienne, and E. Tiesinga, "Feshbach resonances in ultracold gases," *Rev. Mod. Phys.*, vol. 82, pp. 1225–1286, 2 Apr. 2010. DOI: 10.1103/RevModPhys.82.1225.

[21] I. Bloch, J. Dalibard, and W. Zwerger, "Many-body physics with ultracold gases," *Rev. Mod. Phys.*, vol. 80, pp. 885–964, 3 Jul. 2008. DOI: 10.1103/RevModPhys.80.885.

[22] K. Sheshadri, H. R. Krishnamurthy, R. Pandit, and T. V. Ramakrishnan, "Superfluid and insulating phases in an interacting-boson model: Mean-field theory and the rpa," *EPL (Europhysics Letters)*, vol. 22, p. 257, 1993. DOI: 10.1209/0295-5075/22/4/004.

[23] M. P. A. Fisher, P. B. Weichman, G. Grinstein, and D. S. Fisher, "Boson localization and the superfluid-insulator transition," *Phys. Rev. B*, vol. 40, p. 546, 198. DOI: 10.1103/PhysRevB.40.546.

[24] M. Greiner, O. Mandel, T. Esslinger, T. W. Hänsh, and I. Bloch, "Quantum phase transition from a superfluid to a mott insulator in a gas of ultracold atoms," *Nature*, vol. 415, pp. 39–44, 2002. DOI: 10.1038/415039a.

[25] T. Stöferle, H. Moritz, C. Schori, M. Köhl, and T. Esslinger, "Transition from a strongly interacting 1d superfluid to a mott insulator," *Phys. Rev. Lett.*, vol. 92, p. 130 403, 13 Mar. 2004. DOI: 10.1103/PhysRevLett.92.130403.

[26] I. B. Spielman, W. D. Phillips, and J. V. Porto, "Mott-insulator transition in a two-dimensional atomic bose gas," *Phys. Rev. Lett.*, vol. 98, p. 080 404, 8 Feb. 2007. DOI: 10.1103/PhysRevLett.98.080404.

[27] M. Köhl, H. Moritz, T. Stöferle, C. Schori, and T. Esslinger, "Superfluid to mott insulator transition in one, two, and three dimensions," *Journal of Low Temperature Physics*, vol. 138, no. 3, pp. 635–644, Feb. 2005. DOI: 10.1007/s10909-005-2273-4.

[28] D. S. Rokhsar and B. G. Kotliar, "Gutzwiller projection for bosons," *Phys. Rev. B*, vol. 44, pp. 10 328–10 332, 1991. DOI: 10.1103/PhysRevB.44.10328.

[29] J. M. Kurdestany, R. V. Pai, and R. Pandit, "Random-phase-approximation excitation spectra for bose-hubbard models," 2014. DOI: arXiv:1410.3621.

[30] K. Sengupta and N. Dupuis, "Mott-insulator-to-superfluid transition in the bose-hubbard model: A strong-coupling approach," *Phys. Rev. A*, vol. 71, p. 033 629, 2005. DOI: 10.1103/PhysRevA.71.033629.

[31] S. Konabe, T. Nikuni, and M. Nakamura, "Laser probing of the single-particle energy gap of a bose gas in an optical lattice in the mott-insulator phase," *Phys. Rev. A*, vol. 73, p. 033 621, 2006. DOI: 10.1103/PhysRevA.73.033621.

[32] C. Menotti and N. Trivedi, "Spectral weight redistribution in strongly correlated bosons in optical lattices," *Phys. Rev. B*, vol. 77, p. 235 120, 2008. DOI: 10.1103/PhysRevB.77.235120.

[33] B. Capogrosso-Sansone, N. V. Prokof'ev, and B. V. Svistunov, "Phase diagram and thermodynamics of the three-dimensional bose-hubbard model," *Phys. Rev. B*, vol. 75, p. 134 302, 2007. DOI: 10.1103/PhysRevB.75.134302.

[34] B. Capogrosso-Sansone, N. Soyler Sebnem Gunes Prokof'ev, and B. Svistunov, "Monte carlo study of the two-dimensional bose-hubbard model," *Phys. Rev. A*, vol. 77, p. 015 602, 2008. DOI: 10.1103/PhysRevA.77.015602.

[35] S. Ejima, H. Fehske, and F. Gebhard, "Dynamic properties of the one-dimensional bose-hubbard model," *Europhysics Letters*, vol. 93, p. 30 002, 2011. DOI: 10.1209/0295-5075/93/30002.

[36] J. Carrasquilla, S. R. Manmana, and M. Rigol, "Scaling of the gap, fidelity susceptibility, and bloch oscillations across the superfluid-to-mott-insulator transition in the one-dimensional bose-hubbard model," *Phys. Rev. A*, vol. 87, p. 043 606, 2013. DOI: 10.1103/PhysRevA.87.043606.

[37] T. Stöferle, H. Moritz, C. Schori, M. Köhl, and T. Esslinger, "Transition from a strongly interacting 1d superfluid to a mott insulator," *Phys. Rev. Lett.*, vol. 92, p. 130 403, 2004. DOI: 10.1103/PhysRevLett.92.130403.

[38] T. McIntosh, P. Pisarski, R. J. Gooding, and E. Zaremba, "Multisite mean-field theory for cold bosonic atoms in optical lattices," *Phys. Rev. A*, vol. 86, p. 013 623, 1 Jul. 2012. DOI: 10.1103/PhysRevA.86.013623.

[39] R. V. Pai, K. Sheshadri, and R. Pandit, "Phases and transitions in the spin-1 bose-hubbard model: Systematics of a mean-field theory," *Phys. Rev. B*, vol. 77, p. 014 503, 1 Jan. 2008. DOI: 10.1103/PhysRevB.77.014503.

[40] T. Lahaye, C. Menotti, L. Santos, M. Lewenstein, and T. Pfau, "The physics of dipolar bosonic quantum gases," *Reports on Progress in Physics*, vol. 72, p. 126 401, 2009. DOI: 10.1088/0034-4885/72/12/126401.

[41] S. Will, T. Best, U. Schneider, L. Hackermuller, D. Luhmann, and I. Bloch, "Time-resolved observation of coherent multi-body interactions in quantum phase revivals," *Nature*, vol. 465, p. 197, 2010. DOI: 10.1038/nature09036.

[42] J. K. Freericks and H. Monien, "Strong-coupling expansions for the pure and disordered bose-hubbard model," *Phys. Rev. B*, vol. 53, pp. 2691–2700, 1996. DOI: 10.1103/PhysRevB.53.2691.

[43] N. Teichmann, D. Hinrichs, M. Holthaus, and A. Eckardt, "Bose-hubbard phase diagram with arbitrary integer filling," *Phys. Rev. B*, vol. 79, p. 100 503, 2009. DOI: 10.1103/PhysRevB.79.100503.

[44] R. V. Pai, R. Pandit, H. R. Krishnamurthy, and S. Ramasesha, "One-dimensional disordered bosonic hubbard model: A density-matrix renormalization group study," *Phys. Rev. Lett.*, vol. 76, pp. 2937–2940, 1996. DOI: 10.1103/PhysRevLett.76.2937.

[45] T. D. Kuhner and H. Monien, "Phases of the one-dimensional bose-hubbard model," *Phys. Rev. B*, vol. 58, R14741–R14744, 1998. DOI: 10.1103/PhysRevB.58.R14741.

[46] G. Vidal, "Efficient simulation of one-dimensional quantum many-body systems," *Phys. Rev. Lett.*, vol. 93, p. 040 502, 2004. DOI: 10.1103/PhysRevLett.93.040502.

[47] I. Danshita and C. A. R. Sá de Melo, "Stability of superfluid and supersolid phases of dipolar bosons in optical lattices," *Phys. Rev. Lett.*, vol. 103, p. 225 301, 22 Nov. 2009. DOI: 10.1103/PhysRevLett.103.225301.

[48] T. McIntosh, P. Pisarski, R. J. Gooding, and E. Zaremba, "Multisite mean-field theory for cold bosonic atoms in optical lattices," *Phys. Rev. A*, vol. 86, p. 013 623, 2012. DOI: 10.1103/PhysRevA.86.013623.

[49] B. K. Alavani, A. Das, and R. V. Pai, "Cluster mean field theory for 2-dimensional spin-1 bose hubbard model," *J. Phys. B: At. Mol. Opt. Phys.*, vol. 51, p. 145 302, 2018. DOI: 10.1088/1361-6455/aac5b2.

[50] S. R. White, "Density matrix formulation for quantum renormalization groups," *Phys. Rev. Lett.*, vol. 69, pp. 2863–2866, 19 Nov. 1992. DOI: 10.1103/PhysRevLett.69.2863.

[51] S. R. White, "Density-matrix algorithms for quantum renormalization groups," *Phys. Rev. B*, vol. 48, pp. 10 345–10 356, 14 Oct. 1993. DOI: 10.1103/PhysRevB.48.10345.

[52] K. G. Wilson, "The renormalization group: Critical phenomena and the kondo problem," *Rev. Mod. Phys.*, vol. 47, pp. 773–840, 4 Oct. 1975. DOI: 10.1103/RevModPhys.47.773.

[53] U. Schollwöck, "The density-matrix renormalization group," *Rev. Mod. Phys.*, vol. 77, pp. 259–315, 1 Apr. 2005. DOI: 10.1103/RevModPhys.77.259.

[54] T. D. Kuhner, S. R. White, and H. Monien, "One-dimensional bose-hubbard model with nearest-neighbor interaction," *Phys. Rev. B*, vol. 61, pp. 12 474–12 489, 2000. DOI: 10.1103/PhysRevB.61.12474.

[55] D. Yamamoto, T. Fukuhara, and I. Danshita, "Frustrated quantum magnetism with bose gases in triangular optical lattices at negative absolute temperatures," *Communications Physics*, vol. 3, p. 56, 2020. DOI: 10.1038/s42005-020-0323-5.

[56] D. Yamamoto, C. Suzuki, G. Marmorini, S. Okazaki, and N. Furukawa, "Quantum and thermal phase transitions of the triangular su(3) heisenberg model under magnetic fields," *Phys. Rev. Lett.*, vol. 125, p. 057 204, 2020. DOI: 10.1103/PhysRevLett.125.057204.

[57] D. Yamamoto, G. Marmorini, M. Tabata, K. Sakakura, and I. Danshita, "Magnetism driven by the interplay of fluctuations and frustration in the easy-axis triangular xxz model with transverse fields," *Phys. Rev. B*, vol. 100, p. 140 410, 2019. DOI: 10.1103/PhysRevB.100.140410.

[58] J. M. Kosterlitz and D. J. Thouless, "Ordering, metastability and phase transitions in two-dimensional systems," *Journal of Physics C: Solid State Physics*, vol. 6, p. 1181, 1973. DOI: 10.1088/0022-3719/6/7/010.

[59] S. Ramanan, T. Mishra, M. S. Luthra, R. V. Pai, and B. P. Das, "Signatures of the superfluid-to-mott-insulator transition in cold bosonic atoms in a one-dimensional optical lattice," *Phys. Rev. A*, vol. 79, p. 013 625, 2009. DOI: 10.1103/PhysRevA.79.013625.

[60] A. Dhar, T. Mishra, M. Maji, R. V. Pai, S. Mukerjee, and A. Paramekanti, "Chiral mott insulator with staggered loop currents in the fully frustrated bose-hubbard model," *Phys. Rev. B*, vol. 87, p. 174 501, 2013. DOI: 10.1103/PhysRevB.87.174501.

[61] A. Dhar, M. Maji, T. Mishra, R. V. Pai, S. Mukerjee, and A. Paramekanti, "Bose-hubbard model in a strong effective magnetic field: Emergence of a chiral mott insulator ground state," *Phys. Rev. A*, vol. 85, p. 041 602, 2012. DOI: 10.1103/PhysRevA.85.041602.

[62] J. Struck, C. Ölschläger, R. L. Targat, *et al.*, "Quantum simulation of frustrated classical magnetism in triangular optical lattices," *Science*, vol. 333, no. 6045, pp. 996–999, 2011. DOI: 10.1126/science.1207239.

[63] J. Struck, C. Ölschläger, M. Weinberg, *et al.*, "Tunable gauge potential for neutral and spinless particles in driven optical lattices," *Phys. Rev. Lett.*, vol. 108, p. 225 304, 22 May 2012. DOI: 10.1103/PhysRevLett.108.225304.

[64] G. Wirth, M. Alschlager, and A. Hemmerich, "Evidence for orbital superfluidity in the p-band of a bipartite optical square lattice," *Nature Physics*, vol. 7, p. 147, 2011. DOI: 10.1038/nphys1857.

[65] O. Penrose and L. Onsager, "Bose-einstein condensation and liquid helium," *Phys. Rev.*, vol. 104, pp. 576–584, 3 Nov. 1956. DOI: 10.1103/PhysRev.104.576.

[66] E. Kim and M. H. W. Chan, "Probable observation of a supersolid helium phase," *Nature*, vol. 427, no. 6971, pp. 225–227, Jan. 2004. DOI: 10.1038/nature02220.

[67] A. J. Leggett, "Can a solid be "superfluid"?" *Phys. Rev. Lett.*, vol. 25, pp. 1543–1546, 22 Nov. 1970. DOI: 10.1103/PhysRevLett.25.1543.

[68] A. F. Andreev, "Supersolidity of glasses," *JETP Letters*, vol. 85, no. 11, pp. 585–587, Aug. 2007, ISSN: 1090-6487. DOI: 10.1134/S0021364007110124.

[69] T. Leggett, "Physics. superfluidity in a crystal?" *Science*, vol. 305, no. 5692, pp. 1921–1922, 2004. DOI: 10.1126/science.1103584.

[70] E. Kim and M. H. W. Chan, "Observation of superflow in solid helium," *Science*, vol. 305, no. 5692, pp. 1941–1944, Sep. 2004. DOI: 10.1126/science.1101501.

[71] S. Sasaki, R. Ishiguro, F. Caupin, H. J. Maris, and S. Balibar, "Superfluidity of grain boundaries and supersolid behavior," *Science*, vol. 313, no. 5790, pp. 1098–1100, Jul. 2006. DOI: 10.1126/science.1130879.

[72] A. Griesmaier, J. Werner, S. Hensler, J. Stuhler, and T. Pfau, "Bose-einstein condensation of chromium," *Phys. Rev. Lett.*, vol. 94, p. 160 401, 16 Apr. 2005. DOI: 10.1103/PhysRevLett.94.160401.

[73] J. Stuhler, A. Griesmaier, T. Koch, *et al.*, "Observation of dipole-dipole interaction in a degenerate quantum gas," *Phys. Rev. Lett.*, vol. 95, p. 150 406, 15 Oct. 2005. DOI: 10.1103/PhysRevLett.95.150406.

[74] A. de Paz, A. Sharma, A. Chotia, *et al.*, "Nonequilibrium quantum magnetism in a dipolar lattice gas," *Phys. Rev. Lett.*, vol. 111, p. 185 305, 18 Oct. 2013. DOI: 10.1103/PhysRevLett.111.185305.

[75] B. Naylor, A. Reigue, E. Maréchal, O. Gorceix, B. Laburthe-Tolra, and L. Vernac, "Chromium dipolar fermi sea," *Phys. Rev. A*, vol. 91, p. 011 603, 1 Jan. 2015. DOI: 10.1103/PhysRevA.91.011603.

[76] M. Lu, N. Q. Burdick, S. H. Youn, and B. L. Lev, "Strongly dipolar bose-einstein condensate of dysprosium," *Phys. Rev. Lett.*, vol. 107, p. 190 401, 19 Oct. 2011. DOI: 10.1103/PhysRevLett.107.190401.

[77] K. Aikawa, A. Frisch, M. Mark, *et al.*, "Bose-einstein condensation of erbium," *Phys. Rev. Lett.*, vol. 108, p. 210 401, 21 May 2012. DOI: 10.1103/PhysRevLett.108.210401.

[78] S. Baier, M. J. Mark, D. Petter, *et al.*, "Extended bose-hubbard models with ultracold magnetic atoms," *Science*, vol. 352, no. 6282, pp. 201–205, 2016. DOI: 10.1126/science.aac9812.

[79] K. Góral, L. Santos, and M. Lewenstein, "Quantum phases of dipolar bosons in optical lattices," *Phys. Rev. Lett.*, vol. 88, p. 170 406, 17 Apr. 2002. DOI: 10.1103/PhysRevLett.88.170406.

[80] T. Dauxois, S. Ruffo, E. Arimondo, and M. Wilkens, "Dynamics and thermodynamics of systems with long-range interactions: An introduction," in *Dynamics and Thermodynamics of Systems with Long-Range Interactions*, T. Dauxois, S. Ruffo, E. Arimondo, and M. Wilkens, Eds. Berlin, Heidelberg: Springer Berlin Heidelberg, 2002, pp. 1–19, ISBN: 978-3-540-45835-7. DOI: 10.1007/3-540-45835-2_1.

[81] S. Sinha and L. Santos, "Cold dipolar gases in quasi-one-dimensional geometries," *Phys. Rev. Lett.*, vol. 99, p. 140 406, 14 Oct. 2007. DOI: 10.1103/PhysRevLett.99.140406.

[82] B. Pasquiou, G. Bismut, E. Maréchal, *et al.*, "Spin relaxation and band excitation of a dipolar bose-einstein condensate in 2d optical lattices," *Phys. Rev. Lett.*, vol. 106, p. 015 301, 1 Jan. 2011. DOI: 10.1103/PhysRevLett.106.015301.

[83] R. V. Pai and R. Pandit, "Superfluid, mott-insulator, and mass-density-wave phases in the one-dimensional extended bose-hubbard model," *Phys. Rev. B*, vol. 71, p. 104 508, 10 Mar. 2005. DOI: 10.1103/PhysRevB.71.104508.

[84] E. G. Dalla Torre, E. Berg, and E. Altman, "Hidden order in 1d bose insulators," *Phys. Rev. Lett.*, vol. 97, p. 260 401, 26 Dec. 2006. DOI: 10.1103/PhysRevLett.97.260401.

[85] D. Rossini and R. Fazio, "Phase diagram of the extended bose–hubbard model," *New Journal of Physics*, vol. 14, no. 6, p. 065 012, Jun. 2012. DOI: 10.1088/1367-2630/14/6/065012.

[86] G. G. Batrouni, R. T. Scalettar, G. T. Zimanyi, and A. P. Kampf, "Supersolids in the bose-hubbard hamiltonian," *Phys. Rev. Lett.*, vol. 74, pp. 2527–2530, 13 Mar. 1995. DOI: 10.1103/PhysRevLett.74.2527.

[87] G. G. Batrouni, F. Hébert, and R. T. Scalettar, "Supersolid phases in the one-dimensional extended soft-core bosonic hubbard model," *Phys. Rev. Lett.*, vol. 97, p. 087 209, 8 Aug. 2006. DOI: 10.1103/PhysRevLett.97.087209.

[88] G. G. Batrouni, F. Hébert, and R. T. Scalettar, "Supersolid phases in the one-dimensional extended soft-core bosonic hubbard model," *Phys. Rev. Lett.*, vol. 97, p. 087 209, 8 Aug. 2006. DOI: 10.1103/PhysRevLett.97.087209.

[89] T. Mishra, R. V. Pai, S. Ramanan, M. S. Luthra, and B. P. Das, "Supersolid and solitonic phases in the one-dimensional extended bose-hubbard model," *Phys. Rev. A*, vol. 80, p. 043 614, 4 Oct. 2009. DOI: 10.1103/PhysRevA.80.043614.

[90] G. G. Batrouni, V. G. Rousseau, R. T. Scalettar, and B. Grémaud, "Competing phases, phase separation, and coexistence in the extended one-dimensional bosonic hubbard model," *Phys. Rev. B*, vol. 90, p. 205 123, 20 Nov. 2014. DOI: 10.1103/PhysRevB.90.205123.

[91] G. G. Batrouni and R. T. Scalettar, "Phase separation in supersolids," *Phys. Rev. Lett.*, vol. 84, pp. 1599–1602, 2000. DOI: 10.1103/PhysRevLett.84.1599.

[92] K. Kottmann, A. Haller, A. Acín, G. E. Astrakharchik, and M. Lewenstein, "Supersolid-superfluid phase separation in the extended bose-hubbard model," *Phys. Rev. B*, vol. 104, p. 174 514, 17 Nov. 2021. DOI: 10.1103/PhysRevB.104.174514.

[93] F. J. Burnell, M. M. Parish, N. R. Cooper, and S. L. Sondhi, "Devil's staircases and supersolids in a one-dimensional dipolar bose gas," *Phys. Rev. B*, vol. 80, p. 174 519, 17 Nov. 2009. DOI: 10.1103/PhysRevB.80.174519.

[94] P. P. Gaude, A. Das, and R. V. Pai, "Superfluid, phase-separation, supersolid and density wave phases in extended bose-hubbard model," *AIP Conference Proceedings (Accepted)*, 2023.

[95] G. G. Batrouni, R. T. Scalettar, V. G. Rousseau, and B. Grémaud, "Competing supersolid and haldane insulator phases in the extended one-dimensional bosonic hubbard model," *Phys. Rev. Lett.*, vol. 110, p. 265 303, 26 Jun. 2013. DOI: 10.1103/PhysRevLett.110.265303.

[96] D. Rossini, V. Lante, A. Parola, and F. Becca, "Phase diagram of hard-core bosons on a zigzag ladder," *Phys. Rev. B*, vol. 83, p. 155 106, 15 Apr. 2011. DOI: 10.1103/PhysRevB.83.155106.

[97] O. Dutta, M. Gajda, P. Hauke, *et al.*, "Non-standard hubbard models in optical lattices: A review," *Reports on Progress in Physics*, vol. 78, no. 6, p. 066 001, May 2015. DOI: 10.1088/0034-4885/78/6/066001.

[98] T. Kraemer, M. Mark, P. Waldburger, *et al.*, "Evidence for efimov quantum states in an ultracold gas of caesium atoms," en, *Nature*, vol. 440, no. 7082, pp. 315–318, Mar. 2006. DOI: 10.1038/nature04626.

[99] M. J. Mark, E. Haller, K. Lauber, *et al.*, "Preparation and spectroscopy of a metastable mott-insulator state with attractive interactions," *Phys. Rev. Lett.*, vol. 108, p. 215 302, 21 May 2012. DOI: 10.1103/PhysRevLett.108.215302.

[100] G. K. Campbell, J. Mun, M. Boyd, *et al.*, "Imaging the mott insulator shells by using atomic clock shifts," *Science*, vol. 313, no. 5787, pp. 649–652, 2006. DOI: 10.1126/science.1130365.

[101] W. S. Bakr, P. M. Preiss, M. E. Tai, R. Ma, J. Simon, and M. Greiner, "Orbital excitation blockade and algorithmic cooling in quantum gases," en, *Nature*, vol. 480, no. 7378, pp. 500–503, Dec. 2011. DOI: 10.1038/nature10668.

[102] M. J. Mark, E. Haller, K. Lauber, J. Danz, A. J. Daley, and H.-C. Näger, "Precision measurements on a tunable mott insulator of ultracold atoms," *Phys.Rev.Lett.*, vol. 107, p. 175 301, 2011. DOI: 10.1103/PhysRevLett.107.175301.

[103] M. Singh, S. Greschner, and T. Mishra, "Anomalous pairing of bosons: Effect of multibody interactions in an optical lattice," *Phys. Rev. A.*, vol. 98, p. 023 615, 2018. DOI: 10.1103/PhysRevA.98.023615.

[104] T. Sowi ński, "Exact diagonalization of the one-dimensional bose-hubbard model with local three-body interactions," *Phys. Rev. A*, vol. 85, p. 065 601, 6 Jun. 2012. DOI: 10.1103/PhysRevA.85.065601.

[105] A. M. Daley, J. M. Taylor, S. Diehl, M. Baranov, and P. Zoller, "Atomic three-body loss as a dynamical three-body interaction," *Phys. Rev. Lett.*, vol. 102, p. 040 402, 2009. DOI: 10.1103/PhysRevLett.102.040402.

[106] A. Safavi-Naini, J. von Stecher, B. Capogrosso-Sansone, and S. T. Rittenhouse, "First-order phase transitions in optical lattices with tunable three-body onsite interaction," *Phys. Rev. Lett.*, vol. 109, p. 135 302, 13 Sep. 2012. DOI: 10.1103/PhysRevLett.109.135302.

[107] M. Singh, A. Dhar, T. Mishra, R. V. Pai, and B. P. Das, "Three-body on-site interactions in ultracold bosonic atoms in optical lattices and superlattices," *Phys. Rev. A*, vol. 85, p. 051 604, 5 May 2012. DOI: 10.1103/PhysRevA.85.051604.

[108] D. M. Stamper-Kurn, M. R. Andrews, A. P. Chikkatur, *et al.*, "Optical confinement of a bose-einstein condensate," *Phys. Rev. Lett.*, vol. 80, pp. 2027–2030, 1998. DOI: 10.1103/PhysRevLett.80.2027.

[109] A. Tokuno and A. Georges, "Ground states of a bose–hubbard ladder in an artificial magnetic field: Field-theoretical approach," *New Journal of Physics*, vol. 16, p. 073 005, 7 Jul. 2014. DOI: 10.1088/1367-2630/16/7/073005.

[110] B. Song, S. Dutta, S. Bhave, J.-C. Yu, N. Carter E.and Cooper, and U. Schneider, "Realizing discontinuous quantum phase transitions in a strongly correlated driven optical lattice," *Nature Phys.*, vol. 18, pp. 259–264, 2022. DOI: 10.1038/s41567-021-01476-w.

[111] S. S. Shettigar, B. K. Alavani, and R. V. Pai, "Mott insulator to superfluid with staggered phases in driven optical lattices," *AIP Conference Proceedings (Accepted)*, 2023.